

**ISTANBUL TECHNICAL UNIVERSITY ★ GRADUATE SCHOOL OF SCIENCE**  
**ENGINEERING AND TECHNOLOGY**

**CRUSTAL STRUCTURE OF THE NORTH-WESTERN TURKEY AROUND  
THE NORTH ANATOLIAN FAULT ZONE (NAFZ) RESOLVED FROM  
THE HIGH-RESOLUTION AMBIENT SEISMIC NOISE TOMOGRAPHY**



**M.Sc. THESIS**

**Buse TURUNÇTUR**

**Department of Geophysical Engineering**

**Geophysical Engineering Programme**

**DECEMBER 2018**



**ISTANBUL TECHNICAL UNIVERSITY ★ GRADUATE SCHOOL OF SCIENCE**  
**ENGINEERING AND TECHNOLOGY**

**CRUSTAL STRUCTURE OF THE NORTH-WESTERN TURKEY AROUND  
THE NORTH ANATOLIAN FAULT ZONE (NAFZ) RESOLVED FROM  
THE HIGH-RESOLUTION AMBIENT SEISMIC NOISE TOMOGRAPHY**

**M.Sc. THESIS**

**Buse TURUNÇTUR  
(505161418)**

**Department of Geophysical Engineering**

**Geophysical Engineering Programme**

**Thesis Advisor: Dr. Tuna EKEN**

**DECEMBER 2018**



**ISTANBUL TEKNİK ÜNİVERSİTESİ ★ FEN BİLİMLERİ ENSTİTÜSÜ**

**ARKA ALAN SİSMİK GÜRÜLTÜ TOMOGRAFİ YÖNTEMİ  
KULLANILARAK KUZAY ANADOLU FAY ZONU (KAFZ) VE KUZAYBATI  
TÜRKİYE'NİN KABUK YAPISININ YÜKSEK ÇÖZÜNÜRLÜKTE  
GÖRÜNTÜLENMESİ**

**YÜKSEK LİSANS TEZİ**

**Buse TURUNÇTUR  
(505161418)**

**Jeofizik Mühendisliği Anabilim Dalı**

**Jeofizik Mühendisliği Programı**

**Tez Danışmanı: Dr. Tuna EKEN**

**ARALIK 2018**



Buse Turunçtur, a M.Sc. student of ITU Graduate School of Science Engineering and Technology student ID 505161418, successfully defended the thesis/dissertation entitled “CRUSTAL STRUCTURE OF THE NORTH-WESTERN TURKEY AROUND THE NORTH ANATOLIAN FAULT ZONE (NAFZ) RESOLVED FROM THE HIGH-RESOLUTION AMBIENT SEISMIC NOISE TOMOGRAPHY”, which she prepared after fulfilling the requirements specified in the associated legislations, before the jury whose signatures are below.

**Thesis Advisor :**     **Dr. Tuna EKEN** .....  
Istanbul Technical University

**Jury Members :**     **Prof. Dr. Tuncay TAYMAZ** .....  
Istanbul Technical University

**Prof. Dr. Ali PINAR** .....  
Boğaziçi University

**Dr. Tuna EKEN** .....  
Istanbul Technical University

**Date of Submission : 16 November 2018**  
**Date of Defense : 14 December 2018**





*To my Mom and Rex,*



## FOREWORD

I would like to thank my supervisor Dr Tuna Eken for his continuous encouragements, patience and support. His experiences and advices have been very helpful to build my career in academics. I am thankful for him to accept me as bachelor and master student and as well as for his belief in my research and passion.

I also would like to thank Dr Erdinc Saygin from University of Western Australia for his enourmous guidance and sharing experience on Transdimensional Bayesian Inversion approach. He was always willing to answer my questions regarding data processing and modelling related problems. I am also very grateful to him for inviting me to Australia to work on the thesis.

I am indebted to Prof. Tuncay Taymaz for his guidance and advises during my bachelor and master projects. I would like to thank him for providing me with an office to work comfortably at the university. I thank Assoc. Prof. Dr. Seda Yolsal-Çevikbilen for her friendly attitude always.

The facilities of IRIS Data Services and specifically the IRIS Data Management Center were used for access to waveforms, related metadata, and/or derived products used in this study. IRIS Data Services are funded through the Seismological Facilities for the Advancement of Geoscience and EarthScope (SAGE) Proposal of the National Science Foundation under Cooperative Agreement EAR-1261681. The other seismic datasets used in this study were obtained from the repositories of Kandilli Observatory and Earthquake Research Institute (KOERI) with network code KO, Earth Research Directorate of Turkey (AFAD) with newtork code TU and RESIF (<http://dx.doi.org/10.15778/RESIF.XW2007>,<http://dx.doi.org/10.15778/RESIF.YI2008>).

We use fast marching method developed by Rawlinson and Sambridge (2004a,b) to conduct forward calculation of traveltimes. This research was undertaken with the assistance of the resources provided at the High Performance Computing (HCP) facilities *of the Commonwealth Scientific and Industrial Research Organisation (CSIRO)*. This study makes use of the computer package *rj-tomo* which was made available with support from the Inversion Laboratory (*ilab*). *Ilab* is a program for construction and distribution of data inference software in the geosciences supported by AuScope Ltd, a non-profit organization for Earth Science infrastructure funded by the Australian Federal Government. We use the Scientific Color-Map of F. Cartelli (<http://www.fabiocrameri.ch/colourmaps.php>).

I would like to thank Hoël for his unconditional help and encouragement during my unmotivated times and for talking for hours to explain me things that I do not understand. I am thankful to my friends Büş for always helping and being there for me, to Ömer for helping me for the thesis during the time that I blocked, to Judith for helping me with her GMT skills and for the scientific conversations, to Gizem for studying with me during the master, to Oğuzhan for providing convenience for me to finalize my thesis.

Finally, I would like to thank my mom for her unconditional love and support each day. I can never pay back her the support and love that she gives me. I am grateful to meet with Aynur Kuđu Ünal whom always there for me and helps me to improve myself. And I thank my dear lovely sister Hazal for showing me love and support no matter what.

November 2018

Buse TURUNÇTUR



## TABLE OF CONTENTS

	<u>Page</u>
<b>FOREWORD</b> .....	<b>ix</b>
<b>TABLE OF CONTENTS</b> .....	<b>xi</b>
<b>ABBREVIATIONS</b> .....	<b>xiii</b>
<b>SYMBOLS</b> .....	<b>xv</b>
<b>LIST OF FIGURES</b> .....	<b>xvii</b>
<b>SUMMARY</b> .....	<b>xix</b>
<b>ÖZET</b> .....	<b>xxi</b>
<b>1. INTRODUCTION</b> .....	<b>1</b>
1.1 Tectonic Settings of Turkey .....	4
1.1.1 Indications of the deformation from geodetic observations.....	5
1.1.2 Different tectonic zones of the study area.....	7
1.1.3 The North Anatolian Fault Zone (NAFZ).....	8
1.1.4 The Sea of Marmara.....	10
1.2 Main Purpose of the Study.....	11
<b>2. PREVIOUS STUDIES</b> .....	<b>15</b>
<b>3. AMBIENT SEISMIC NOISE TOMOGRAPHY</b> .....	<b>19</b>
3.1 Imaging with Noise.....	19
3.2 Retrieval of Green's Function.....	22
3.3 Nonlinear Traveltime Tomography.....	23
3.3.1 Principle.....	23
3.3.2 Tomographic Inversion.....	24
3.4 Transdimensional Bayesian Tomography .....	25
3.4.1 Bayesian Inference .....	25
3.4.2 Tomographic inversion.....	27
<b>4. DATA</b> .....	<b>31</b>
4.1 Data Sources .....	31
4.2 Data Processing .....	31
<b>5. APPLICATION OF THE INVERSION TO DATA</b> .....	<b>37</b>
5.1 Tomographic Inversion .....	37
5.2 Transdimensional Bayesian Tomography .....	38
<b>6. RESULTS AND INTERPRETATIONS</b> .....	<b>41</b>
<b>7. CONCLUSION</b> .....	<b>75</b>
<b>REFERENCES</b> .....	<b>77</b>
<b>CURRICULUM VITAE</b> .....	<b>87</b>



## ABBREVIATIONS

<b>AAB</b>	: Armutlu-Almacik Block,
<b>AB</b>	: Adapazari Basin,
<b>AFAD</b>	: Afet ve Acil Durum Yönetimi Başkanlığı,
<b>ASTER</b>	: Advanced Spaceborne Thermal Emission and Reflection Radiometer,
<b>ATB</b>	: Anatolide-Tauride Block,
<b>CAV</b>	: Central Anatolian Volcanics,
<b>CB</b>	: Cinarcik Basin,
<b>CMF</b>	: Central Marmara Fault,
<b>CSIRO</b>	: Commonwealth Scientific and Industrial Research Organisation,
<b>DANA</b>	: Dense Array for North Anatolia,
<b>DSFS</b>	: Dead Sea Fault System,
<b>EAF</b>	: East Anatolian Fault,
<b>EAFS</b>	: East Anatolian Fault System,
<b>EAFZ</b>	: East Anatolian Fault Zone,
<b>FMM</b>	: Fast Marching Method,
<b>GEBCO</b>	: General Bathymetric Charts of the Oceans,
<b>GMT</b>	: General Mapping Tools,
<b>GPS</b>	: Global Positioning System,
<b>HPC</b>	: High Performance Computing,
<b>IASPE91</b>	: International Association of Seismology and Physics of the Earth's Interior,
<b>IRIS</b>	: Incorporated Research Institutions for Seismology,
<b>IZ</b>	: Istanbul Zone,
<b>KAFZ</b>	: Kuzey Anadolu Fay Zonu,
<b>KAIVF</b>	: Kırka-Afyon-Isparta Volcanic Field,
<b>KM</b>	: Kırşehir Massif,
<b>KOERI</b>	: Kandilli Observatory and Earthquake Research Institute,
<b>NAF</b>	: North Anatolian Fault,
<b>NAFS</b>	: North Anatolian Fault System,
<b>NAFZ</b>	: North Anatolian Fault Zone,

**NNAF** : Northern Strand of North Anatolian Fault,  
**OBS** : Ocean Bottom Seismometers,  
**PREM** : Preliminary Reference Earth Model,  
**RESIF** : French Seismologic and Geodetic Network,  
**rj-McMC** : Reversible-jump Markov chain Monte Carlo,  
**SAGE** : Seismological Facilities for the Advancement of Geoscience,  
**SNAF** : Southern Strand of North Anatolian Fault,  
**SZ** : Sakarya Zone,  
**TB** : Tekirdag Basin.



## SYMBOLS

$C_{AB}(\tau)$	: Cross-correlation function,
$\mathbf{m}_0$	: Reference model,
$\mathbf{m}_0$	: Reference Model,
$v_g$	: Group velocity,
$v_p$	: Phase velocity,
$\sigma_d^2$	: Estimated variance of data,
$\mathbf{d}$	: Data,
$\mathbf{d}_{\text{obs}}$	: Observed data,
$g(\mathbf{m})$	: Estimated data,
$H(t)$	: Heaviside function,
$k$	: Wave number,
$L(\mathbf{v})$	: Raypath,
$\mathbf{m}$	: Model parameter,
$p(\mathbf{d}_{\text{obs}} \mathbf{m})$	: Likelihood function,
$p(\mathbf{m})$	: Prior probability density of $\mathbf{m}$ ,
$p(\mathbf{m} \mathbf{d}_{\text{obs}})$	: Posterior probability distribution,
$t$	: Traveltimes,
$\mathbf{v}(\mathbf{x})$	: Velocity field,
$\omega$	: Angular frequency,
$\epsilon$	: Damping factor,
$\pi$	: Pi,
$\tau$	: Lag time,
$\phi(\mathbf{m})$	: Misfit function.



## LIST OF FIGURES

	<u>Page</u>
<b>Figure 1.1:</b> A schematic view of the difference between group velocity and phase velocity. The sum of two sinusoidal waves with a different frequencies and wavenumbers. The velocity of individual peaks represents the phase velocity and the velocity of the wave packets represents the group velocity.....	2
<b>Figure 1.2:</b> Seismicity of the Anatolian Plate and surroundings for a period of 1973–2007.....	5
<b>Figure 1.3:</b> Map of major plate boundaries for the Anatolian plate and surroundings...6	6
<b>Figure 1.4:</b> A schematic view of the tectonic settings in the Eastern Mediterranean....6	6
<b>Figure 1.5:</b> Major tectonic map of Turkey.....7	7
<b>Figure 1.6:</b> Historical earthquakes that occurred along the NAFZ.....9	9
<b>Figure 1.7:</b> Tectonic settings of the Marmara Region.....11	11
<b>Figure 1.8:</b> Active tectonics boundaries of Anatolian Plate.....12	12
<b>Figure 2.1:</b> The full-waveform tomographic inversion results shows the vertical slices of Vs.....	16
<b>Figure 2.2:</b> P and S velocity anomaly results for 5, 15, 30 and 50 km depths.....	16
<b>Figure 2.3:</b> The fault model for the geometry of NAFZ.....	17
<b>Figure 3.1:</b> The schematic view of frequency range of ambient seismic wavefield...20	20
<b>Figure 3.2:</b> A schematic view of the excitation of a) seismic hum and b) microseisms.20	20
<b>Figure 3.3:</b> The difference of the process by using active source and passive source..21	21
<b>Figure 3.4:</b> Retrieval of the Green’s function, a) the noise evenly distributed in space (red dots) around the receivers $x_A$ and $x_B$ , b) the cross-correlation of the noise for each source, c) the sum of the cross-correlations.....	23
<b>Figure 3.5:</b> Group velocity maps obtained by cross-correlating the one month noise a) Rayleigh waves for period 7.5 sec b) Rayleigh waves for period 15 sec..23	23
<b>Figure 3.6:</b> a) The best fit model which is the only global minimum b) probability density function which has numerous maximums.....	26
<b>Figure 3.7:</b> An example of a Voronoi cells which are in irregular shape shown in black lines and nodes shown in red dots.....	28
<b>Figure 3.8:</b> The steps of tomographic inversion used in this study. Two loops are shown; the black lines show the outer loop and the dashed red lines show the inner loop. ....	29
<b>Figure 4.1:</b> Locations of the seismic stations used in this study.....	32
<b>Figure 4.2:</b> Instrument response test applied to the cross-correlation between the stations EASY and EDRB.....	33
<b>Figure 4.3:</b> An example of cross-correlation between TVSB and ADVT stations. Approximately at -50 sec and 50 sec, the two-sided Green's function of the Rayleigh wave is observable.....	33
<b>Figure 4.4:</b> Four examples of cross correlations between stations TVSB and DB01, DB02, DB07, DB08.....	34

<b>Figure 4.5:</b> Extracted Green's functions between all the available stations and a)TVSB, b)KLYT stations. Green lines correspond to 2.4 km/s group velocity.....	<b>35</b>
<b>Figure 4.6:</b> An example of the filtering process shows the group velocities in respect to period...../.....	<b>35</b>
<b>Figure 4.7:</b> Number of picks for every period between 1 and 20 s. The maximum number of picks is over 6000 for period 3 s.....	<b>36</b>
<b>Figure 5.1:</b> Effects of the smoothing and damping parameters on the inversion results. The damping $\epsilon$ and smoothing $\eta$ parameters are; a) $\epsilon=10.5$ $\eta=10.5$ , b) $\epsilon=100.5$ $\eta=100.5$ , c) $\epsilon=500.5$ $\eta=500.5$ , d) $\epsilon=1000.5$ $\eta=1000.5$ .....	<b>37</b>
<b>Figure 5.2:</b> The map of raypath coverage of the study area for period 3 sec after applying the fully nonlinear inversion. Red triangles represent the seismic stations that are used in this study.....	<b>38</b>
<b>Figure 5.3:</b> Group velocity models for each iteration for period of 3 sec. a)First iteration, b)Second iteration, c)Third iteration, d)Fourth iteration, e)Fifth iteration.....	<b>39</b>
<b>Figure 6.1:</b> Group velocity images obtained from nonlinear tomography for periods between 1 sec and 20 sec. The group velocity ranges between 1.4 km/s and 3.2 km/s.....	<b>44-53</b>
<b>Figure 6.2:</b> Group velocity images obtained from Transdimensional Bayesian tomography for periods between 1 sec and 20 sec. The group velocity ranges between 1.4 km/s and 3.2 km/s.....	<b>54-63</b>
<b>Figure 6.3:</b> The uncertainty maps for periods 1-20 sec, The uncertainty tanges between 0.0-1.0 km/s. 0.0 km/s represents the lowest uncertainty and 1.0 km/s represents the highest uncertainty. Black lines represent the NAFZ, dashed red lines represent the suture zones.....	<b>64-73</b>

# **CRUSTAL STRUCTURE OF THE NORTH-WESTERN TURKEY AROUND THE NORTH ANATOLIAN FAULT ZONE (NAFZ) RESOLVED FROM THE HIGH-RESOLUTION AMBIENT SEISMIC NOISE TOMOGRAPHY**

## **SUMMARY**

Turkey poses a complex crustal structure as a result of the convergence of the Arabian and African plates. The North Anatolian Fault Zone (NAFZ) represents 1600 km long active right-lateral strike-slip fault system of the country that has caused several destructive earthquakes. Location of historical earthquakes indicates that the activity on the fault tend to migrate westward that was confirmed by the stress change measurements following the last Mw7.4 1999 Izmit Earthquake. In the western part of NAFZ, there is a seismic gap inside the Sea of Marmara. Reliable knowledge of physical properties of the crustal structure of the unruptured segment within the Sea of Marmara is crucial for proper seismic hazard assessments given that the city of Istanbul, a metropolitan city with its millions of habitats, is closely located to this seismic gap. Although there have been several studies of examining the crustal structure of the Marmara Region and surroundings at different depth scales, the resolution of collected data inside the Sea of Marmara and thus resultant model from, i.e., seismic local earthquake tomography is not good enough mainly due to the lack of seismic instrumentation. The ambient seismic noise tomography eliminates this problem because in this method, every seismometer act as a source. The cross-correlation between two receivers gives the Green's function which contains structural information about the region beneath seismometers.

In this thesis work, the Transdimensional Bayesian tomography, for the first time, has been applied to obtain a high-resolution image of the crustal structure of northwestern Turkey. For forward estimation of traveltimes information for a given velocity model, we used the Fast Marching Method (FMM). Prior to this, we applied a rather simple and computationally fast 2-D nonlinear tomography scheme to have a rough idea on group velocity variation in the regions. We used a Bayesian framework to invert traveltimes residual extracted from Green's functions for the Rayleigh wave group velocity models at various frequencies.

The advantage of this framework is that it allows an adaptive model parametrization using irregular Voronoi cells varying in size and shape depending on data resolution conditions in the model space. Moreover, the inversion scheme is independent from the damping and smoothing parameters and it gives a probability distribution of the complete solution which enables uncertainty estimation of the results as.

Our high-resolution tomographic images included group velocities of Rayleigh waves resolved between 1 sec and 20 s. The tomographic maps of lateral variation successfully revealed the basin structures such as Çınarcık, Tekirdağ, and Adapazarı Basins between periods 1 and 10 s that are characterized by typically low group velocities with low uncertainties in this study. The low-velocity zones mark well sign of deformations along the NAFZ in the crust and the complex structure due to the active tectonics of the Anatolia. Finally, different tectonic units, in particular, to the

east were identified from each other as our maps highlight Istanbul-Zonguldak Zone from Armutlu-Almacik Block with a sharp high to low-velocity change in N-S direction.



# ARKA ALAN SİSMİK GÜRÜLTÜ TOMOGRAFİ YÖNTEMİ KULLANILARAK KUZEY ANADOLU FAY ZONU (KAFZ) VE KUZEYBATI TÜRKİYE'NİN KABUK YAPISININ YÜKSEK ÇÖZÜNÜRLÜKTE GÖRÜNTÜLENMESİ

## ÖZET

Sismoloji, diğer jeofizik yöntemler ile karşılaştırıldığında, yer içerisinde meydana gelen jeodinamik olayları (yitim zonu dinamikleri, manto konveksiyon akımları vs.) ve bunun sonucunda şekillenen tektonik yapıların oluşma süreçlerini daha iyi anlamada etkin bir bilim dalıdır. Yer içerisinde fiziksel özelliklerini (sismik hız, zayıflık zonları, anizotropi, vb.) kabuk, manto ve çekirdeğin yapısını görüntüleme sismolojideki en güçlü araçlardan biri sismik tomografidir. Çeşitli sismik tomografi problemlerinin temel amacı, ortamın fiziksel koşullarına (yoğunluğa, sıcaklığa, kimyasal bileşenlerine, vb.) bağlı olan sismik dalga hızı varyasyonunu belirlemektir. Yerkürenin heterojenliği sismik dalgaların yayılma hızını etkiler, bu nedenle sismik dalgaların seyahat zamanları değişim gösterir. Bilinen bir referans hız modeline göre seyahat süresi anomalileri, yayılma yolu boyunca yer altı yapısının görünür karakterini temsil eden ve ters çözüm işlemi boyunca kullanılabilen gözlem verilerini oluşturur. Genel olarak sismik tomografi, fay zonlarında, volkanik veya jeotermal alanlarda, dalma batma zonlarında vb. sismik hızdaki ani değişiklikleri belirlemek için kullanılır.

Marmara Denizi'nin altında bulunan sismik boşluk boyunca potansiyel olarak beklenen büyük bir depremin meydana gelmesi ve olası hasarlar hakkında uzun zamandır bilimsel tartışmalar yapılmaktadır. Yırtılma yayılımını daha iyi simüle edebilmek ve olası hasarı değerlendirmek için, yırtılma bölgesinin altındaki kabuk yapısı içerisindeki çeşitli fiziksel özellikler hakkında güvenilir ve yüksek çözünürlüklü bir bilgiye sahip olmak esastır. Zayıflık bölgelerinin uygun konumunun ve sismik dalga hızlarındaki malzeme özelliklerinin belirlenmesi, potansiyel kırılma alanlarının yakınındaki bölgelerde sismik riski değerlendiren mühendisler için önemli bir bilgi olacaktır. Bununla birlikte, fay zonları boyunca kabuk özelliklerinin doğru görüntülenmesi, esasen kabuk ve manto içindeki sismik çözünürlük sınırlamaları nedeniyle belirsiz kalmaktadır. Bu çalışmada temel hedefimiz, KAFZ ve çevresinin kuzeybatı kesiminde yeni bir yüksek çözünürlüklü kabuk modeli geliştirmektir.

Türkiye, Arap ve Afrika levhalarının birbirine göre yaklaşan hareketlerinden dolayı oldukça karmaşık bir tektonik yapıdadır. Bununla ilişkili olarak heterojen bir kabuk yapısına sahiptir. Kuzey Anadolu Fay Zonu (KAFZ), 1600 km uzunluğunda aktif sağ-yanal atımlı bir fay sistemi olup geçmişte birçok yıkıcı depreme sebebiyet vermiştir. Tarihsel depremlerin oluş yerleri, fay üzerindeki aktivitenin batıya doğru göç ettiğine işaret eder. Yakın zamanda meydana gelen Mw7.4 1999 İzmit depremi sonrası hesaplanan stres değişiminin yönelimi de bu gözlemi destekler niteliktedir. KAFZ'ın batı kısmında, Marmara Denizi içerisinde, henüz kırılmamış bir sismik boşluk yer almaktadır. 15 milyondan fazla bir nüfusa sahip İstanbul'un, Marmara Denizi içerisinde geçen fay sistemine yakınlığı da düşünüldüğünde, bu boşluk altında kalan kabuk yapısının fiziksel özelliklerinin güvenilirliğinin bilinmesi, bölgede sismik

tehlike deęerlendirmelerinin doęru bir Őekilde yapılabilmesi iin hayati derecede nem arz etmektedir. Marmara Blgesi ve yakın evresinin kabuk yapısını ele alan birok alıŐma mevcuttur, fakat bu alıŐmalar genellikle deniz ierisindeki srekli alıŐan deprem kayıt istasyonlarının sınırlı sayıda olmasından dolayı dŐk znrlkldr.

zellikle son dnemde, sismik istasyonlarda kaydedilen her bilgiyi kullanmanın nemi artmıŐtır. rneęin arka alan sismik grlt bilgisi alıŐalagelmiŐ deprem kaydından ziyade sismik istasyonlara gelen bir veri grubudur. Arka alan sismik grlts, okyanus-kıta birleŐmesinin ve insan faaliyetlerinin etkisinin genellikle yoęun olduęu bir bilgi kaynaęını temsil eder.

Deprem veya patlamalardan kaynaklanan sismik dalgaların kullanımında sınırlamalar vardır. Bu sınırlamalar ierisinde, patlatmaların yksek maliyeti, sismik istasyonların ve depremlerin homojen olmayan daęılımları sayılabilir. Yakın zamanda geliŐtirilen ve iki istasyon ifti arasında kaydedilen grlt analizlerine dayanan, arka alan sismik grlt tomografi alıŐmaları bu sorunu bir lde telafi eder. Arka alan sismik grlt kullanmanın avantajı, deprem veya patlatma gibi yer sarsıntısı iin zorlu bir kaynak gerektirmemesidir. Bu tip bir modelleme ynteminde her bir istasyon bir kaynak olarak deęerlendirilip, iki alıcı (istasyon) arasında elde edilen z iliŐki fonksiyonu Green fonksiyonunu verir. Green fonksiyonunu elde ederek, bir istasyon iftinin arasındaki yapı hakkında bilgi sahibi olmak mmkndr.

Bu tez alıŐmasında, kuzeybatı Trkiye'nin yksek znrlkl kabuk yapısını elde etmek amacıyla ilk defa boyut tesi Bayesian tomografi yntemi kullanılmıŐtır. Blgenin yksek znrlkl kabuk yapısını grntlemek amacı ile, blgedeki 112 geici, 84 srekli alıŐan geniŐbant ve kısa sreli sismik istasyonların srekli kayıtları kullanıldı. Ardından, sismik istasyonların dikey bileŐenleri arasındaki sismik grlt apraz korelasyonları yapılarak Green fonksiyonları elde edildi. Toplamda, 24310 adet Green fonksiyonları el ile seilerek elde edildi. Grup hız bilgilerini Green fonksiyonlarından ıkarmak iin Green fonksiyonlarına dar bantlı Gauss filtresi uygulandı. Bu aŐamada 1 ile 20 saniye periyot aralıęı kullanıldı.

Seyahat zamanlarının verilen bir model iin dz hesaplanması amacıyla *Fast Marching* yntemi kullanılmıŐtır. Blgedeki yzey dalgası grup hızlarının yaklaşık olarak belirlenebilmesi iin Bayesian tipi ters zm ncesinde, hesaplama olarak daha hızlı ve varıŐ zamanı rezidyellerinin direkt ters zmne olanak veren, nispeten daha basit iki boyutlu bir yntem kullanılmıŐtır. Ardından benzer bir Őekilde Bayesian sistemi kullanılarak Green fonksiyonlarından elde edilen varıŐ zamanı rezidyellerinin direkt ters zm elde edilmiŐtir. Bunun sonucunda, bu yntem ile de farklı frekanslarda grup hızlarına ulaŐılmıŐtır. Bayesian tipi ters zmnn kullanımı avantajlı grlmektedir nk bu tip bir optimizasyon sırasında, Voronoi hcrelerinin yardımı ile modelleme alanı ierisindeki veri znrlęnn Őartlarına baęlı olarak deęiŐen ebat ve biimlerde dzensiz bir parametrizasyona olanak saęlar. Ayrıca, ters zm algoritması, klasik anlamda tomografi yntemlerinden farklı olarak, elde edilmek istenen model parametreleri üzerinde snmleme ve/veya dzleŐtirmeye imkn veren parametrelere baęımlı deęildir. Bayesian yaklaŐımı elde edilen btn zm setinin olasılık daęılımını vererek bir nevi zmlerin belirsizlięi hakkında da bilgi saęlar.

Elde edilen tomografik haritalar Rayleigh tipi yzey dalgalarının grup hızlarının 1 ve 20 saniyelik periyotlar arasında iki boyutlu daęılımlarını temsil ederler. Tomografik haritalar, araŐtırma blgesindeki yksek znrlkl dŐk grup hızları ile karakterize edilen ımarcık, Tekirdaę ve Adapazarı gibi havza yapılarını ortaya

çıkarmıştır. KAFZ boyunca gözlemlenen düşük hız zonları, süregelen aktif deformasyonun izlerini işaret etmektedir. Araştırma bölgesinin doğusunda kalan, farklı ve karmaşık tektonik yapıları içeren kısımda, grup hızı dağılımları K-G yönünde düşük hızdan yüksek hıza geçişler göstererek İstanbul-Zonguldak zonuunun Armutlu-Almacık bloğundan farklılık gösterdiğine işaret eder.





## 1. INTRODUCTION

Recent technical advancements in data collection and computational facilities have made seismology become an extensive field of earth sciences in understanding the physical properties of the Earth's interiors, (i.e., seismic velocity, attenuation, anisotropy, etc.) compared to other geophysical methods. The major instrument utilized in the field of seismology, seismic waves, are elastic waves generated by earthquakes or explosions (Stein and Wysession, 2009) and propagate inside the Earth by carrying information from various parts, i.e., the crust, the mantle and from much deeper core structure. In general, there are two types of seismic waves existing: the body waves (P and S waves), and the surface waves (Rayleigh and Love waves). Surface waves usually propagate slower than the body waves. Rayleigh waves exhibit an elliptical and retrograde type of particle motion at the surface (Stein and Wysession, 2009). They are dispersive waves, in other words, wave speeds of Rayleigh waves change with frequency. Surface waves were identified by two types of velocities: phase and group velocities. The phase velocity is represented by the ratio of angular frequency with the wave number ( $v_p = \frac{\omega}{k}$ ) and indicates the velocity of a single wave travelling in space. The group velocity that is the velocity of superimposed waves travelling in space can be found via the derivative of the angular frequency with the wave number ( $v_g = \frac{d\omega}{dk}$ ) which is the velocity of superimposed waves travel in space. The group velocity has a lower frequency than the phase velocity (Shearer, 2009) (Figure 1.1). Type of source whether natural (i.e., earthquakes), or man-made (i.e., quarry-blasts, seismic vibrator, hammer, etc.) can all generate these seismic waves with different penetration depth capabilities that have an influence on spatial resolution.

Seismic imaging efforts that are based on the use of these waves may differ depending on the approach. In general, imaging techniques that benefit from inversion strategies or depend on the depth migration of directly stacked data are the most popular ones.

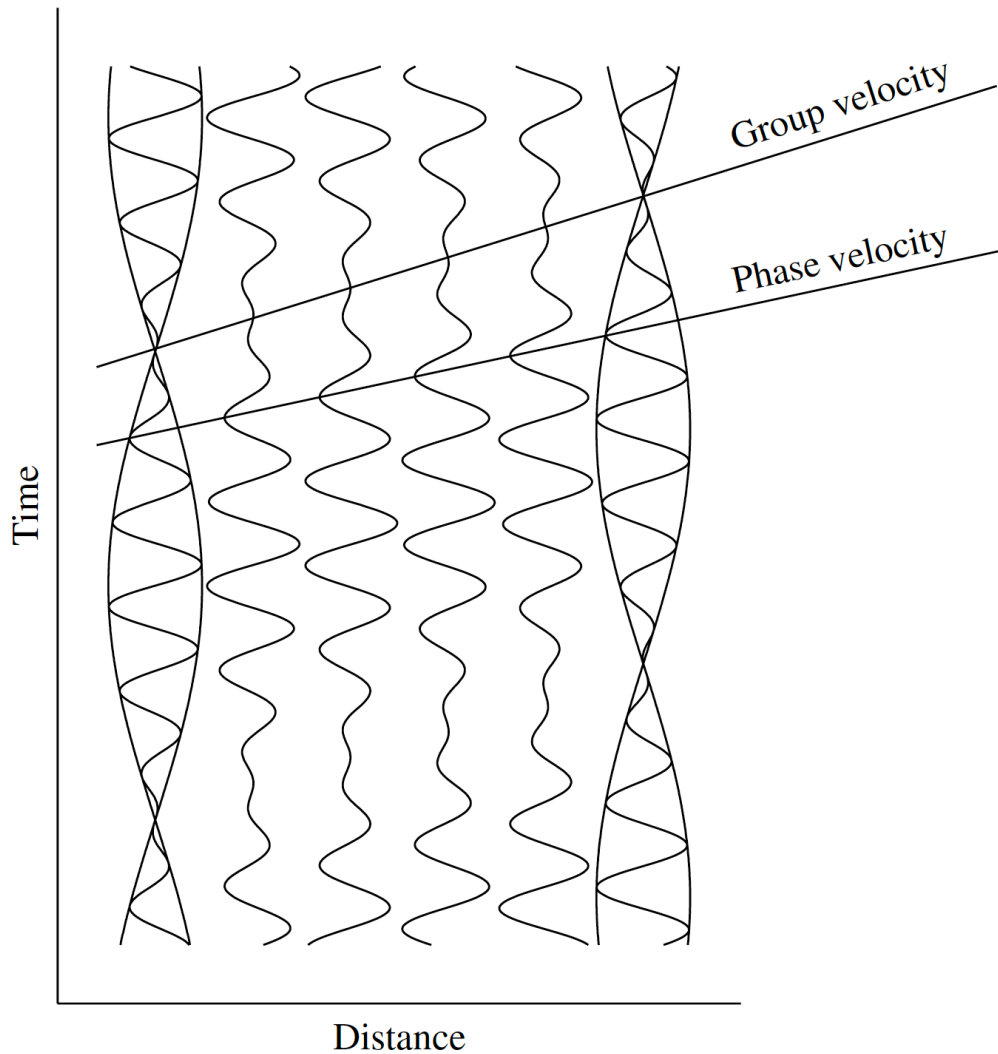


**Figure 1.1:** A schematic view of the difference between group velocity and phase velocity. The sum of two sinusoidal waves with a different frequencies and wavenumbers. The velocity of individual peaks represents the phase velocity and the velocity of the wave packets represents the group velocity (Shearer, 2009).

Inhomogeneity within the Earth's interior becomes larger and less significant at depths. In addition to this, in various tomographic inversion, or receiver function stacking problems we struggle with finding data with decent resolution. Resolution of information for the subsurface structure usually decreases with increasing depth. In some certain cases, where seismic activities are low and man-made seismic sources are restricted, our knowledge of crustal and mantle structure can be poor in local scale but relatively strong considering a global spatial resolution. This is because there is a huge amount of ray paths that sample Earth's interior by ensuring full global coverage due to the irregular distribution of earthquakes and seismic stations.

Seismic tomography is one of the most powerful tools in seismology to image the structure of crust, mantle and core. It is essentially considered as an inverse problem. It starts with the spatiotemporal measurement of wave energy variation emitted through a medium at a certain location by a seismometer. The main purpose of various seismic tomography problems is to determine seismic wave speed variation that strongly depends on the physical conditions of the medium, i.e., density, temperature, compositional, etc. The heterogeneity of the Earth affects propagation speed of seismic waves so that their travel times. Hence, travel time anomalies that can be established with respect to a known reference velocity model, i.e., IASPEI91 (Kennett and Engdahl, 1991), PREM (Dziewonski & Anderson, 1981) form our observed data, which represent apparent character of subsurface structure along the propagation path and can be utilized within the inversion process.

Tomography method earlier was first used in the field of medical sciences to identify anomalies in the human body. The first application of seismic tomography has been done in the 1960's (e.g. Bois et al., 1971; Aki et al., 1977; Aki & Lee, 1976; Dziewonski et al., 1977). The travel time anomalies of the surface waves were calculated by referencing a symmetrical site model and these anomalies were evenly distributed along the ray path (Lay and Wallace, 1995). In general, seismic tomography is used to determine sudden changes in seismic velocity in fault zones, in volcanic or geothermal areas, in subduction zones etc. Tomography requires to have sources and receivers. Even though there are numerous seismic stations all over the world, most of them are land stations. The number of sensors in oceanic environments such as Ocean Bottom Seismometers (OBS) is poorly distributed relative to the continents. This poor coverage gives rise to weak resolution for seismic velocity images beneath certain regions of the world.

During the last decade, seismologists have become aware of the importance of using every information recorded at seismic stations. Seismic ambient noise, in particular, represents the source of information where the combined effect of ocean-solid earth coupling and human activities are usually dense. Such effects can propagate over large distances and performing cross-correlation over continuous noise recordings across a simultaneously operating seismic array can yield the Earth's body and surface wave responses (Green's function). The seismic wavespeed variation between two stations is hidden within these Green's functions. Surface wave part of the Green's function

with significant dispersive behaviour can be examined to elucidate sub-surface seismic wave speed characteristics.

The present thesis work deals with revealing seismic wave properties (group velocities of surface waves) in the crust along the western segment of the North Anatolian Fault Zone (NAFZ). To achieve this we make use of travel time residuals extracted from cross-correlations between station pairs within a merged array including temporary and permanent broadband/short period stations in the study area. In the first chapter of this thesis, tectonic setting of the area and surroundings as well as our main motivation for this study are presented. A literature review concerning the previous geophysical studies carried out in the area, in particular, ambient seismic noise and seismic tomography studies, are given in chapter two. In chapter three, the ambient seismic noise tomography, the nonlinear and Transdimensional Bayesian tomography methods are described. Chapter four shows the steps of seismic data processing conducted in this study. Later, applications of the inversion to the processed observed data is presented in chapter five. Results from the ambient noise seismic tomography with Transdimensional Bayesian inversion and with the nonlinear inversion are presented and modelled group velocities are discussed in relation to the geology and the tectonic settings of the region in chapter six. Finally, the conclusion of this work is given in chapter seven.

## **1.1 Tectonic Settings of Turkey**

In Paleozoic-Mesozoic-Early Tertiary time scale, the Tethys ocean was located between Gondwana and Laurasia (Sengor and Yilmaz, 1981). The Neotethys started its opening in the Triassic. Between the Late Cretaceous to the Eocene the Neotethys oceanic branches closed, forming the present Anatolian plate (Taymaz et al., 2007). Turkey is made of different terranes which broke off from Gondwana. Then the collision with Eurasia during the Alpine orogeny formed the present Anatolian micro-plate (Okay and Tüysüz, 1999). The Anatolian plate is one of the most seismically active and continuously deforming plates due to its past and present tectonic evolution (Figure 1.2). The tectonic motion of Anatolia is controlled by the convergence of the Arabian and African plates with respect to the Eurasian plate (Mckenzie, 1972).

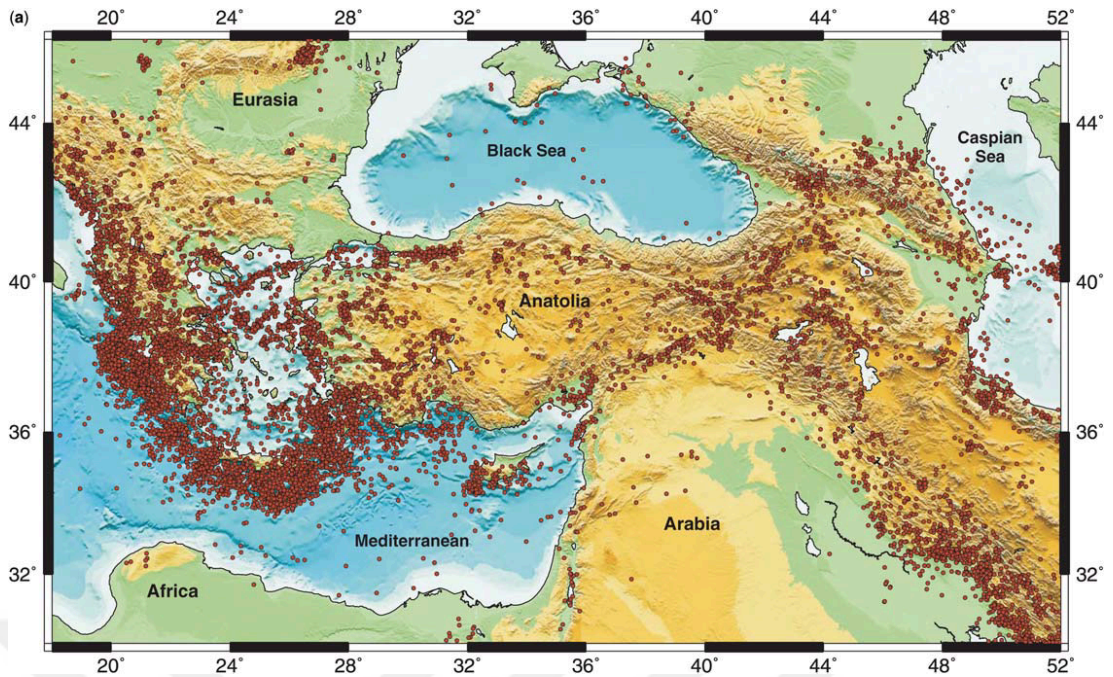


**Figure 1.2:** Seismicity of the Anatolian Plate and surroundings (Taymaz et al., 2007) for a period of 1973–2007.

### 1.1.1 Indications of the deformation from geodetic observations

The African plate is moving to the northeast at an average rate of 10 mm/yr with respect to Eurasia (McClusky et al., 2000) (Figure 1.3). Along the Hellenic Arc, African plate subducts beneath the Aegean Region and the southwestern part of Turkey. The slab-roll back of northward subducting African plate beneath the southern Aegean Region has led to back-arc extension regime and the crustal thinning and volcanism as well. The Arabian plate is moving northwest relatively to Eurasia at an average rate of 18 mm/yr (Mckenzie, 1972) (Figure 1.3). The convergence of the Arabian plate is responsible for a crustal thickening with the compression between Bitlis-Zagros fold and the Caucasus at the eastern Anatolia. As a consequence of the slab-rollback of Africa and the compression of Arabia, Anatolia is moving toward the southwest direction at a rate of 25 mm/yr (Figure 1.4) along two major shear deformation zones: the North Anatolian Fault Zone (NAFZ) and the East Anatolian Fault Zone (EAFZ). The dextral North Anatolian Fault System (NAFS) and the sinistral East Anatolian Fault System (EAFS) play an important role in the southwestward movement of Anatolia (Rotstein, 1984). The sinistral Dead Sea Fault System (DSFS) also has a role in the movement of the Arabian plate (Taymaz et al., 2007).

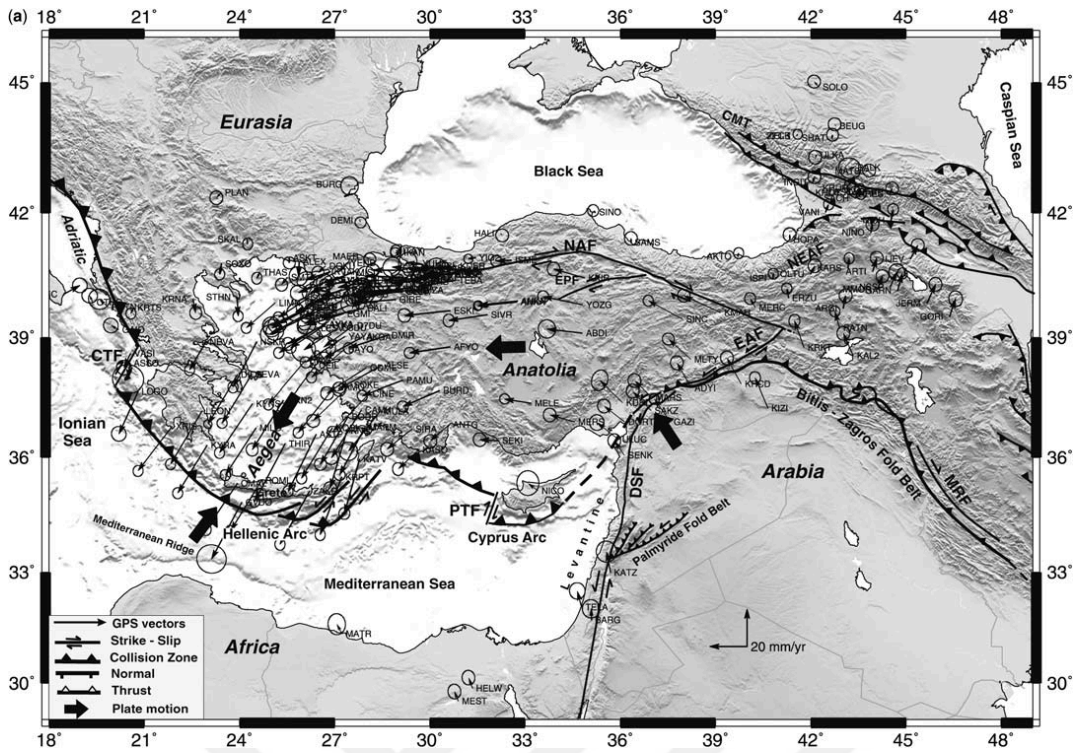


**Figure 1.3:** Map of major plate boundaries for the Anatolian plate and surroundings (Taymaz et al., 2007). GPS horizontal velocities represented by large black arrows indicate relative plate motions with respect to Eurasia (McClusky et al., 2003; Reilinger et al., 2006).

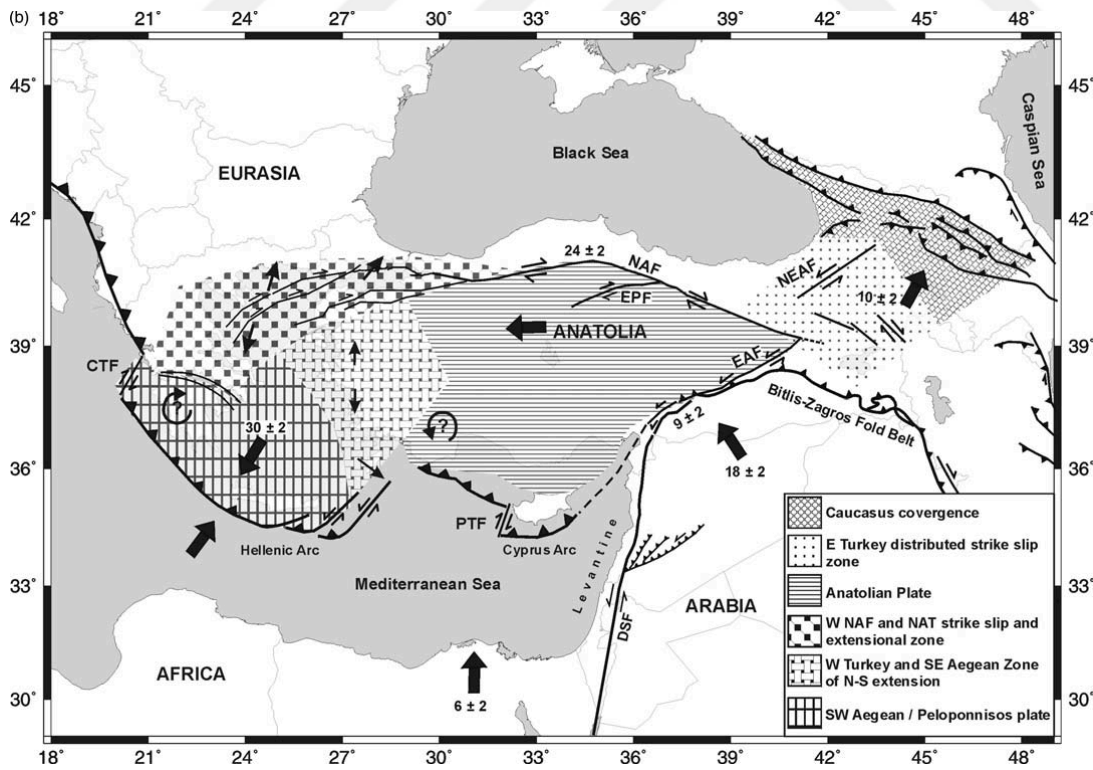


**Figure 1.4:** A schematic view of the tectonic settings in the Eastern Mediterranean (Taymaz et al., 2007). Large black arrows indicate relative plate motions with respect to Eurasia (McClusky et al., 2003; Reilinger et al., 2006).

### 1.1.2 Different tectonic zones of the study area

Turkey has been formed by the juxtaposition of terranes during the Mesozoic and Tertiary. The main geological features of Turkey are the Pontides, the Kırşehir Massif, the Anatolide-Tauride Block, and the Arabian platform (Sengor and Yilmaz, 1981) (Figure 1.5). The Pontides consist of three major terranes namely Strandja Terrane, Istanbul, and Sakarya Zones. The Pontides are separated from the Anatolide-Tauride Block and the Kırşehir Massif by the 2000 km long Izmir-Ankara-Erzincan suture which is the major suture in Turkey (Okay and Tüysüz, 1999). Along the Izmir-Ankara-Erzincan suture, the marks of the Tethys ocean are visible. The second longest suture in Turkey is the Intra-Pontide suture and it forms an 800 km long boundary between Sakarya and Istanbul zones in the east and between Sakarya and Rhodope-Strandja Massif in the west which extends into the Marmara Sea (Sengor and Yilmaz, 1981).

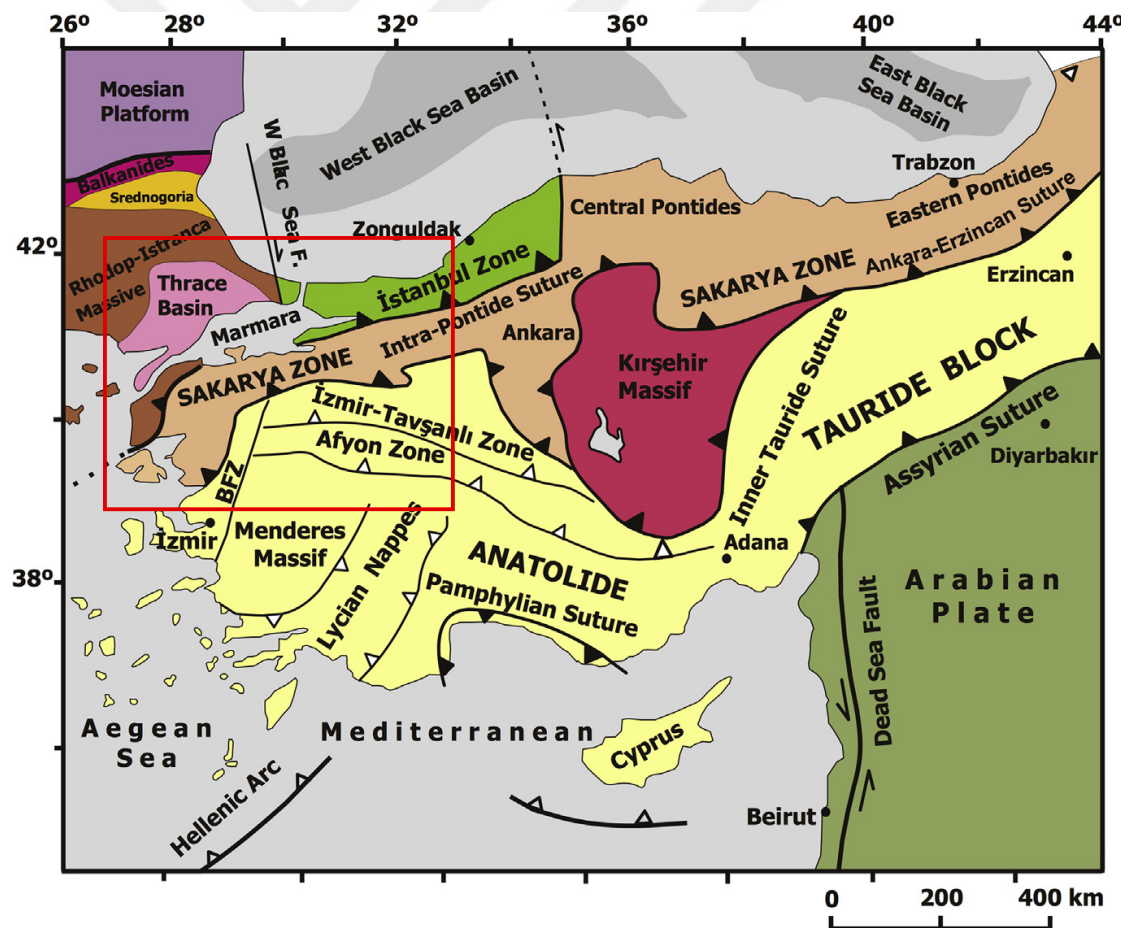


**Figure 1.5:** Major tectonic map of Turkey compiled from (Çubuk-Sabuncu et al., 2017; Okay and Tüysüz, 1999; Okay, 2008). Red square shows the study area.

The Istanbul zone is a 400 km long and 55 km wide continental fragment originally belonging to Laurasia (Gorur et al., 1997; Yilmaz et al., 1998; Okay and Tüysüz, 1999) that has a Precambrian crystalline basement overlaid by a continuous sedimentary sequence. The Sakarya zone is a 1500 km long and 120 km wide continental fragment which has metamorphic basement units, the Karakaya Complex and Oligo-Miocene granitoids (Okay and Tüysüz, 1999). The Rhodope-Strandja zone consists of the Rhodope-Strandja Massifs and the Thrace Basin. The Strandja Massif forms a 280 km long and 40 km wide northwest-southeast trending metamorphic belt on the eastern part of Strandja Zone (Okay et al., 2001). The northern part of Strandja Massif is a flysch-volcanic zone (Yilmaz et al., 1998) and the southern part is cut by NW-SE trending normal, lateral, and transpressional faults. It is bounded by the Thrace Basin which is an approximately 9 km thick sedimentary basin from Eocene-Oligocene age (Turgut, 1991; Gorur and Okay, 1996) overlying a basement of metamorphic rocks of the Strandja Massif (Alaygut, 1995; Yilmaz et al., 1998). To the south, the Thrace sedimentary basin extends beneath the Marmara Sea. The Armutlu-Almacik Zone is located between the Istanbul and Sakarya Zones, on the eastern margin of the Sea of Marmara. It consists of different metamorphic rocks which are a melange of Istanbul and Sakarya Zones.

### **1.1.3 The North Anatolian Fault Zone (NAFZ)**

The NAFZ crosses three zones, Istanbul, Sakarya and Armutlu-Almacik Zones and splits into two branches. The southern strand (SNAF) forms a boundary between Sakarya and Armutlu-Almacik Zones and the northern strand (NNAF) continues beneath Sea of Marmara. The NAFZ is one of the most seismically active strike-slip fault (Figure 1.2). It has an important role in the tectonic behaviour of the region. The NAFZ represents about 1600 km long transform plate boundary between the Arabian, African and Eurasian plates and it follows the Intra-pontide and Izmir-Ankara-Erzincan suture zones (Barka et al., 1992). It developed in early late Miocene after the Arabian and Eurasian plate collision (Sengor, 1985; Sengor et al., 1985; Dewey et al., 1989). The westward orientation of the stress can be deduced from the historical record of large earthquakes that affected the region (Stein, 1997). A series of several historical large earthquakes occurred along the NAFZ, which have taken place over about 900 km of its entire length, implying an overall westward migration of the earthquake occurrences (Ketin, 1948) (Figure 1.5). During the 20th century, the first severe failure

was initiated along the Ganos segment located at the westernmost of the NAFZ. The 1912 failure with magnitude  $M7.4$  caused a 50 km long surface break (Ambraseys and Finkel, 1987). In 1939, an earthquake of magnitude 7.8 to 8 occurred stroke the city of Erzincan. This was the largest earthquake ever recorded in Anatolia. It triggered the westward migration on NAFZ (Barka, 1996). It produced a 360 km long rupture from the Erzincan basin to Amasya (Figure 1.5). Then several earthquakes of lower magnitudes occurred along the NAFZ, with different earthquakes rupture zone lengths: the 1942 Erbaa-Niksar earthquake ( $M=7.1$ ; 50 km long rupture zone) (Pamir and Akyol, 1943; Ambraseys, 1970), the 1943 Tosya earthquake ( $M=7.6$ , 260 km rupture zone) (Ketin, 1969), the 1944 Bolu earthquake ( $M=7.3$ , 165 km rupture zone) (Ketin, 1969), the 1957 Abant earthquake ( $M=7$ , 30 km rupture zone from Abant to Arpaeski) (Barka, 1996), the 1967 Mudurnu earthquake ( $M=7.1$ , 80 km long rupture zone) (Ambraseys and Zatopek, 1969). The 1957 and 1967 earthquakes have ruptured the south segment of the Almacik Block. Most recently, 17 August 1999 Izmit ( $M=7.4$ ) and 12 November 1999 Düzce ( $M=7.2$ ) earthquakes ruptured a segment of 200 km long which is the northern segment of Almacik Block (Figure 1.5). The Izmit earthquake occurred on the seismic gap which Toksöz and Michael (1979) identified. Between Bolu and the eastern part of the ruptured segment of Düzce earthquake, no earthquake has happened yet. Akyuz et al. (2002) say that if this segment is already broken in 1944 or it will break causing an  $M < 6.5$  earthquakes. The historical earthquake records (Ambraseys and Jackson, 2000; [Fig 1b therein]) reveals that region remaining between the 1912 and 1999 ruptures forms a seismic gap in the Sea of Marmara (Barka et al., 2002).

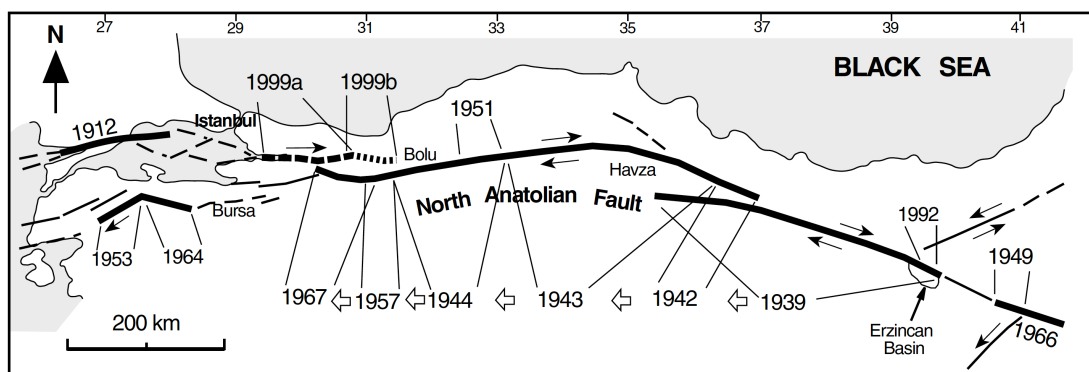


**Figure 1.6:** Historical earthquakes that occurred along the NAFZ (Barka et al., 2002).

#### 1.1.4 The Sea of Marmara

To the west of the NAFZ, the fault tends to become shorter, discontinuous and often stepped through various basins, i.e., the Iznik, Bursa, Karacabey, Manyas and Marmara Sea basins (Barka and Kadinsky-Cade, 1988). Among these basins, Marmara Sea is the largest one with its 280 km long and 80 km wide marine basin and is represented by several complex structures developed within a zone of interaction between the extensional and the strike-slip shear structures (Gürer et al., 2006). The Sea of Marmara has two parts, the southern part with shallow shelf and the northern part with deep basins up to 1250 m water depth (Carton et al., 2007). In the eastern part of the Sea of Marmara, there is a shelf with a width of 7 to 13 km (Okay et al., 2000).

The NAF enters the Sea of Marmara from the Gulf of Izmit as a single strand, continues through the north of Çınarcık Basin as a fault segment and turns to the east-west direction (Figure 1.6) (Le Pichon et al., 2001). The Çınarcık Basin is 50 km long and 18 km wide with water depths ranging between 1270 to 1150 m (Okay et al., 2000, Carton et al., 2007). The NAF splits into two branches in the east as the North Boundary Fault (Wong et al., 1995) and the Inner Boundary Fault which are the boundaries between the northern slope, the southern slope and the Çınarcık Basin (Okay et al., 2000). The North and Inner Boundary faults form a negative flower structure due to the steepness of the North Boundary fault compared to the Inner Boundary fault (Okay et al., 2000). The Çınarcık basin is bounded by the Central Marmara Ridge in the west where there are thrust faults and folds. More to the west a small basin called Kumburgaz Basin is located which is bounded by the Central Marmara Fault (CMF). The North Boundary fault is the continuation of the CMF to the east and together forms a segment of the NAF that joins the Ganos fault to the west (Figure 1.7).

The three segments beneath the Marmara Sea are; the Ganos segment (15 km long) which could have been broken during the 1912 earthquake (Ambrasseys and Finkel, 1987), the Central Marmara segment (105 km long) which has not experienced any rupture since 1766 (Okay et al., 2000), and the North Boundary segment (45 km long) which was broken during the 1894 earthquake (Ambrasseys and Finkel, 1987).

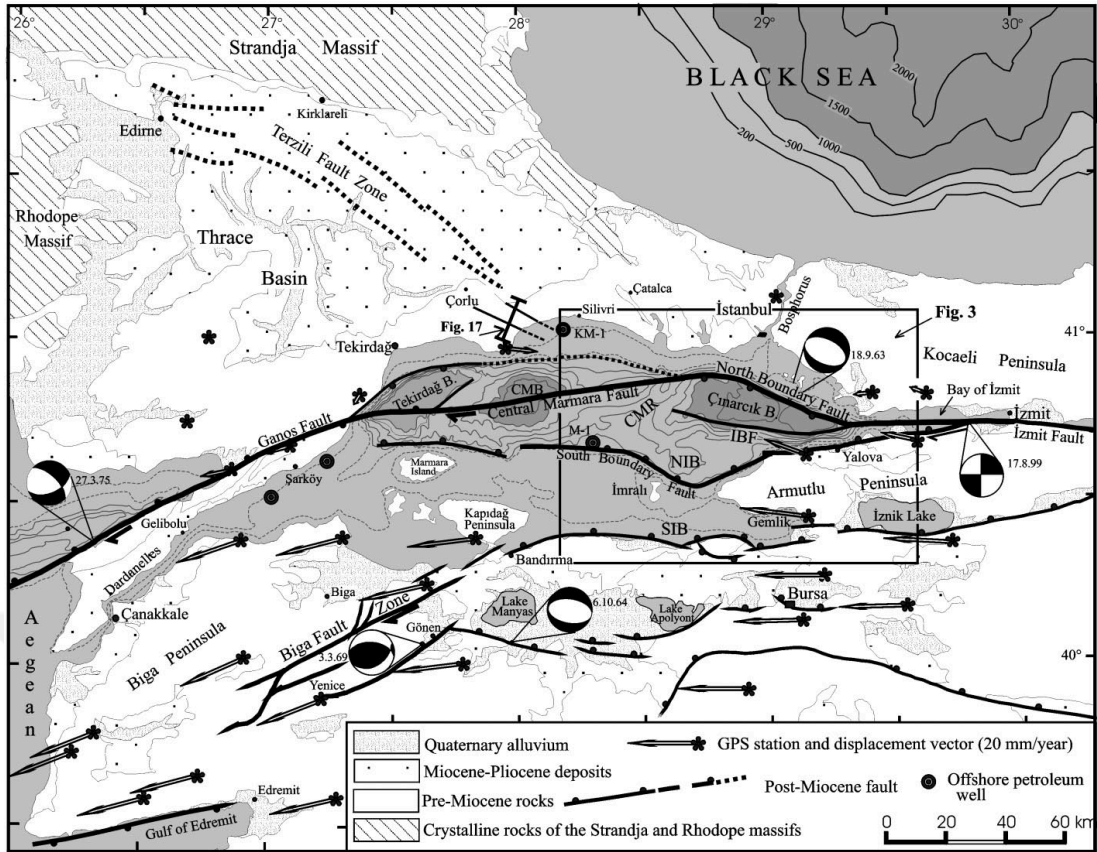


**Figure 1.7:** Tectonic settings of the Marmara Region (Okay et al., 2000).

## 1.2 Main Purpose of the Study

For a long time, there has been a scientific debate on the possible occurrence and the location of a major earthquake which is expected to potentially nucleate somewhere along the seismic gap previously described beneath the Sea of Marmara. To be able to better simulate the rupture propagation and assess the possible damage, it is essential to have a reliable and high-resolution knowledge of various physical properties within the crustal structure beneath the rupture zone. This will enable high-resolution mapping of weakness zones and their depth extent that can significantly contribute to our understanding on whether shear deformation is localized in a narrow brittle zone or it expands into wide, distributed deformation bands at depths (Platt and Behr, 2011), presumably accommodated by lower crustal ductile flow (Bürgmann and Dresen, 2008). Proper location of weakness zones and its material properties in seismic wave speeds would be an important proxy for engineers who evaluate potential seismic risk in regions nearby potential rupture areas.



permanent and temporary seismic networks. Finally, we applied a Transdimensional Bayesian inversion algorithm (Bodin et al. 2012) performed over Rayleigh wave Green's functions in order to develop a high-resolution shear wave velocity model beneath north-western part of the NAFZ including the Sea of Marmara. Employing a Bayesian strategy in the modelling can be advantageous in making robust interpretations of the models since a probability density is determined a priori to prevent from the consideration of unrealistic earth models. The posterior distribution of proposed models provides a statistically rigorous appraisal of model uncertainty.





## 2. PREVIOUS STUDIES

Early seismic studies to characterize the structure of the NW Turkey have been performed by different methods at various scales. Biryol et al. (2011) applied the teleseismic P-wave traveltimes tomography to obtain a structural image of the deeper lithosphere and mantle of Anatolia in regional scale. They observed fast seismic anomalies represent subducting African plate beneath Anatolia. Slow velocity anomalies within the mantle wedge just beneath Anatolia was attributed to the presence of hot upwelling asthenosphere in the same study. As being different from Biryol et al. (2011), Fichtner et al. (2013a,b) examined the same region via multi-scale full waveform tomography to image the deep structure of the NAFZ. They observed a low-velocity zone beneath the NAFZ which corresponds to the upper mantle expression of the sutures (Figure 2.1). Beside this, various seismic imaging efforts including, i.e., Gans et al. (2009) and Mutlu and Karabulut (2011) applying Pn tomography; Bakırcı et al. (2012), Salaün et al. (2012) and Delph et al. (2017) using surface wave tomography; Warren et al. (2013) applying ambient noise tomography and Çubuk-Sabuncu et al. (2017) using full-waveform tomography, Kind et al. (2015), Licciardi et al. (2018) using receiver function analyses have delineated both heterogeneous and anisotropic character in the crustal upper mantle structure of Anatolia and its adjacents in details.

In a similar region overlapping our study area, Polat et al. (2016) have recently imaged the crustal structure of northwestern Turkey by using local earthquake tomography and they observed high-velocity anomalies beneath the NAFZ and low velocities beneath the central Sea of Marmara (Figure 2.2). Çubuk-Sabuncu et al. (2017) applied a full-waveform tomography that benefits from the adjoint method in a larger area covering western Turkey. Their results revealed the strong velocity variations down to the depth of 35 km. More locally, Koulakov et al. (2010) investigated the crustal structure of the western part of the NAFZ using local earthquake tomography. They proposed a model for pull-apart basins that is consistent with their low-velocity zones and high attenuation model findings in the area.

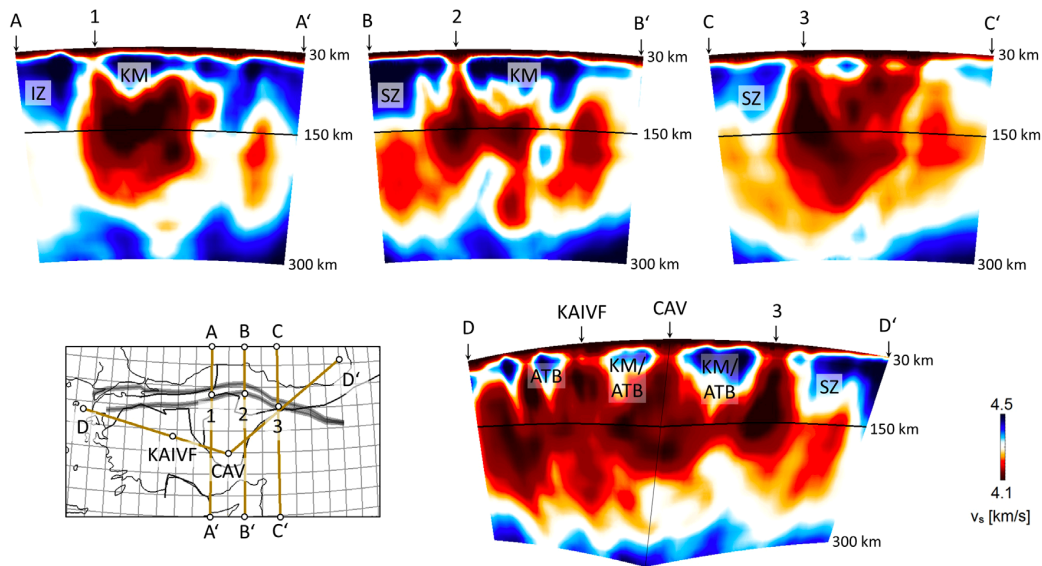


**Figure 2.1:** The full-waveform tomographic inversion results of Fichtner et al. (2013a,b) shows the vertical slices of  $V_s$ . ATB: Anatolide–Tauride Block, CAV: Central Anatolian Volcanics, IZ: İstanbul Zone, KAIVF: Kirka–Afyon–Isparta Volcanic Field, KM: Kırşehir Massif, SZ: Sakarya Zone.

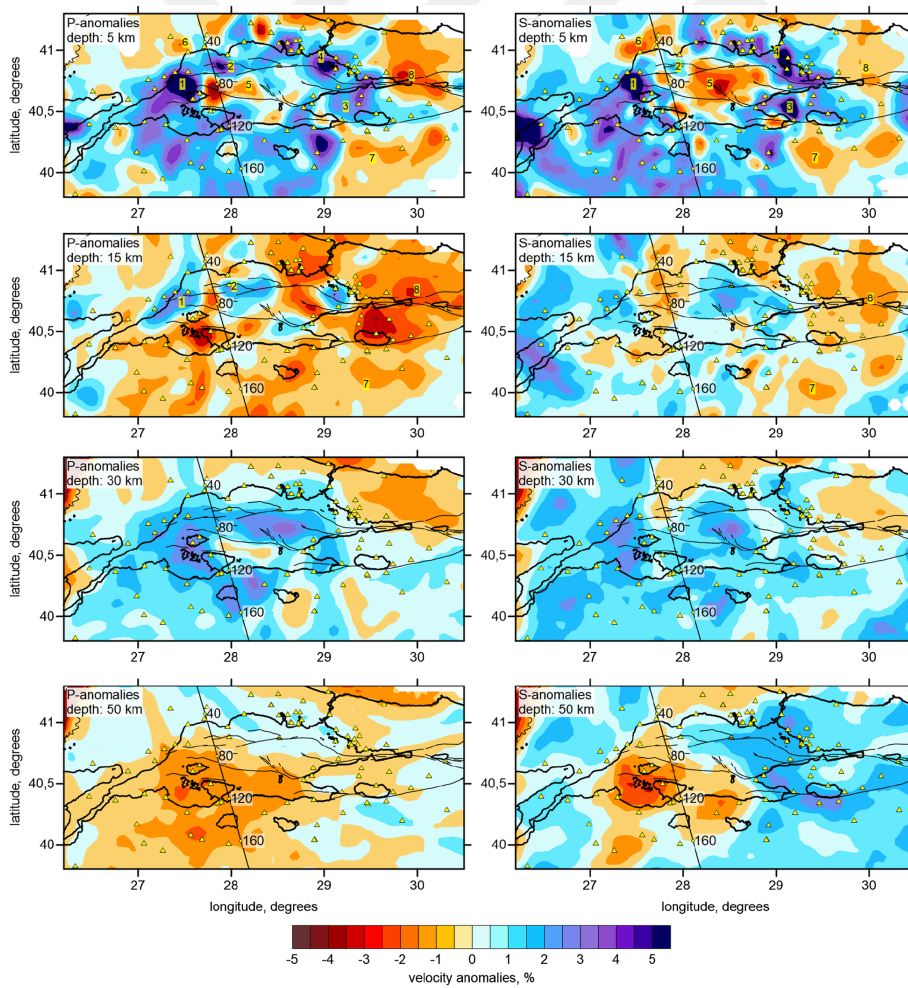


**Figure 2.2:** P and S velocity anomaly results for 5, 15, 30 and 50 km depths obtained by Polat et al. (2016).

Kahraman et al. (2015) applied receiver function method on teleseismic observations recorded at Dense Array for North Anatolia (DANA) network to the western part of the NAFZ and they were able to detect low-velocity zones and different Moho depths in the northern and southern parts across the NAFZ. Recently, Papaleo et al. (2017, 2018) applied teleseismic tomography study by using the data set extracted from the DANA network. Their results have suggested the presence of a high-velocity body between the two branches of the NAFZ and clearly imaged deeper extension of a widening weakness zone toward the upper mantle depths (Figure 2.3).

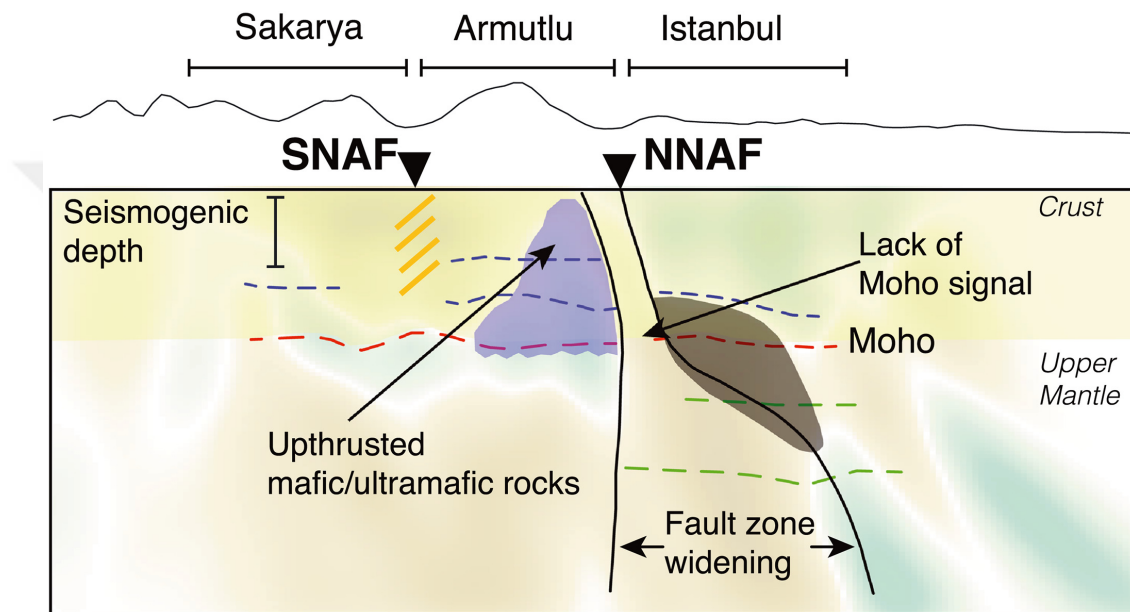


**Figure 2.3:** The fault model for the geometry of NAFZ by Papaleo et al. (2018).

Focusing on the westward to the Sea of Marmara, there have been a large number of seismic experiments aiming at delineating sea bottom and complicated faulting network conducted within the last 20 years. Hence, the Sea of Marmara has become one of the most well-known intra sea in terms of its shallow crustal features. For instance, the first deep seismic study has been done by Laigle et al. (2008). They detected a reflective lower crust and the Moho boundary. Bayrakci et al. (2013) applied a 3-D tomographic inversion of controlled source data and developed seismic velocity models down to 8 km below the sea level for the Sea of Marmara. These model results indicated prominent basement depressions beneath three basins. Other studies about the Sea of Marmara and surroundings including the NAFZ that were performed by Okay et al. (1999), Parke et al. (1999), Le Pichon et al. (2001), Yaltrak (2002), Armijo

et al. (2002, 2005) proposed various fault models for the geometry of the NAFZ beneath the Sea of Marmara.

Several other geophysical investigations have been conducted including such as geoelectrical imaging based on magnetotelluric data inversions (e.g. Honkura et al., 2000; Tank et al., 2005; Kaya et al., 2009; Kaya et al., 2013) that has significantly contributed to elucidating of shallow/deep crustal depth structures. N-S profiles cutting the fault zones revealed clear transitions between conductive and resistive zones with varying extent related to different segments of the NAFZ. Another imaging approach that is based on the auto-correlation of ambient seismic noise data extracted from the stations traversing various accretionary complexes (e.g. Istanbul Zone, Sakarya Terrane, Armutlu-Almacik Block) to the west of the Sea of Marmara resulted in reflection profiles indicating a Moho reflected P wave and additional structure within the crust and upper mantle (Taylor and Houseman, 2016).

### **3. AMBIENT SEISMIC NOISE TOMOGRAPHY**

#### **3.1 Imaging with Noise**

Seismic waves are elastic waves caused by natural sources (e.g. earthquakes) or artificial sources (e.g. explosions) (Stein and Wysession, 2009). The study of the propagation of different types of seismic waves (body waves, surface waves) into the Earth provides information about the structure of the Earth's interior. Surface waves (Rayleigh and Love waves) are dispersive types of waves and thus relevant velocities of surface waves can be obtained for different frequencies. This also indicates the depth varying character of surface wave speeds. Continuous digital recordings with certain sampling rates (sampling frequencies) extracted from seismic stations contain valuable information about body waves and surface waves released after an earthquake or explosion but also after any type of waves in relation to any other ground shaking factors, for instance, human activities, small vibrations of the Earth, etc (Lay and Wallace, 1995). The latter usually tend to generate random seismic wavefield and usually referred to the seismic noise on seismograms.

The origins of the seismic noise are the seismic hum, the microseisms and the microtremors. The frequencies of the seismic noise range between  $10^{-3}$  Hz and 100 Hz (Nishida, 2017). The microtremors are high-frequency noise greater than 1 Hz and are produced by human activities (traffic, heavy machines etc.) (Bonnefoy-Claudet et al., 2006). The microseisms are continuous oscillations of the ground (Lounguet-Higgins, 1950) produced by oceanic gravity waves (ocean swell), wind waves, and ocean infragravity waves (Nishida, 2017). Below 1 Hz, the ambient seismic wavefield classifies into; the seismic hum (1-20 mHz), primary microseisms (0.02-0.1 Hz) and secondary microseisms (0.1-1 Hz) (Figure 3.1). The excitation of microseisms is related to changing weather conditions and ocean swell activity (Figure 3.2). They are the result of intersections between the ocean, climate and lithosphere. Thus, it should be considered as an ocean-atmosphere-solid earth coupled system (Tanimoto et al., 1998).

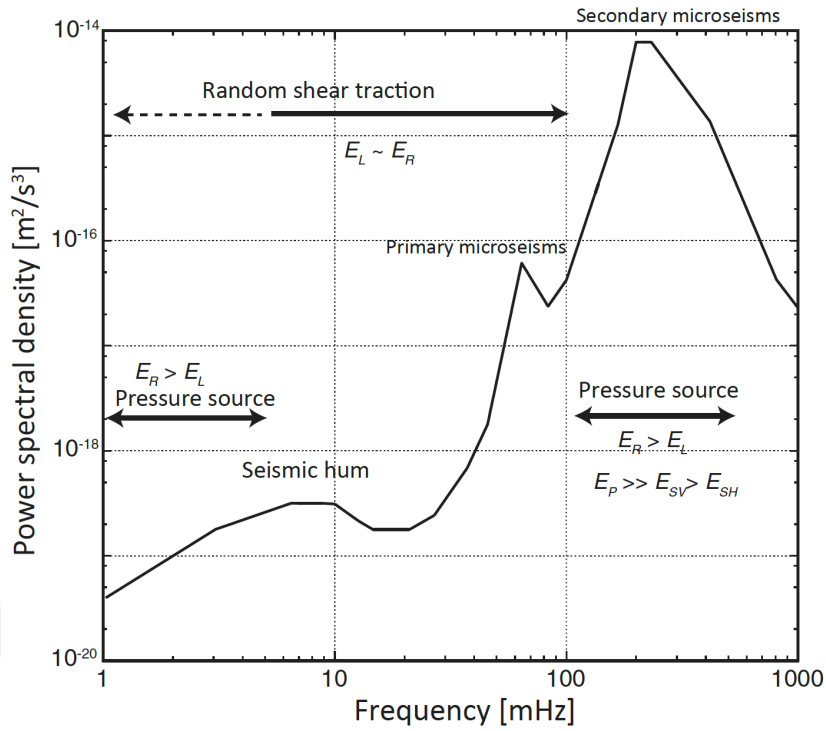
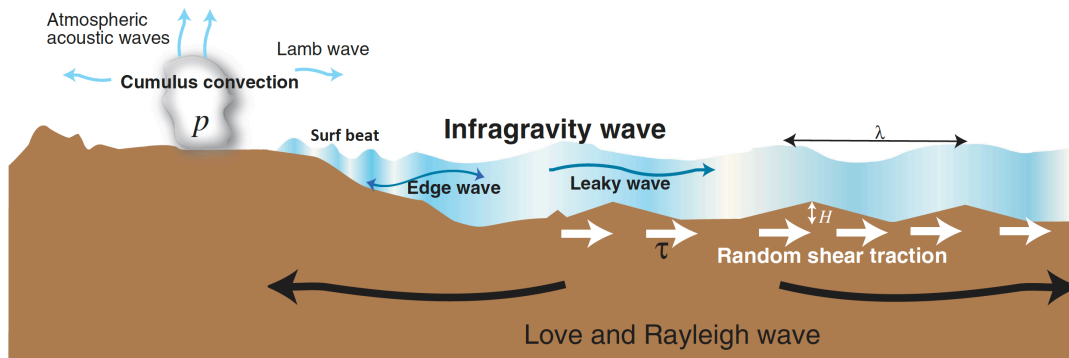


**Figure 3.1:** The schematic view of frequency range of ambient seismic wavefield (Nishida, 2017).

**(a) Seismic hum**



**(b) Microseisms**

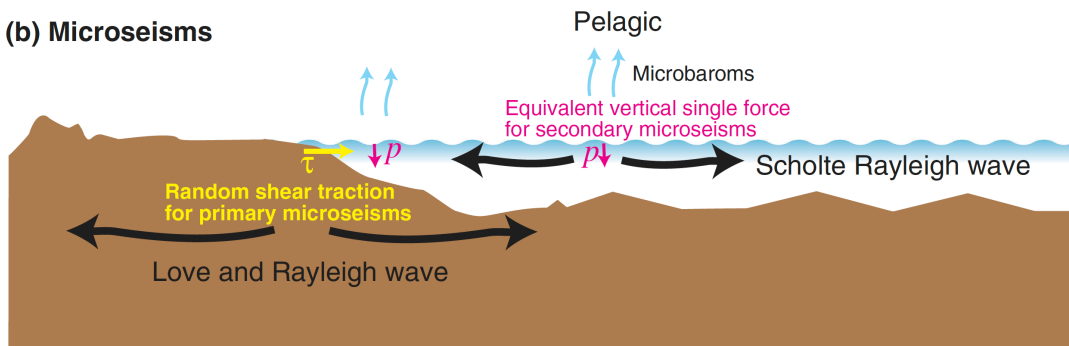


**Figure 3.2:** A schematic view of the excitation of a) seismic hum and b) microseisms (Nishida, 2017).

There are limitations of using the seismic waves which occurred from earthquakes or explosions. These limitations are the high cost of the explosions and the inhomogeneous distribution of seismic stations and earthquakes. The advantage of using seismic noise is that it does not require any demanding source for ground shaking such as earthquakes or explosions.

Most recently, seismic ambient noise tomography has become an alternative method to image the Earth's interior by using direct waves. The noise can be recorded continuously at any location. The cross-correlation of ambient seismic wavefield between two seismic stations gives the Green's functions or impulse response between them (Nishida, 2017) (Figure 3.3). By extracting the Green's functions, it is possible to have an information about the structure between two stations of a station-pair. For a much detailed investigation of such possible structural differences, Green's functions are used to perform a tomographic inversion.

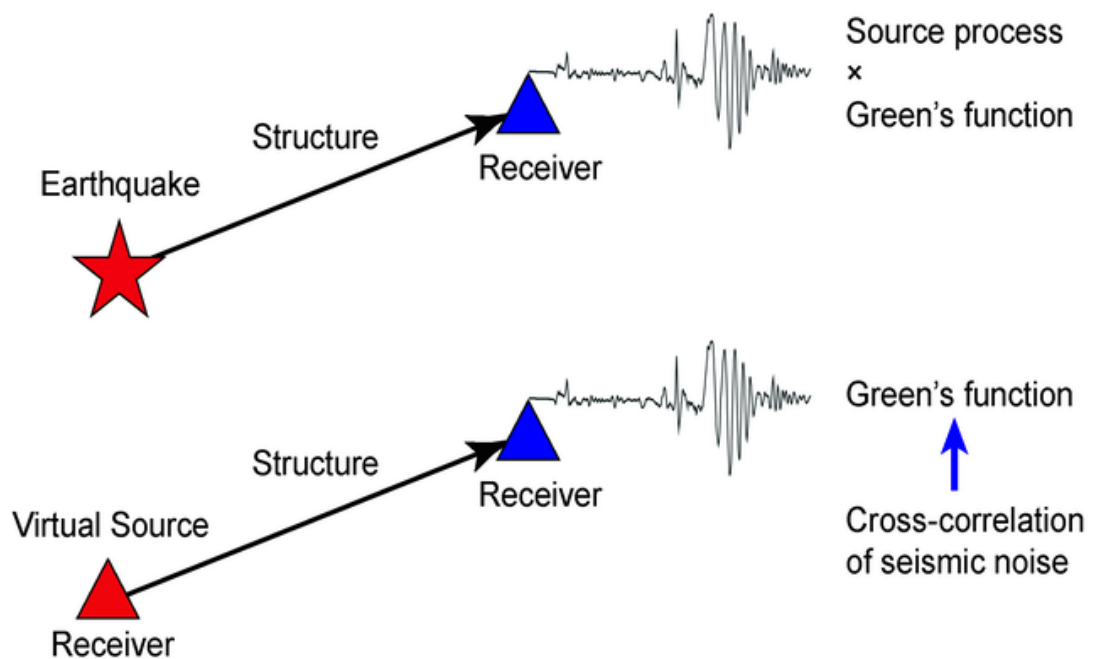


**Figure 3.3:** The difference of the process by using active source and passive source.

The seismic ambient noise was first time successfully performed in Campillo and Paul (2003) Shapiro and Campillo (2004). Examples of the first tomographic imaging that exploit ambient noise-derived dispersion curves are given in Shapiro et al. (2005) (see Fig. 3.5) and Sabra et al. (2005). Following these studies, seismic ambient noise imaging has rapidly become a popular imaging tool of passive seismology experiments conducted at different scales from very shallow to upper mantle depths, in order to

delineate subsurface heterogeneities (e.g. Yang et al., 2007; Mordret et al., 2013; Saygin et al., 2013; Gao and Shen, 2014; Saygin et al., 2015; Kim et al., 2016). For example, Yao et al. (2006), Lin et al. (2008), Moschetti et al. (2010), Saygin and Kennett (2012) and Zulfakriza et al. (2013) are some other well-known examples of ambient noise tomography inversion to map high-resolution crustal heterogeneities. A comprehensive review of the historical background and development of the ambient noise techniques with example studies can be found in Weaver (2005) and Snieder and Larose (2013).

### 3.2 Retrieval of Green's Function

If we consider two receivers  $x_A$  and  $x_B$ , and apply a cross-correlation operation to the observed noise data recorded at two stations, we will be measuring similarities of the waveforms (Figure 3.3). Hence, cross-correlation will yield the same response of the structure beneath them. Lobkis and Weaver (2001) have defined the Green's function by:

$$G(x, x', t) = \sum_n u_n(x)u_n(x')\cos(\omega_n t)H(t) \quad (3.1)$$

where  $H(t)$  is the Heaviside function which is zero for negative time and one for positive time,  $\omega_n$  is angular frequency of mode  $n$ .

The cross-correlation between two stations  $x_A$  and  $x_B$  will be,

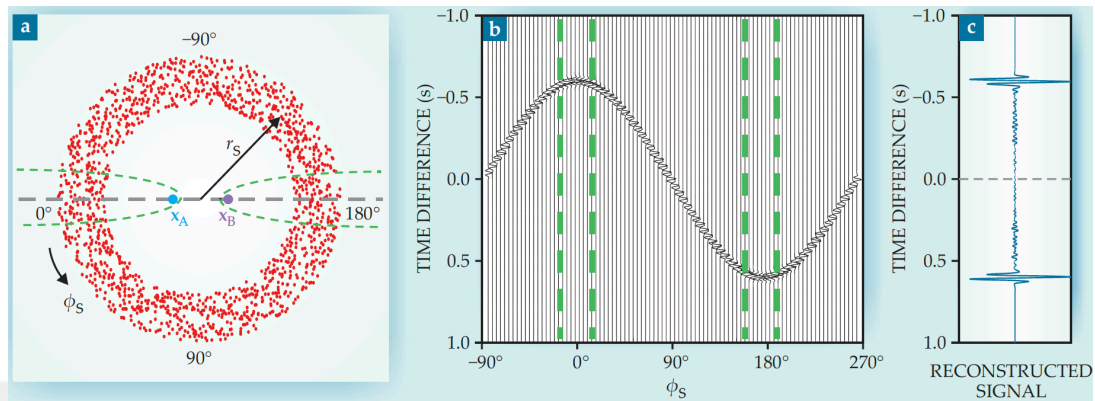
$$C_{AB}(\tau) = S[G(x_A, x_B, \tau) + G(x_A, x_B, -\tau)] \quad (3.2)$$

$C_{AB}(\tau)$  represents the cross-correlation function and  $\tau$  is the lag time.

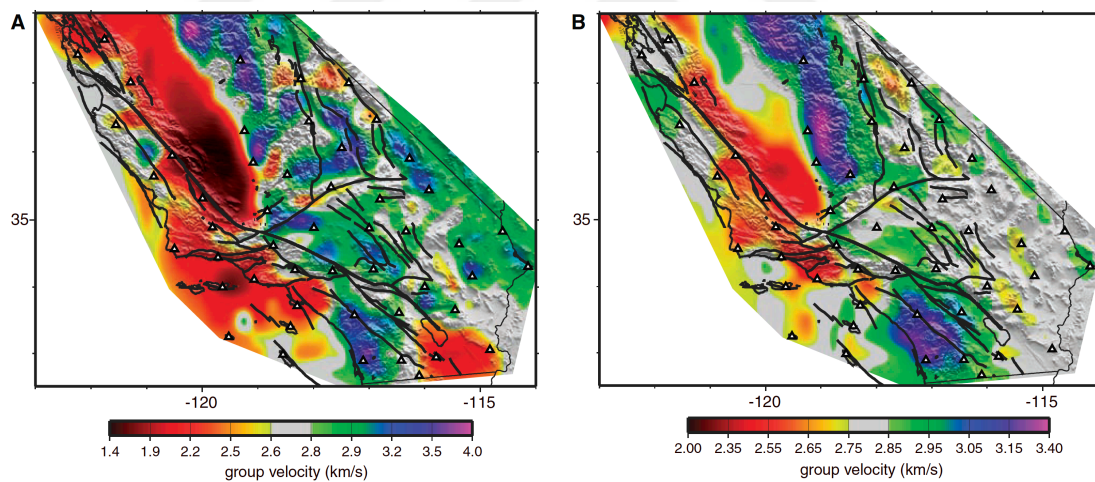
When the noise is distributed evenly, the cross-correlation of  $x_A$  and  $x_B$  gives represents the superposition of Green's functions and  $G(x_A, x_B, \tau)$  and its time-reversed counterpart  $G(x_A, x_B, -\tau)$ .

Figure 3.4 presents a simple and summarized depiction of retrieval of Green's function between two stations  $x_A$  and  $x_B$ . If the noise sources are distributed evenly by sampling the region around station pairs with a good azimuthal coverage (Fig. 3.4a) in the space, then the azimuthal variation of the Green's functions will exhibit correlation time lags with a  $\pi$ -periodicity and varying polarities between negative and positive amplitudes

(Fig. 3.4b). Summing up traces representing noise sources from different azimuths in Fig. 3.4b will only result in the Green's functions corresponding the noise sources located at azimuths inline with the azimuth of the station pair (Fig. 3.4c). This is because the noise sources outside the stationary phase zone cancel each other.



**Figure 3.4:** Retrieval of the Green's function, a) the noise evenly distributed in space (red dots) around the receivers  $x_A$  and  $x_B$ , b) the cross-correlation of the noise for each source, c) the sum of the cross-correlations (Sneider and Wapenaar, 2010).



**Figure 3.5:** Group velocity maps obtained by cross-correlating the one month noise a) Rayleigh waves for period 7.5 sec b) Rayleigh waves for period 15 sec (Shapiro et al., 2005).

### 3.3 Nonlinear Traveltime Tomography

#### 3.3.1 Principle

When a seismic wave propagates inside a medium from a source to a receiver, it will take a certain amount of time to reach the receiver mainly controlled by seismic wave speed properties. Assuming a reference Earth model where the seismic velocities are

known, the traveltimes of different seismic waves can be predicted. However, the observed traveltimes can be generally different from these predicted ones. Observed discrepancies between observed and predicted travel times are known as traveltimes anomalies. The main purpose of seismic tomography experiments is to converge observed traveltimes using an inversion scheme in which initial velocity model repeatedly in a systematic way is updated till reaching an optimum velocity model resulting in traveltimes with the most possible similarity that of observed ones. Such optimization strategy allows resolving a complex unknown velocity models of the subsurface.

The equation (3.1) from Rawlinson et al. (2003) represents the traveltimes of a seismic wave that travels in a medium with a velocity of  $v(x)$ .

$$t = \int_{L(v)} \frac{1}{v(x)} dl \quad (3.3)$$

where  $L$  indicates the raypath.  $v(x)$  the velocity field. The non-linear equation implies the unit path length described within integral equation dependent on unknown velocity field  $v$ .

### 3.3.2 Tomographic inversion

The inverse of the velocity field is called the slowness field, this quantity is used during the tomographic inversion. The subsurface is discretized into cells, each of them having a unique value of slowness (or velocity). Considering many sources and receivers, the data will consist of multiple ray paths with different traveltimes. The model parameter  $\mathbf{m}$  represents the unknown velocity field and while data  $\mathbf{d}$  indicates observed traveltime residuals. The forward calculation of travel time residuals in this problem is given by:

$$\mathbf{d} = \mathbf{G}\mathbf{m} \quad (3.4)$$

$\mathbf{G}$  is known kernel and indicates the relationship between the data and the model for a tomographic problem.

The inverse problem involves the minimization of traveltime residuals that simply indicate the differences between observed data and the response of any given model

introduced to the system. However, because of the nonlinearity of the inverse problem a priori information on the model parameters (e.g. an initial model) and regularization has to be introduced to the inverse problem. Then our objective function  $\phi$  to be minimized takes its following form:

$$\phi(\mathbf{m}) = (\mathbf{d} - \mathbf{G}\mathbf{m})^T(\mathbf{d} - \mathbf{G}\mathbf{m}) + \epsilon(\mathbf{m} - \mathbf{m}_0)^T(\mathbf{m} - \mathbf{m}_0) \quad (3.5)$$

where  $\epsilon$  is the damping parameter that controls the influence of the poorly constrained regions of the model.  $\mathbf{m}_0$  is a reference model. Spatial smoothing is another parameter required to regularize the inversion.

The inversion scheme here can be defined as an iterative workflow of which main steps are listed below (Tarantola, 2005):

- i) parametrization of the model, the model parameters are defined using an initial model at the beginning,
- ii) forward modelling to calculate the responses using the model parameters,
- iii) minimization of objective function to estimate the actual model parameters via the use of observed data.

### 3.4 Transdimensional Bayesian Tomography

#### 3.4.1 Bayesian inference

The model parameters  $\mathbf{m}$  represents the unknown velocity field which is here, the Voronoi nuclei. Being unknown in the problem, posterior distribution has a numerous of maximas (Figure 3.6) (Bodin, 2010).

It includes a highly nonlinear  $\mathbf{G}$  function in Equation 3.4. The posterior probability distribution which is the probability density of the model parameters  $\mathbf{m}$  with the observed data  $\mathbf{d}_{obs}$  written as,  $p(\mathbf{m}|\mathbf{d}_{obs})$  (Smith, 1991). Bayes' rule involves the manipulation of conditional probability which is defined as Bayes' Theorem and written as;

$$p(\mathbf{m}|\mathbf{d}_{obs}) \propto p(\mathbf{d}_{obs}|\mathbf{m})p(\mathbf{m}) \quad (3.6)$$

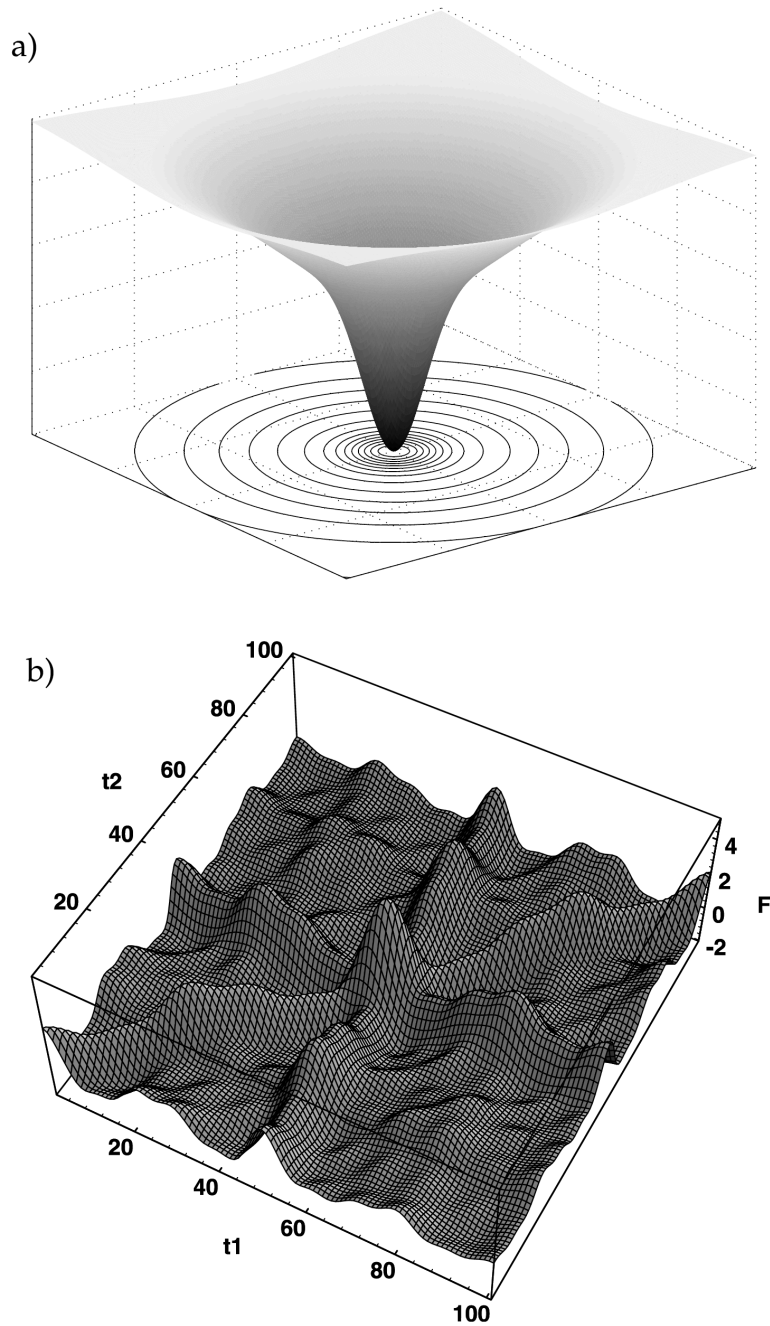


**Figure 3.6:** a) The best fit model which is the only global minimum b) probability density function which has numerous maximums (Sambridge and Mosegaard, 2002).

where the observed data and model parameters are  $\mathbf{d}_{obs}$  and  $\mathbf{m}$  respectively,  $p(\mathbf{d}_{obs}|\mathbf{m})$  is the likelihood function which quantifies the probability of observing the measured data given a model.  $p(\mathbf{m})$  is the a priori probability density of  $\mathbf{m}$ .

The likelihood  $p(\mathbf{d}_{obs}|\mathbf{m})$  has an important role on the estimation of the model parameters for a given data. The aim is to obtain a minimum misfit between estimated data and observed data,

$$\phi(\mathbf{m}) = \left\| \frac{g(\mathbf{m}) - \mathbf{d}_{obs}}{\sigma_d^2} \right\|^2 \quad (3.7)$$

$\phi(\mathbf{m})$  is the misfit,  $g(\mathbf{m})$  is the estimated data, and  $\sigma_d^2$  is the estimated variance. The likelihood as the form of a Gaussian likelihood function:

$$p(\mathbf{d}_{obs}|\mathbf{m}) \propto \exp\left\{-\frac{\phi(\mathbf{m})}{2}\right\} \quad (3.8)$$

Detailed information about the Bayesian inference can be found in Box and Tiao (1973), Tarantola and Valette (1982), Duijndam (1988a), Smith (1991) and Gelman et al. (1995) and Mosegaard and Tarantola (1995).

### 3.4.2 Tomographic inversion

The transdimensional Bayesian tomography is a Bayesian inference approach where many potential solutions are generated. It uses a Markov chain Monte Carlo (McMC) method to estimate the probability distribution of the model parameters. To estimate the posterior density, the model space has to be evaluated at different positions (Bodin and Sambridge, 2009). The McMC method is an iterative stochastic approach which is a solution for the high-dimension of the model space which increase the number of models to test (Bodin and Sambridge, 2009). An extended information about McMC can be found in Gilks et al. (1996) and Sivia (1996).

For each Markov chain, the starting point is randomly selected and the models are generated in terms of the previous model (Bodin and Sambridge, 2009), using the Metropolis–Hasting algorithm (Metropolis et al., 1953; Hastings 1970) which accept or reject new proposed models.

Where the tomographic inversion will give a single best model (Figure 3.6a), the Bayesian inversion gives a probability distribution as the complete solution as it allows evaluating uncertainty on the results.

During the tomographic inversion, the parameters required for regularization of inversion (e.g. mesh size, damping, smoothing parameters, etc.) are chosen by the user on an arbitrary basis. Such parameters are tested by the geophysicist until the final inversion result reaches a satisfactory level. The transdimensional Bayesian tomography developed by Bodin et al. (2012) invert simultaneously for the number of

cells in the model, their geometries and their seismic velocities. It can treat the noise as unknown. Then the parametrization is directly determined by the inversion. The velocity field is represented with irregular Voronoi cells (Figure 3.7), which vary in size and shape depending on data resolution conditions in the model space and reflect the resolution in the model due to the irregular distribution of the station (Sambridge et al., 2013).

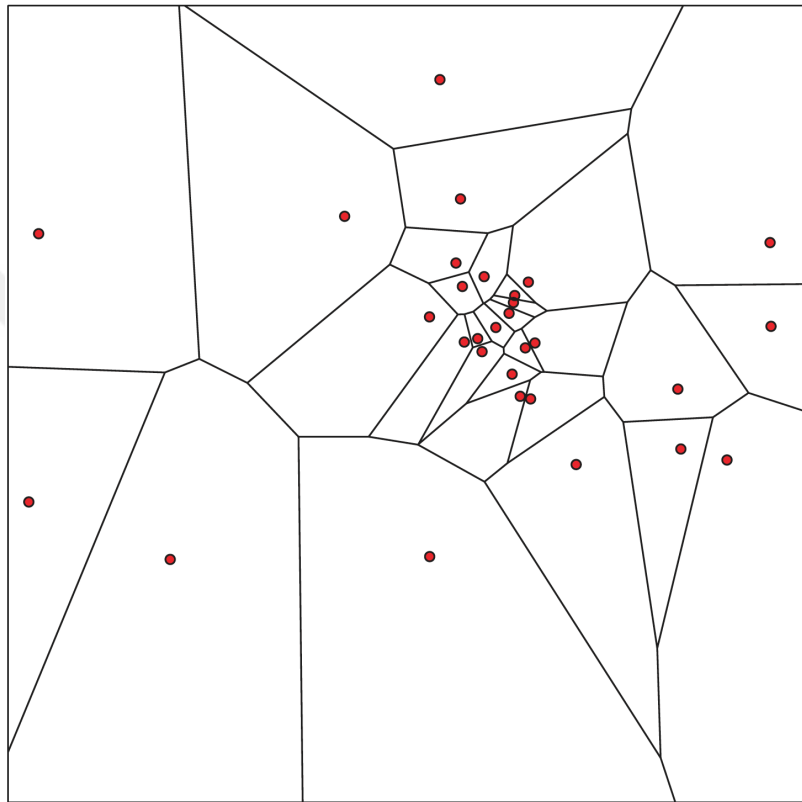


**Figure 3.7:** An example of a Voronoi cells which are in irregular shape shown in black lines and nodes shown in red dots (Bodin et al., 2012).

In order to avoid unrealistic Earth models, the inversion considers prior information on the parameters, such as the range of seismic velocity expected, the range on the number of cells or the range on the noise that might be considered.

For the forward modelling, the Fast Marching Method (FMM, Rawlinson and Sambridge, 2004a, b) is used to update the raypaths. In Figure 3.8, the tomographic scheme is shown. The ray geometries are updated at each iteration by using FMM. For the inversion step, reversible jump Markov chain Monte Carlo (rj-McMC) algorithm (Green 1995) is used to determine the partitioned velocity models (inside the inner loop shown in Figure 3.8) that forms the reference model for the next iteration (Bodin and Sambridge, 2009).

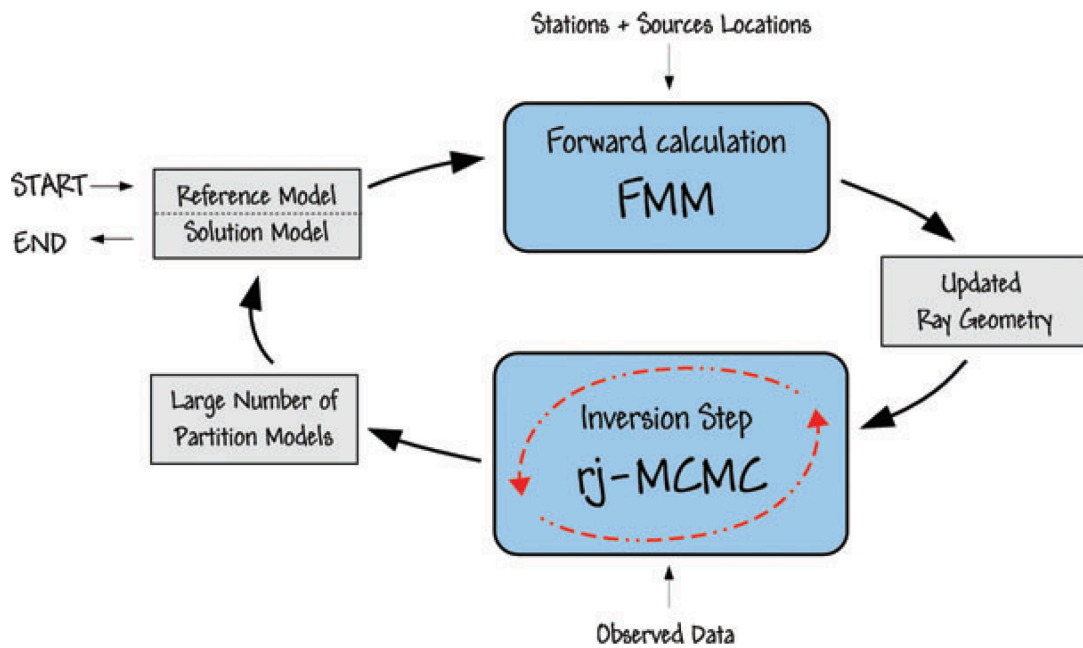


**Figure 3.8:** The steps of tomographic inversion used in this study (Bodin and Sambridge, 2009). Two loops are shown; the black lines show the outer loop and the dashed red lines show the inner loop.

In this thesis, our main aim is to conduct the transdimensional Bayesian tomography inversion adapting the rj-McMC algorithm (e.g. Bodin et al., 2012) to the traveltime residuals extracted from the cross-correlated ambient noise data along the northwest of NAFZ and surrounding regions. In addition to the Bayesian approach, the non-linear tomographic inversion, for comparison was also applied to the same dataset.



## **4. DATA**

### **4.1 Data Sources**

In order to obtain a high-resolution crustal structure image of the north-western part of the NAFZ including the Sea of Marmara, we use continuous recordings of 112 temporary and 84 permanent broadband and short-period seismic stations operated in the region. The data were obtained from the IRIS and AFAD repositories. The Dense Array for North Anatolia (DANA) seismic network was operating for 18 months between May 2012 and October 2013 with a dense coverage, inter-station spacing of 7 km. The DANA network consists of 70 temporary broadband seismic stations and additionally 3 permanent Kandilli seismic stations. In order to increase the station coverage, the permanent Kandilli (73 seismic stations) and the AFAD (31 seismic stations) networks and other 42 temporary seismic stations which have been operating at various time periods between 2005 and 2017 were used. In Figure 4.1, the locations of seismic stations that are used in this study are shown. Blue triangles indicate the AFAD network, red triangles represent the Kandilli network and orange triangles show all temporary seismic stations recording in the region.

The typical inter-station spacing varies between 10 km and 400 km. The sampling rates of the recordings range from 20-50 Hz. The data were downsampled to 10 Hz to obtain a unique sampling rate and a zero-phase low pass filter was applied to each seismic record prior to downsampling. The recordings from various types of sensors were used to calculate cross-correlations. However, we did not apply systematic instrument corrections to all records in order to unify the sensor responses because our tests showed that using different instrument responses had no effect on the resultant correlation functions within the bandwidth of frequency (Figure 4.2).

### **4.2 Data Processing**

Following the downsampling process, we benefit from the following recipe described in Saygin and Kennett (2010) and Saygin and Kennett (2012) to obtain Green's

## NW Turkey Seismic Station Distribution Map

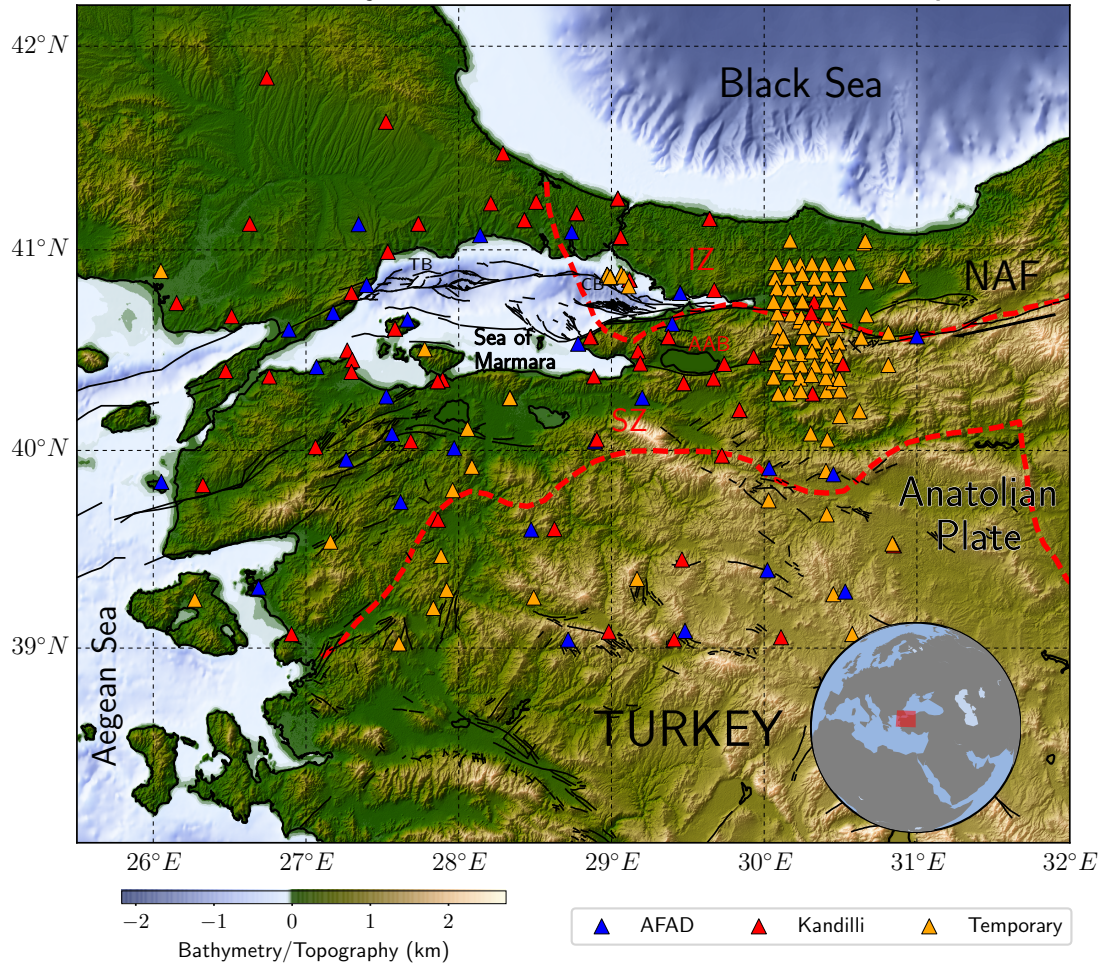


**Figure 4.1:** Locations of the seismic stations used in this study. The background digital elevation model is from ASTER2 (Geyer, 2015), and the bathymetric data is from GEBCO, provided by GEBCO (1997). Red dashed lines represent the suture zones. AAB: Armutlu-Almacık Zone, CB: Çınarcık Basin, IZ: Istanbul Zone, NAF: North Anatolian Fault, SZ: Sakarya Zone, TB: Tekirdağ Basin

functions using seismic noise cross-correlations among vertical components of seismic stations:

1. Preparation of daily SAC files observed for every receivers.
2. Eliminate the problematic records related instrumental problems.
3. Dividing 4 hours of segments from full day records into, and generating cross-correlations via a 1-hour overlap at each station pair.
4. Daily estimates are obtained by averaging the cross-correlation segments.
5. Enhancement of the signal to noise ratio of the final Green's functions by stacking all averaged correlations for each days

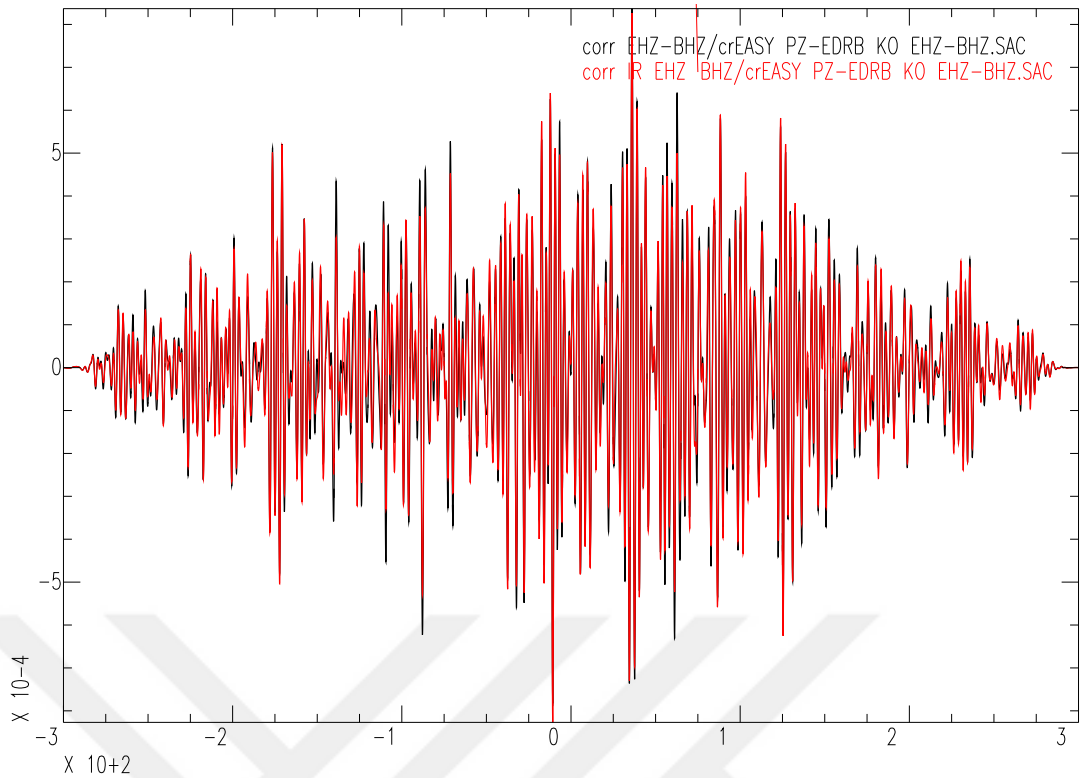


**Figure 4.2:** Instrument response test applied to the cross-correlation between the stations EASY and EDRB.

6. The cross-correlation is computed for data with a length of 300 seconds and adjacent streams have an overlap of 60 seconds.

Once the construction of cross-correlation traces is completed, all the available traces are stacked to create the final inter-station correlogram. Figure 4.3 shows an example of obtained cross-correlation between the stations TVSB and ADVT. In total, 24310 cross-correlations were obtained and visual identification was made manually for every cross-correlation to avoid picking noise or higher mode energy. In Figure 4.4, data traces of cross-correlations extracted for four examples are shown. The visual identification was made by comparing at the cross-correlations between one station and others.

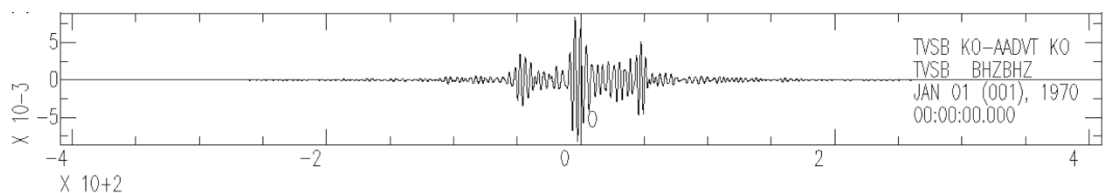


**Figure 4.3:** An example of cross-correlation between TVSB and ADVT stations. Approximately at -50 sec and 50 sec, the two-sided Green's function of the Rayleigh wave is observable.

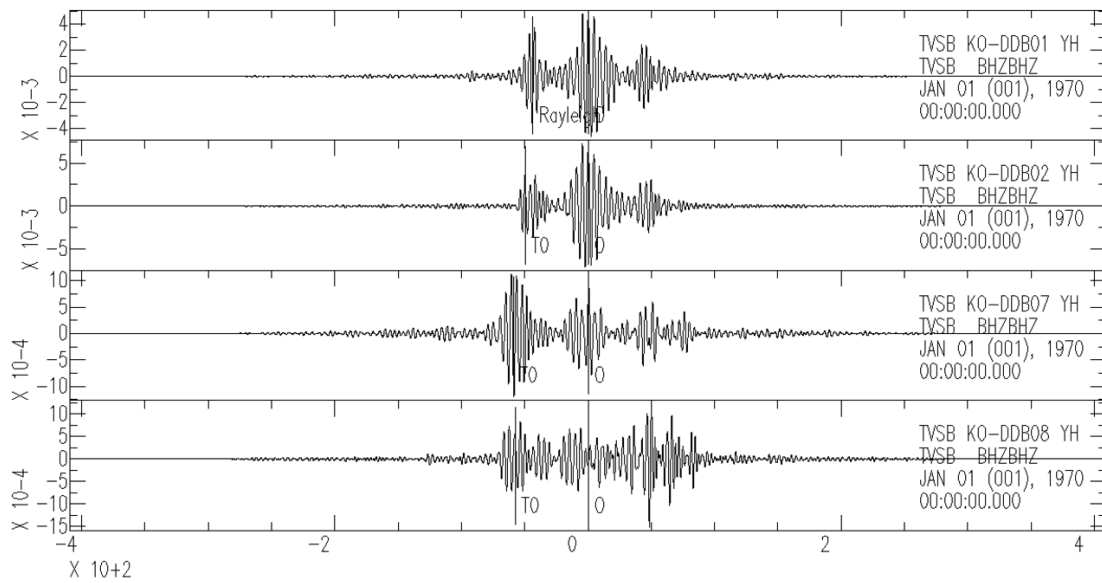


**Figure 4.4:** Four examples of cross correlations between stations TVSB and DB01, DB02, DB07, DB08.

Two examples of estimated Rayleigh wave Green's function as a function of a distance between one station and all the others from ambient seismic noise is shown in Figure 4.5. In Figure 4.5a, station TVSB (Tavsanlı) in the southern part of the study area and in Figure 4.5b, station KLYT (Kilyos) in the northern part of the study area is presented. An increase in the arrival time with the interstation distance and the two-sided Green's function of the Rayleigh wave is observable in Figure 4.5. All the waveforms were filtered between 0.1 Hz and 1.0 Hz and normalized to unity. We applied a gain function to cross-correlations in Figure 4.5 to suppress the waves between -10 and 10 seconds. A narrow-band Gaussian filter was applied to every Green's functions to extract the group velocities from the arrival times by using multiple filter analysis. This technique is used to estimate group velocities through the cross-correlation of recorded noise.

We use a period range from 1 second (1 Hz) to 20 seconds (0.05 Hz). For periods more than 20 seconds, the extracted Green's functions do not carry upward information about the structure of the study area most likely due to the poor raypath coverage. A maximum over 6000 interstation traveltimes were acquired by manual picking at each period. An example of extracting group velocities from the arrival times by using multiple filter analysis technique is shown in Figure 4.6. In Figure 4.7, the number of filtered and picked Green's functions for each period is shown.

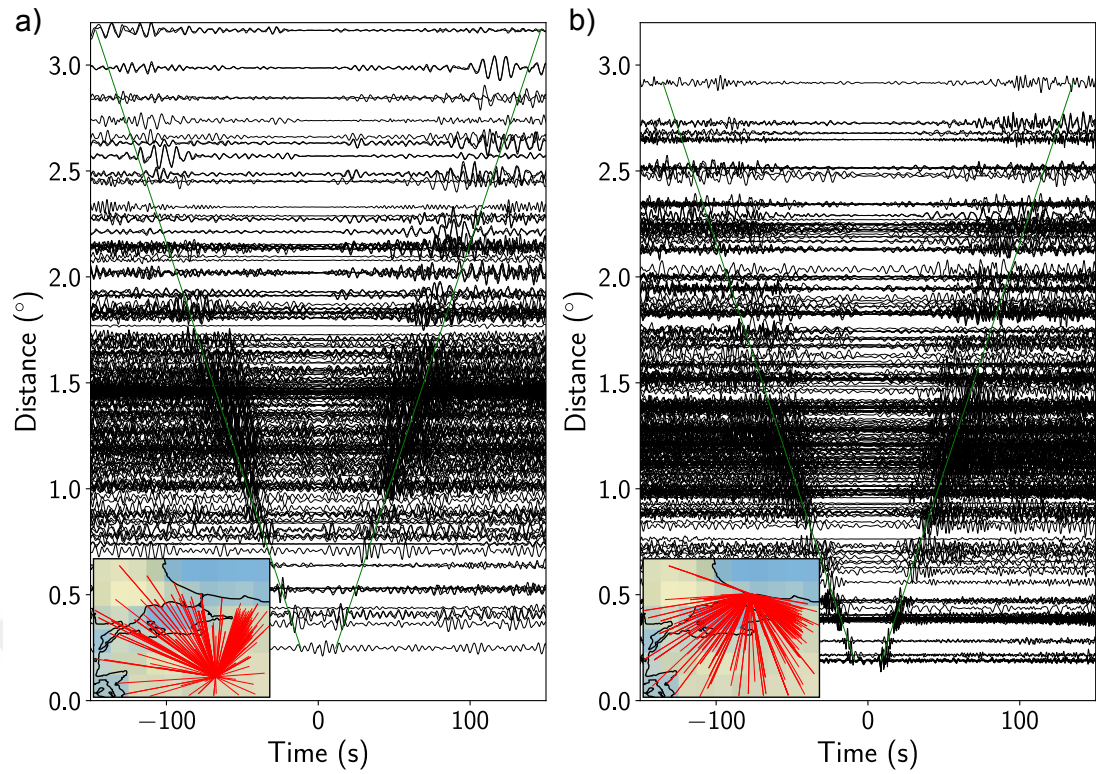


**Figure 4.5:** Extracted Green's functions between all the available stations and a)TVSB, b)KLYT stations. Green lines correspond to 2.4 km/s group velocity.

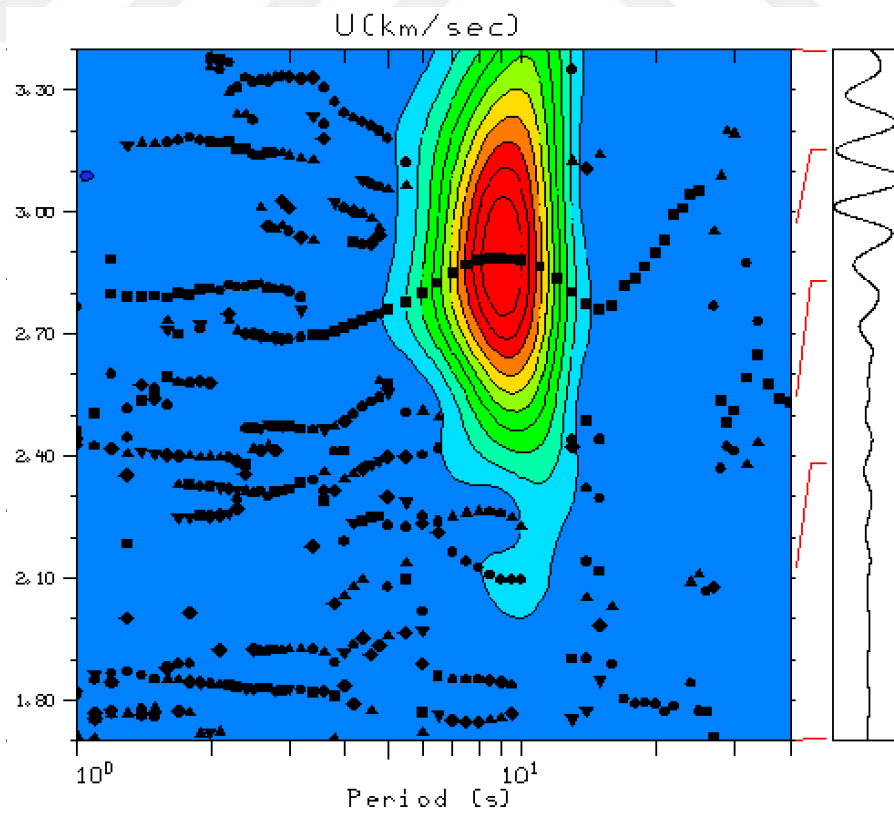


**Figure 4.6:** An example of the filtering process shows the group velocities in respect to period.

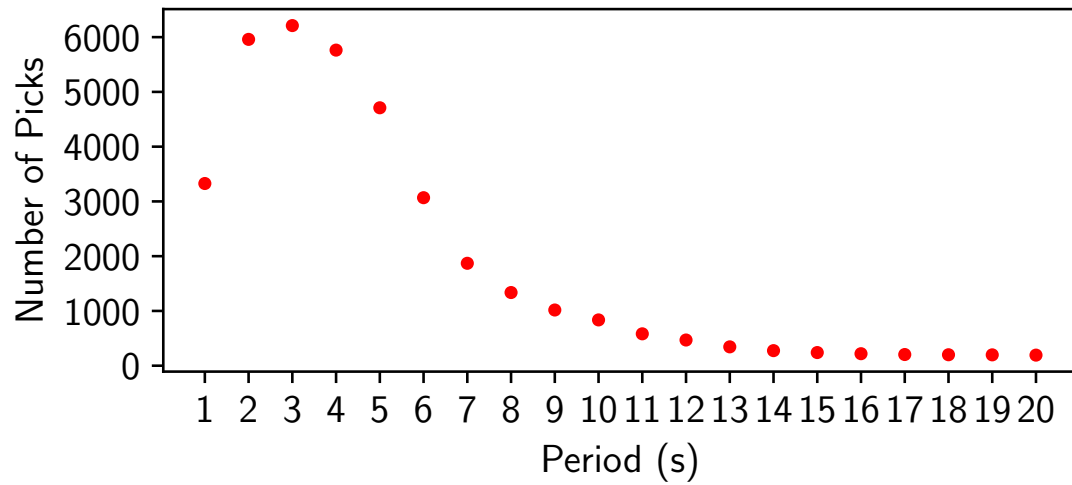


**Figure 4.7:** Number of picks for every period between 1 and 20 s. The maximum number of picks is over 6000 for period 3 s.

## 5. APPLICATION OF THE INVERSION TO DATA

### 5.1 Tomographic Inversion

A fully nonlinear 2-D tomographic inversion was performed to resolve seismic velocity maps for periods ranging between 1 and 20 s. We used a 50 x 50 (roughly corresponding 10 km x 20 km) grid spacing and assumed a reference velocity of 2.4 km/s for the inversion at each period. The observed travel time residuals were inverted using the Fast Marching Method (FMM, Rawlinson and Sambridge, 2004a,b) forward traveltimes calculations and subspace inversion. We performed several inversion tests by experimenting different sets of damping and smoothing values. Figure 5.1 shows that the variation of these two parameters did not produce big differences in the inversion results. Thus, we fixed the final value of damping to 500.5 and of the smoothing to 500.5.

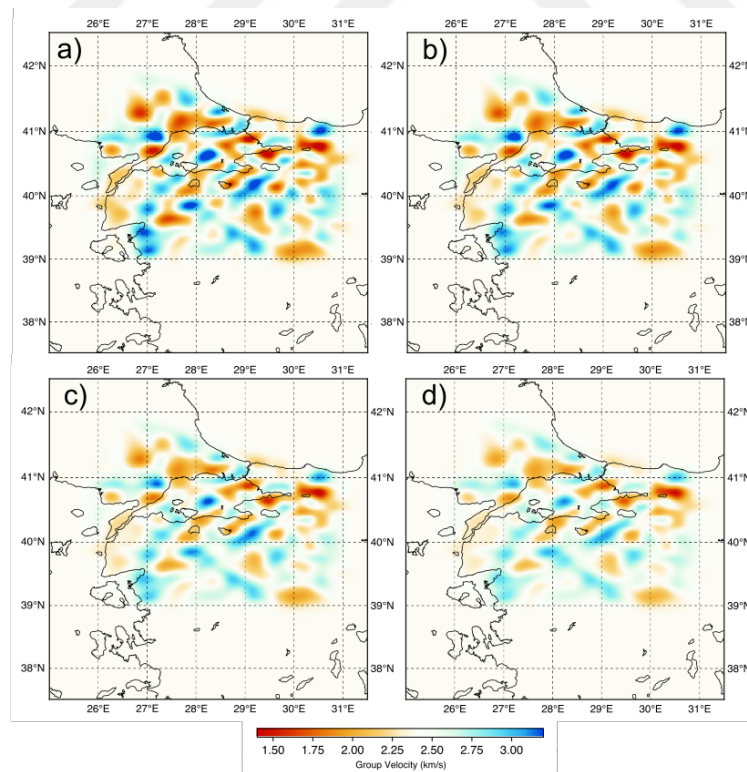


**Figure 5.1:** Effects of the smoothing and damping parameters on the inversion results. The damping  $\epsilon$  and smoothing  $\eta$  parameters are; a)  $\epsilon=10.5$   $\eta=10.5$ , b)  $\epsilon=100.5$   $\eta=100.5$ , c)  $\epsilon=500.5$   $\eta=500.5$ , d)  $\epsilon=1000.5$   $\eta=1000.5$

The ray paths were calculated by applying the fully nonlinear inversion with 6 iterations. In Figure 5.2, the new effective ray path coverage for the 3 sec period which corresponds to the maximum interstation traveltimes is shown.

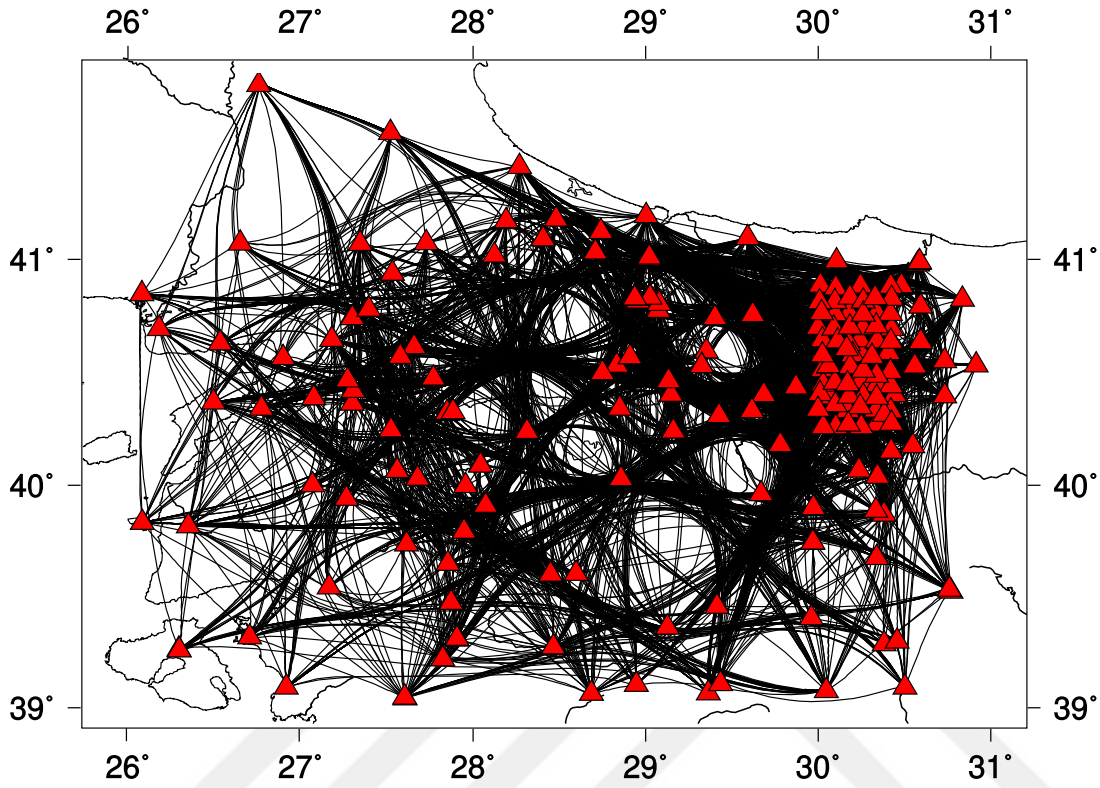


**Figure 5.2:** The map of raypath coverage of the study area for period 3 sec after applying the fully nonlinear inversion. Red triangles represent the seismic stations that are used in this study.

## 5.2 Transdimensional Bayesian Tomography

We performed a fully non-linear inversion using a Bayesian framework. As already mentioned in Chapter 3 the advantage of this framework compared to standard tomography is that it allows obtaining an ensemble of solutions with a full probability distribution. This posterior probability distribution contains a large ensemble of models that satisfy the data, allowing a statistical assessment of the model uncertainty. The method uses the reversible jump Markov chain Monte Carlo method in the sampling process implemented by Bodin et al. (2012). In this method, in addition to the velocity field, the number and position of cells, and the data noise are all part of unknowns.

In this work, we used a prior distribution for the group velocity range for the number of Voronoi cells between 1.0 and 3.2 km/s and between 2 and 1000 cells, respectively.

The *raj*-McMC was run with using 200 parallel Markov chains on supercomputing cluster. Each chain was run on a single core and did 200000 iterations in total where 100000 burn-in steps and 100000 post burn-in steps at each period. In the first iteration, the ray paths were assumed as to be straight lines. Then between each run of inversion the raypaths were updated with the new velocity model using FMM. Five iterations were achieved to update the raypath geometries at each period. The velocity models at each iteration for period 3 sec is shown in Figure 5.3.

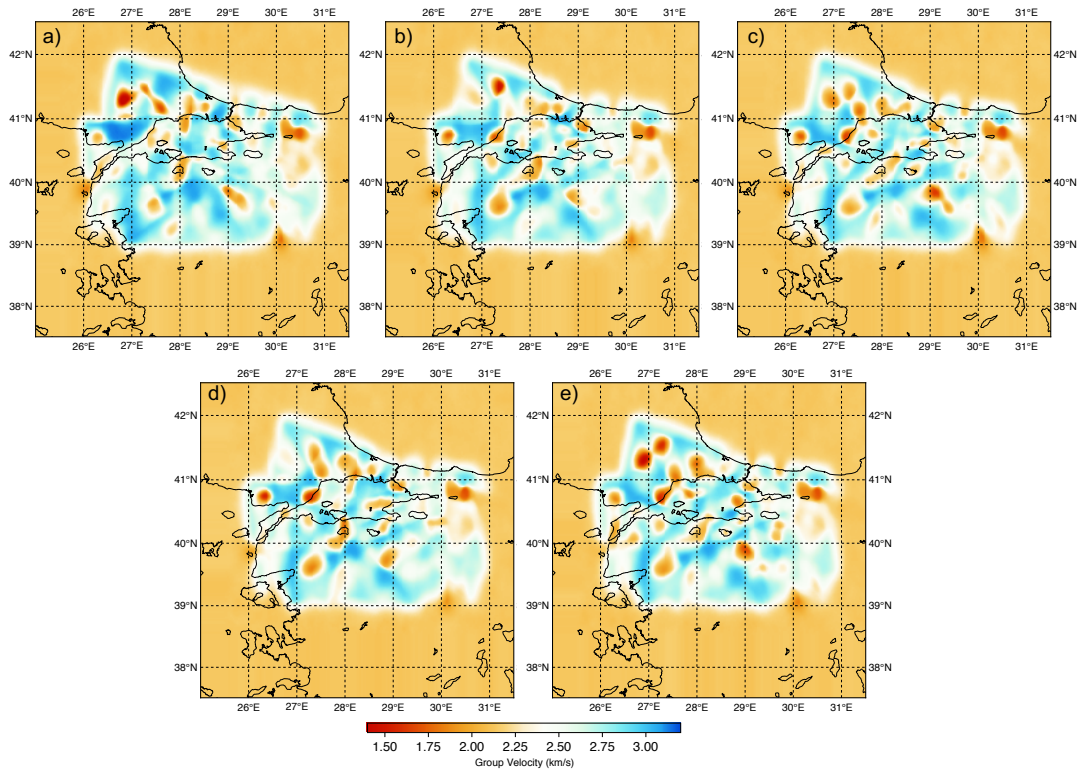


**Figure 5.3:** Group velocity models for each iteration for period of 3 sec. a)First iteration, b)Second iteration, c)Third iteration, d)Fourth iteration, e)Fifth iteration.



## 6. RESULTS AND INTERPRETATIONS

The main motivation of the current thesis is to adapt a transdimensional Bayesian inversion approach using Green's functions which were retrieved along the northwest NAFZ. Prior to this using exactly the same dataset, we tested rather simple nonlinear tomography method that has been conventionally employed in various early ambient noise tomography experiments. Despite the fact that, inversion algorithms employed here are based on different frameworks with different strategies when resolving unknown parameters in model space, lateral variations of group velocities with similar types of features over the study area have strongly evidenced the tomographic images might be required by data. Our choice for preferring Bayesian inversion approach in this work is that, it does not depend on any user chosen parameters that are necessary during the regularization of the objective function. Such parameters namely, damping and smoothing parameters can introduce strong artefacts into the solution. However, we have shown that possible influence of the various implementation of these parameters should be very small (e.g. no drastic change in tomographic images) when a nonlinear tomography approach was applied (Fig. 5.1) for the study area. In this study, we have shown that the Bayesian approach would not need any fixed spatial model parametrization but instead, it achieves parametrization in lateral and vertical directions in an adaptive manner by considering actual data resolution. Overall the advantage of the Bayesian framework can be summarized by; i) adaptive with the irregular Voronoi cells vary in size and shape depending on data resolution conditions in the model space, ii) independent from the damping and smoothing parameters, iii) it gives a probability distribution as a complete solution as it allows to evaluate uncertainty on the results, not a single best model like the tomographic inversion.

In this chapter, we will start by describing characteristic features that we obtained from two types of inversions. Group velocities shown here in general at longer periods must be associated with relatively deep structures and vice versa.

In Figure 6.1, the nonlinear tomography images from periods 1 sec to 20 sec are presented. From nonlinear direct tomography images, it is evident that the group velocities of the Rayleigh waves vary with a range between 1.4 km/s and 3.4 km/s. At

all periods, the velocity anomalies demonstrate spatial variation of relatively high and low velocity anomalies. For higher frequencies (shorter periods), the path coverage tends to be good and the estimated group velocities vary between 1.6 km/s and 3.2 km/s.

Lateral variations of group velocities resolved from the transdimensional Bayesian inversion are presented in Figure 6.2 for the same periods between 1 sec and 20 s. Reliability of group velocities can be tested corresponding uncertainty maps displayed in Figure 6.3. For group velocity maps at periods smaller than 10 s, the region of small uncertainties (e.g.  $<0.2$  km/s) corresponding high-resolution model results appear to expand a broader space compared to those higher than 10 s. Notably high uncertainty ( $\sim 0.4$  km/s) area roughly between 27E-28E and 41N-42N is present for almost all periods and stems from the lack of crossing ray-paths in this region.

As a significant tectonic feature within our study, the NAFZ and its segments are well marked by low group velocity distribution as this implies zones of highly deformed and distributed crustal features along major fault zones in continents. Similar type of pattern along the NAFZ have been earlier imaged by full-waveform modelling studies (e.g. Fichtner et al., 2013a,b; Çubuk-Sabuncu et al., 2017) and in the ambient noise tomography study conducted in a much regional scale covering entire Anatolia by Delph et al. (2015) although resolution power is stronger in our study. In the western US, along the San Andreas Fault Zone, which is another typical active continental fault zone that has been the focus of extensive scientific attention owing to its seismic hazard potential Shapiro et al. (2005) were able to detect lower speeds are observed in the Mojave Shear Zone and along the Garlock Fault.

There is an apparent continuity of low group velocity variation along the east-west oriented segmentation along the NAFZ for various frequencies, in particular between 1 to 10 s. However, for an actual knowledge on its depth extent, we further suggest S-velocity inversion which can potentially tell us whether the shear deformation remains in narrow localized zones in relation to the brittle deformation in the upper crust or becomes widening to the lower crustal depths due to ductile flow.

Generally speaking a lateral variation of group velocities for a frequency range between 1 to 10 s, which most likely provides much reliable data resolution and hence model resolution indicates some prominent characterized very low absolute group

velocities. Tekirdağ Basin to the west of our model is characterized by one of those low-velocity regions falling between 27.5E-28.0E and 40.5N-41N. Signatures of Tekirdağ Basin in early studies (e.g. Delph et al., 2015; Çubuk-Sabuncu et al., 2017) were implied but with low-resolution capability compared to this study. Here provide valuable constraints on the structure of Tekirdağ Basin. Another notable low-velocity area is located at the eastern side of the Sea of Marmara expanding over an area between 28.75E-29.25E and 40.7N-40.9N. From local geological constraints of the Sea of Marmara, we know that significant low-velocity variation here might be associated with Çınarcık Basin. Apparent higher absolute group velocities in between Tekirdağ Basin and Çınarcık Basin for periods 1 to 10 s could stem from the Central and Western Highs that have been previously reported with high-velocity P-wave velocity Bayrakçı et al. (2013) and high resistivity anomalies that is attributed to asperity zones in the Sea of Marmara by Kaya (2012).

At the easternmost part, where we expect highest data resolution, the NAFZ crosses different geological zones. Istanbul zone consists of Precambrian crystalline overlaid by a continuous sedimentary sequence (Okay et al. 1999). Relatively high-velocity anomalies at upper crustal depth-resolved in a very recent teleseismic P- and S-wave tomography study by Papaleo et al. (2017, 2018) confirmed the dominant effect of Precambrian crystalline rocks. Similarly, coda waves analyses of local earthquakes specifically in this region exhibit low attenuation both for inelastic absorption and scattering attenuation in the region (e.g. Izgi et al., 2018) as being in a good accordance with significant high group velocities resolved following both Bayesian and nonlinear inversions in this study. In this part of the study region, Kahraman et al. (2015) have modelled the crustal structure of the region via inversions of P-receiver functions observed a high velocity and low-velocity zones beneath Istanbul Zone and Armutlu-Almacik Block, respectively. Our group velocity maps indicated visible low velocity confirming the Almacik Block with a low uncertainty estimates (ranging 0.0-0.1) of model parameters. Such coherency with P-receiver function models (Kahraman et al., 2013) and teleseismic tomography inversion results (Papaleo et al., 2018) suggest the reliability of our maps although three different method compared here pose different sensitivities to the same structures due to their changing frequency contents.

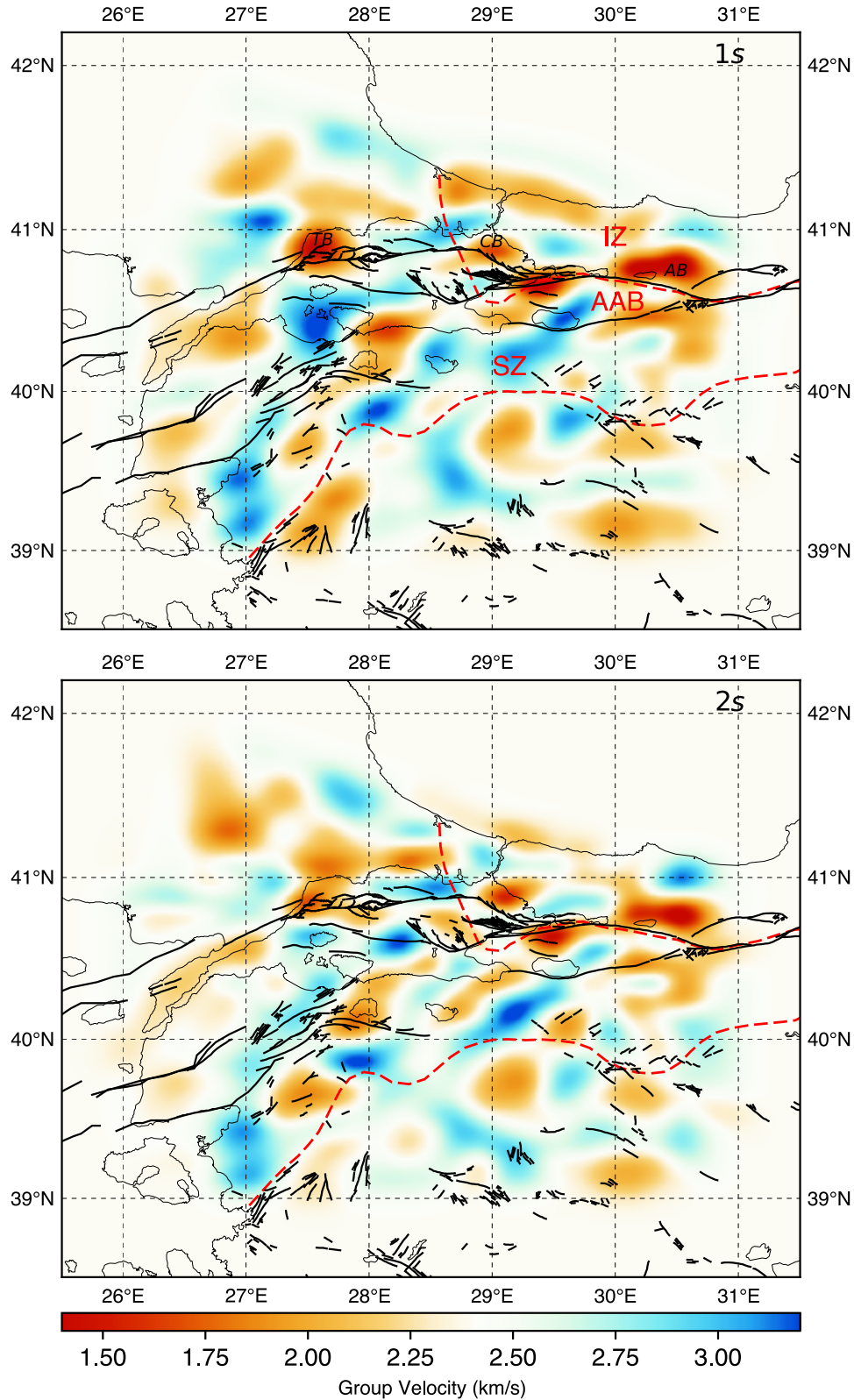


**Figure 6.1:** Group velocity images obtained from nonlinear tomography for periods between 1 sec and 20 sec. The group velocity ranges between 1.4 km/s and 3.2 km/s. Black lines represent the NAFZ, dashed red lines represent the suture zones. AAB: Armutlu-Almacik Block, AB: Adapazari Basin, CB: Cinarcik Basin, IZ: Istanbul Zone, SZ: Sakarya Zone, TB: Tekirdag Basin.

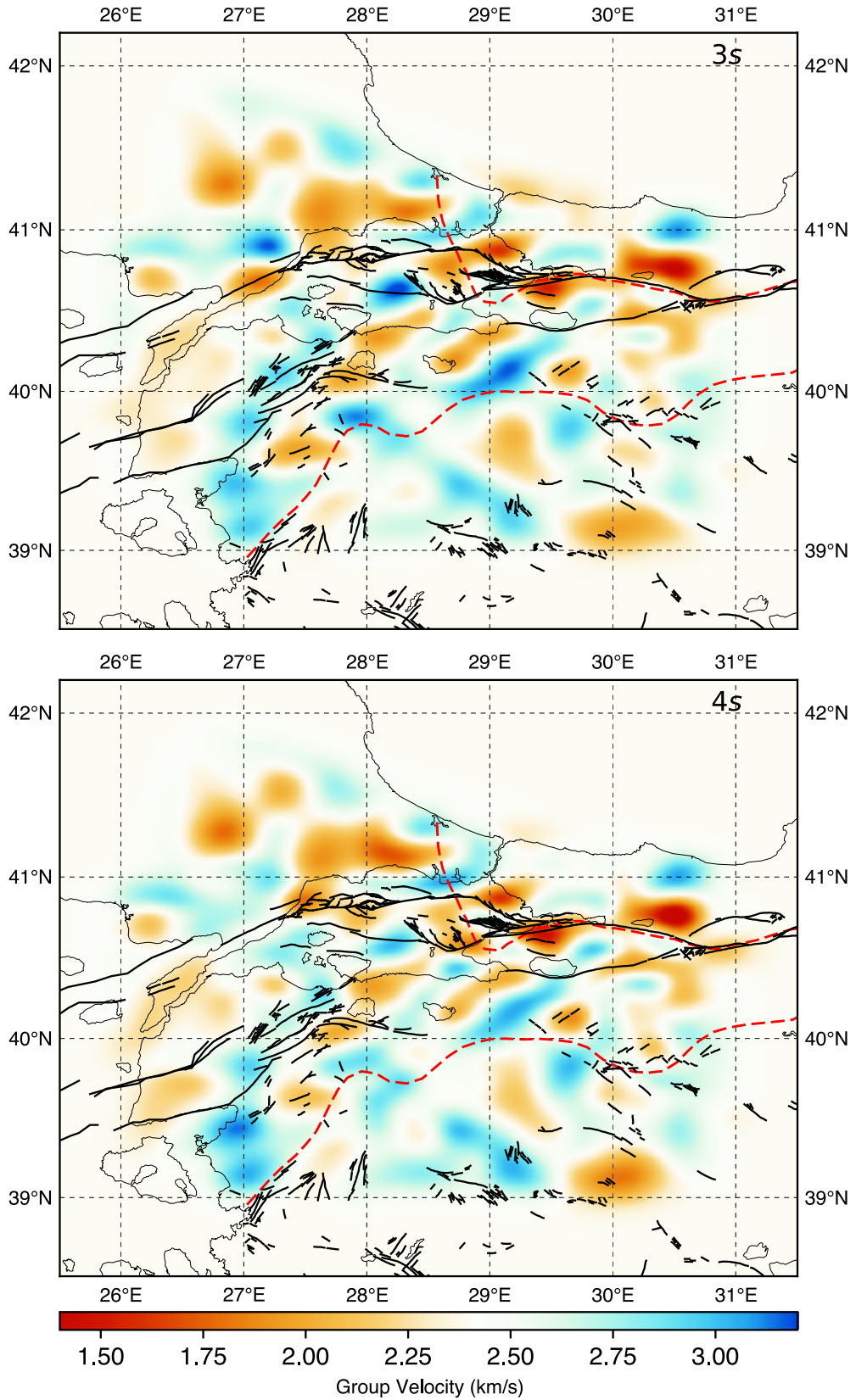


**Figure 6.1 (continued):** Group velocity images obtained from nonlinear tomography for periods between 1 sec and 20 sec. The group velocity ranges between 1.4 km/s and 3.2 km/s. Black lines represent the NAFZ, dashed red lines represent the suture zones.

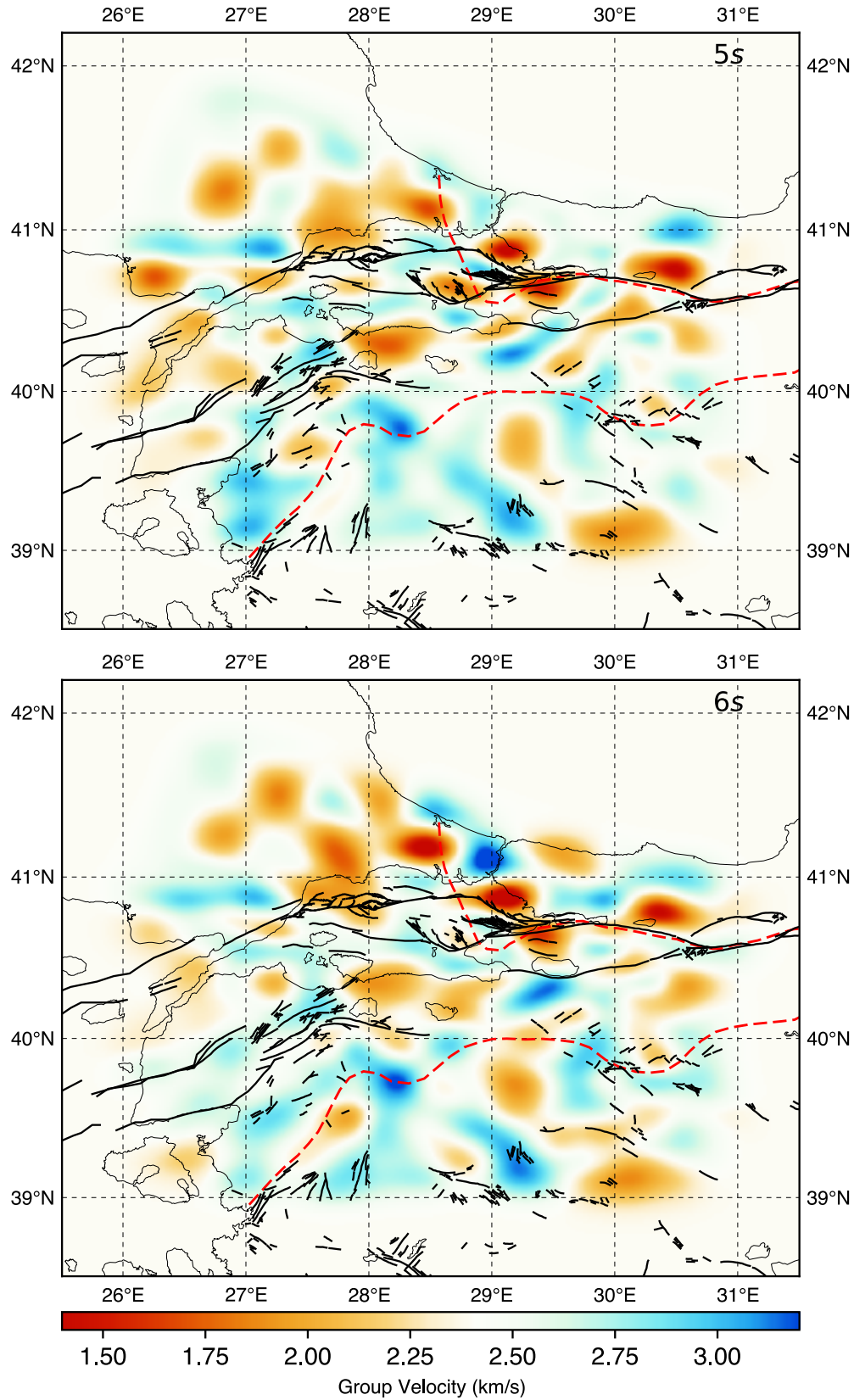


**Figure 6.1 (continued):** Group velocity images obtained from nonlinear tomography for periods between 1 sec and 20 sec. The group velocity ranges between 1.4 km/s and 3.2 km/s. Black lines represent the NAFZ, dashed red lines represent the suture zones.

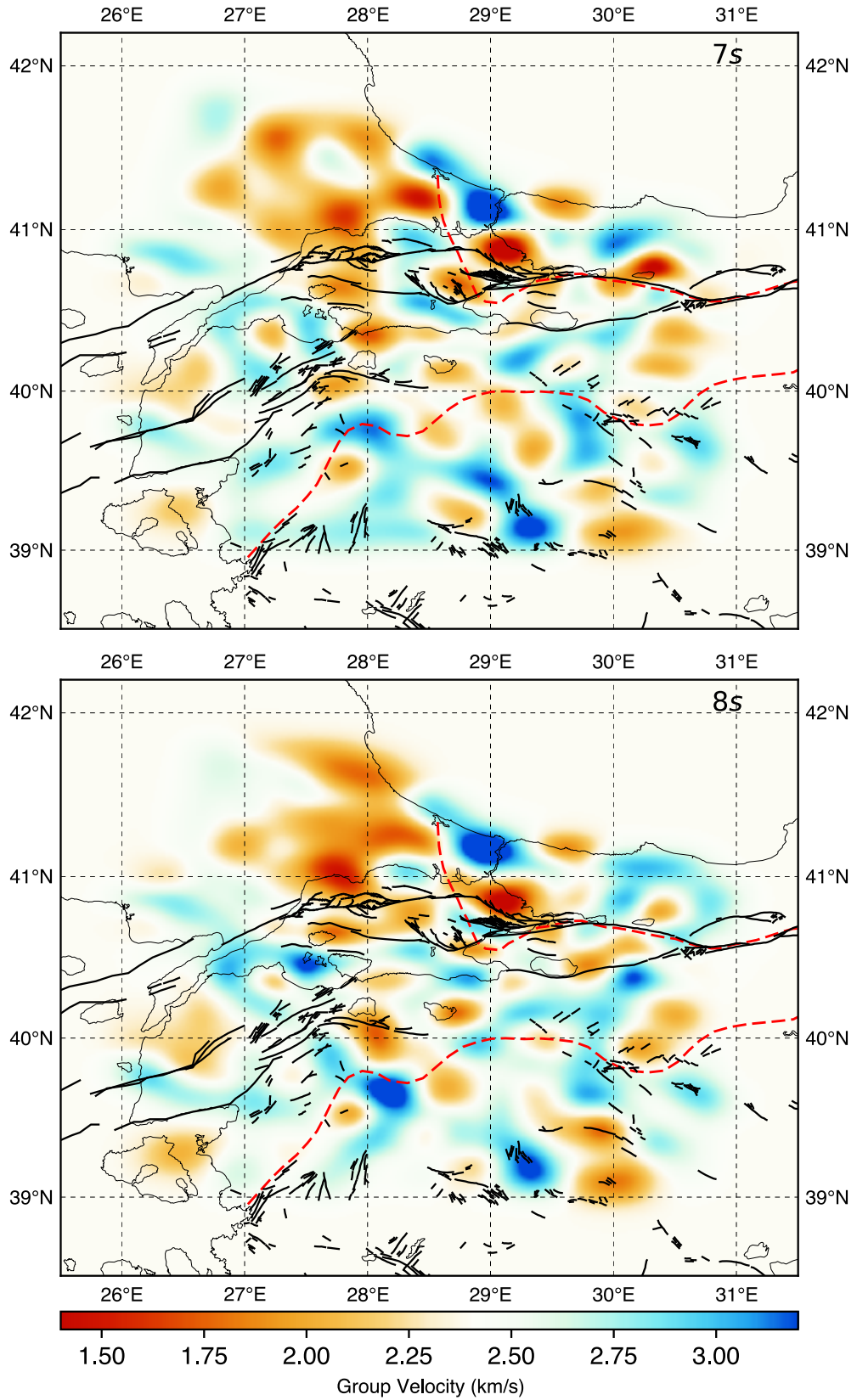


**Figure 6.1 (continued):** Group velocity images obtained from nonlinear tomography for periods between 1 sec and 20 sec. The group velocity ranges between 1.4 km/s and 3.2 km/s. Black lines represent the NAFZ, dashed red lines represent the suture zones.

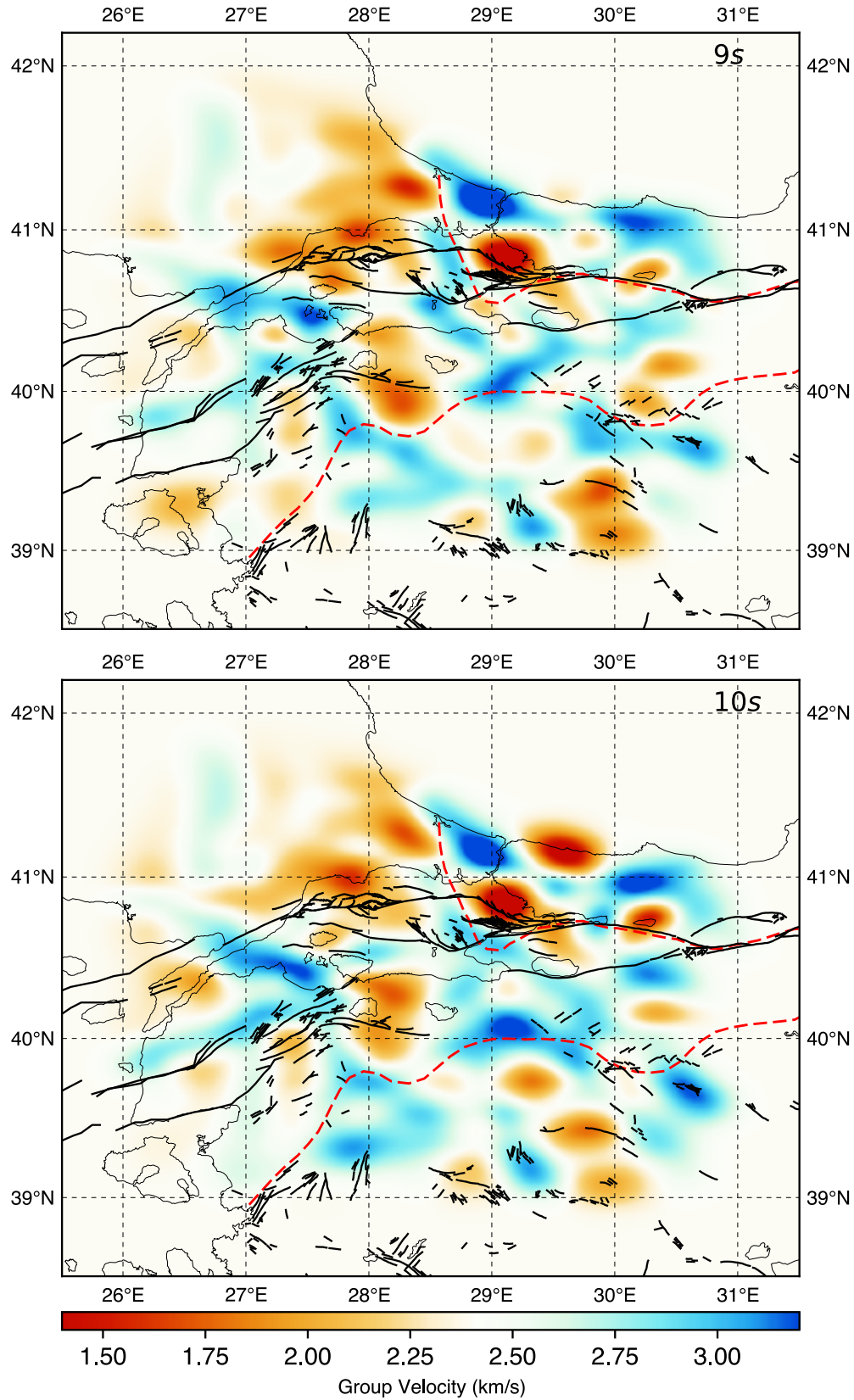


**Figure 6.1 (continued):** Group velocity images obtained from nonlinear tomography for periods between 1 sec and 20 sec. The group velocity ranges between 1.4 km/s and 3.2 km/s. Black lines represent the NAFZ, dashed red lines represent the suture zones.

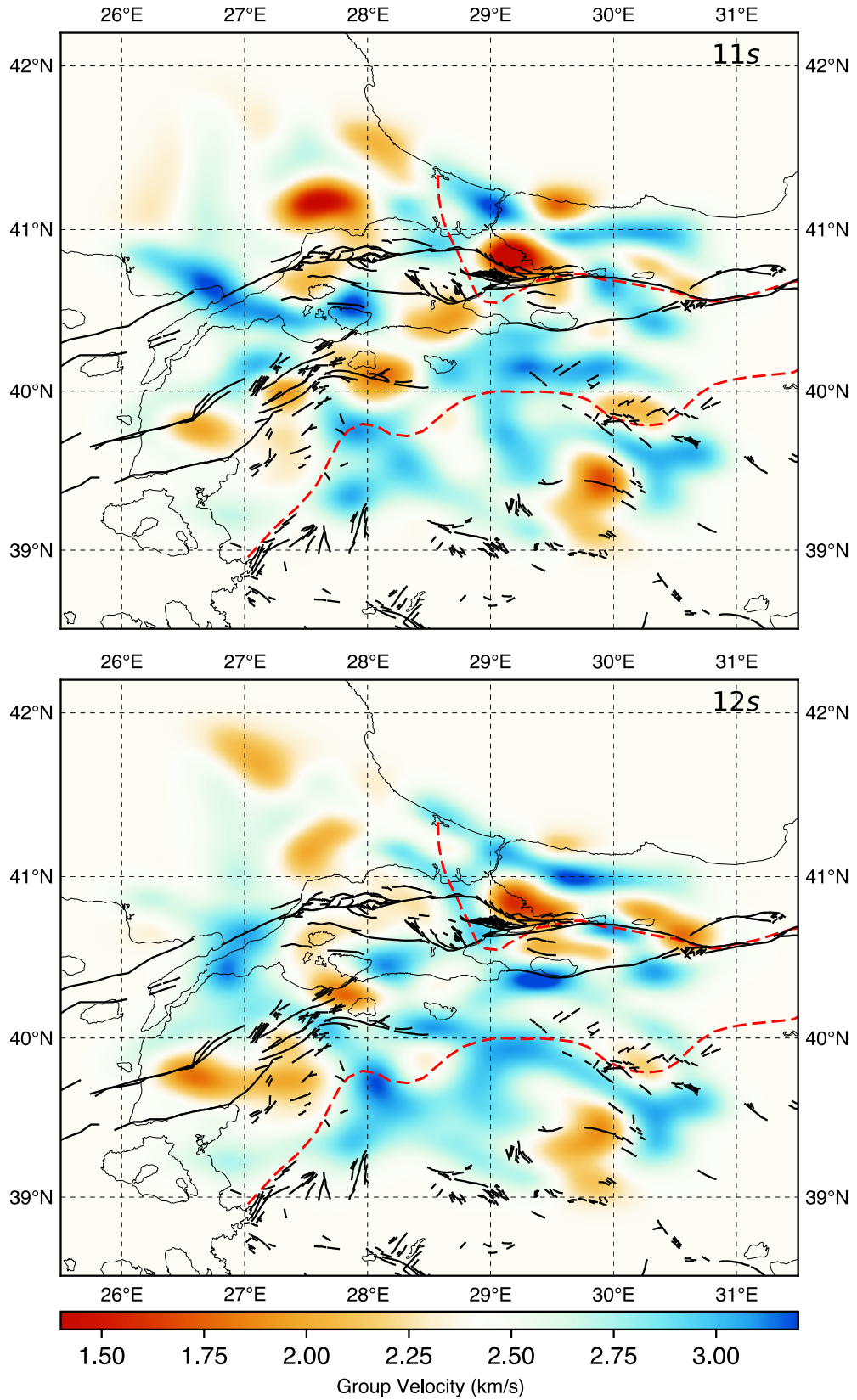


**Figure 6.1 (continued):** Group velocity images obtained from nonlinear tomography for periods between 1 sec and 20 sec. The group velocity ranges between 1.4 km/s and 3.2 km/s. Black lines represent the NAFZ, dashed red lines represent the suture zones.

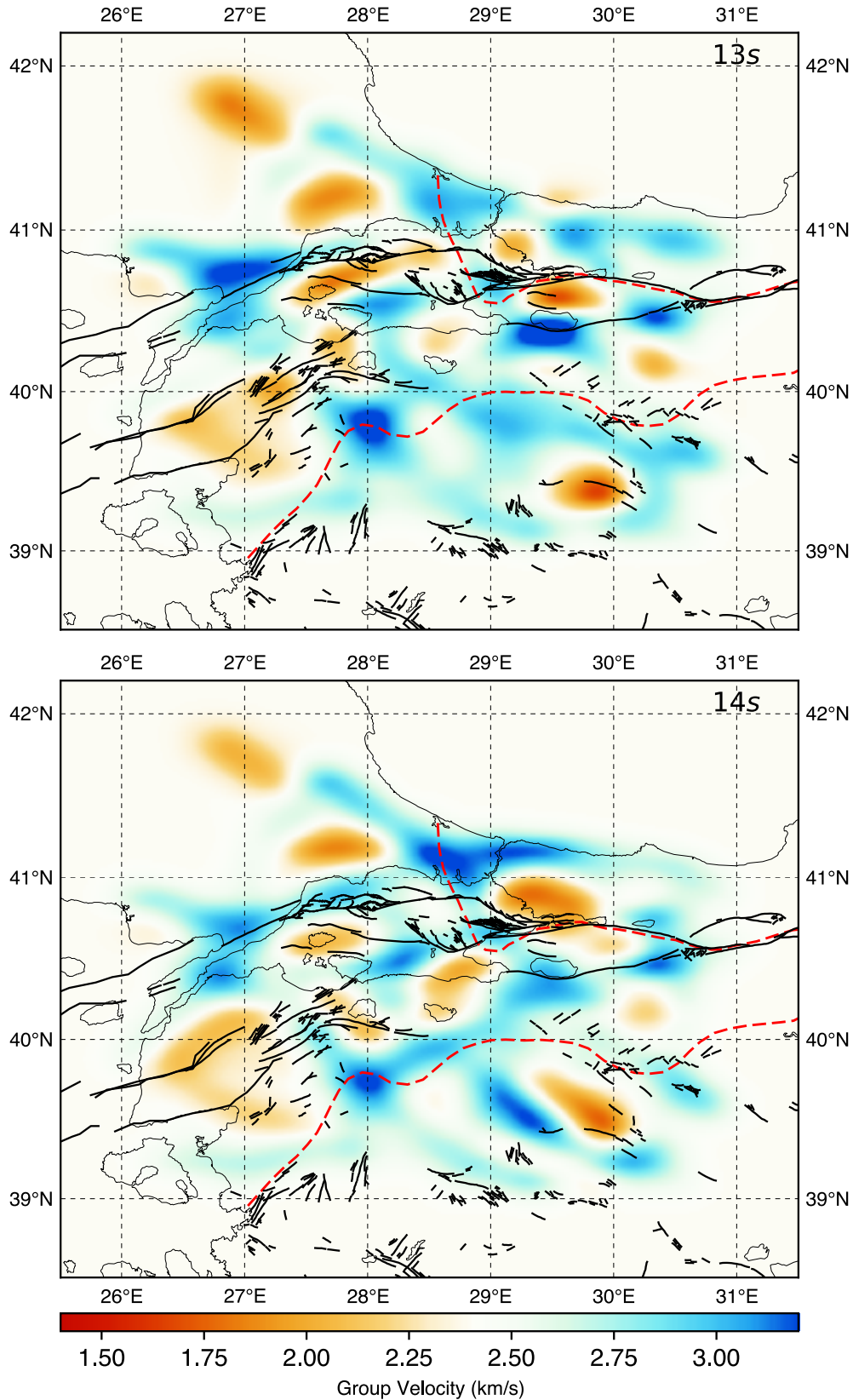


**Figure 6.1 (continued):** Group velocity images obtained from nonlinear tomography for periods between 1 sec and 20 sec. The group velocity ranges between 1.4 km/s and 3.2 km/s. Black lines represent the NAFZ, dashed red lines represent the suture zones.

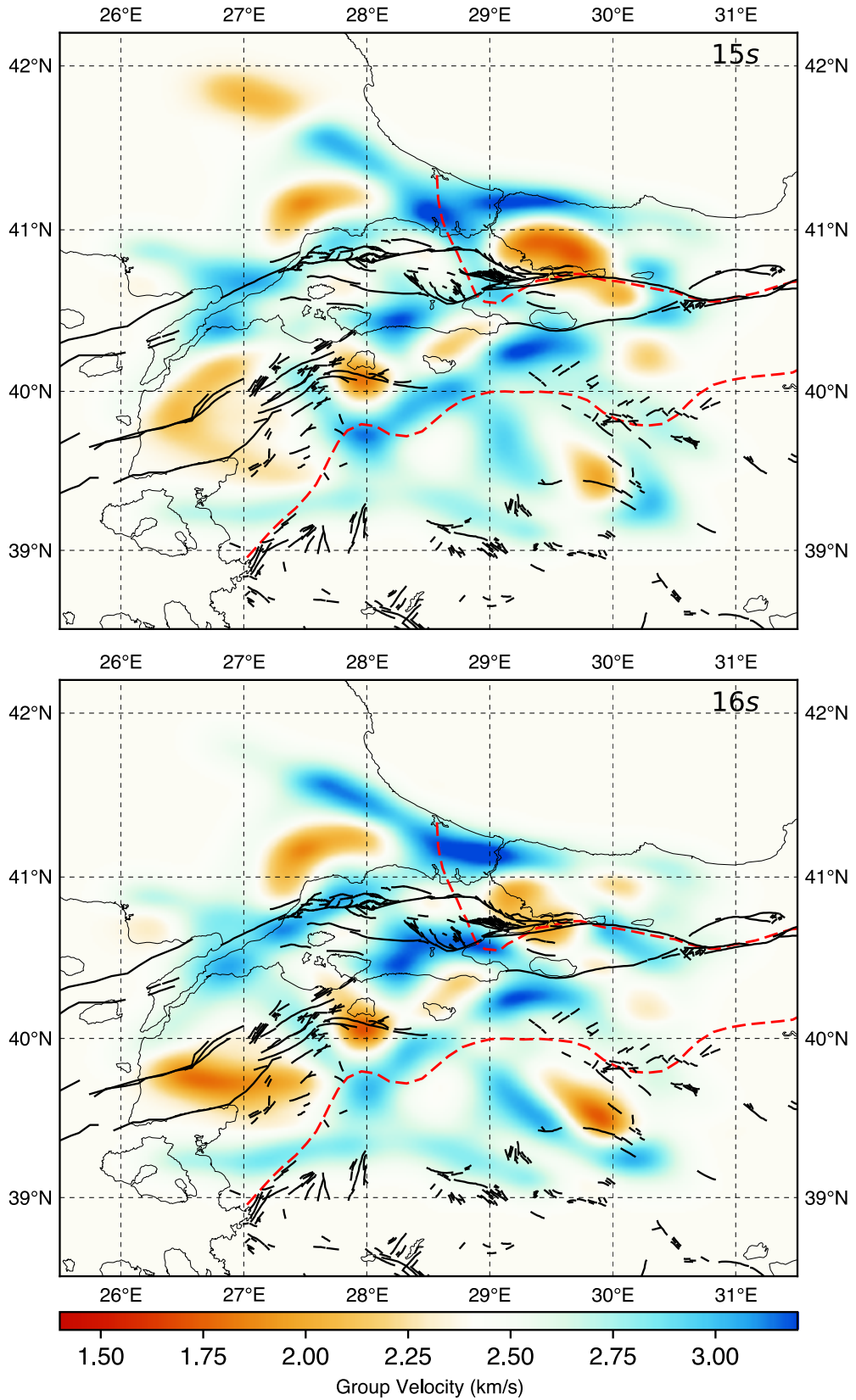


**Figure 6.1 (continued):** Group velocity images obtained from nonlinear tomography for periods between 1 sec and 20 sec. The group velocity ranges between 1.4 km/s and 3.2 km/s. Black lines represent the NAFZ, dashed red lines represent the suture zones.

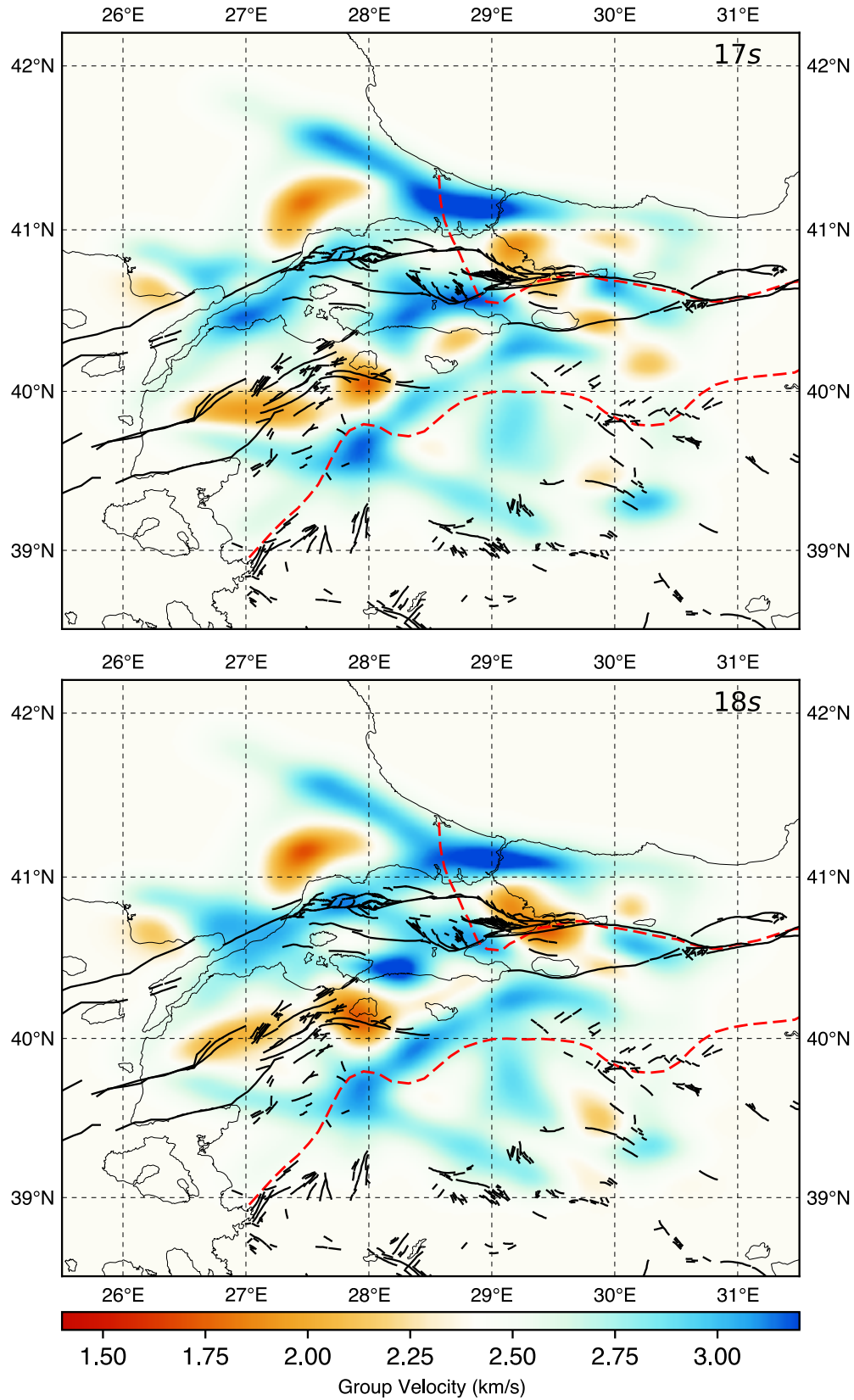


**Figure 6.1 (continued):** Group velocity images obtained from nonlinear tomography for periods between 1 sec and 20 sec. The group velocity ranges between 1.4 km/s and 3.2 km/s. Black lines represent the NAFZ, dashed red lines represent the suture zones.

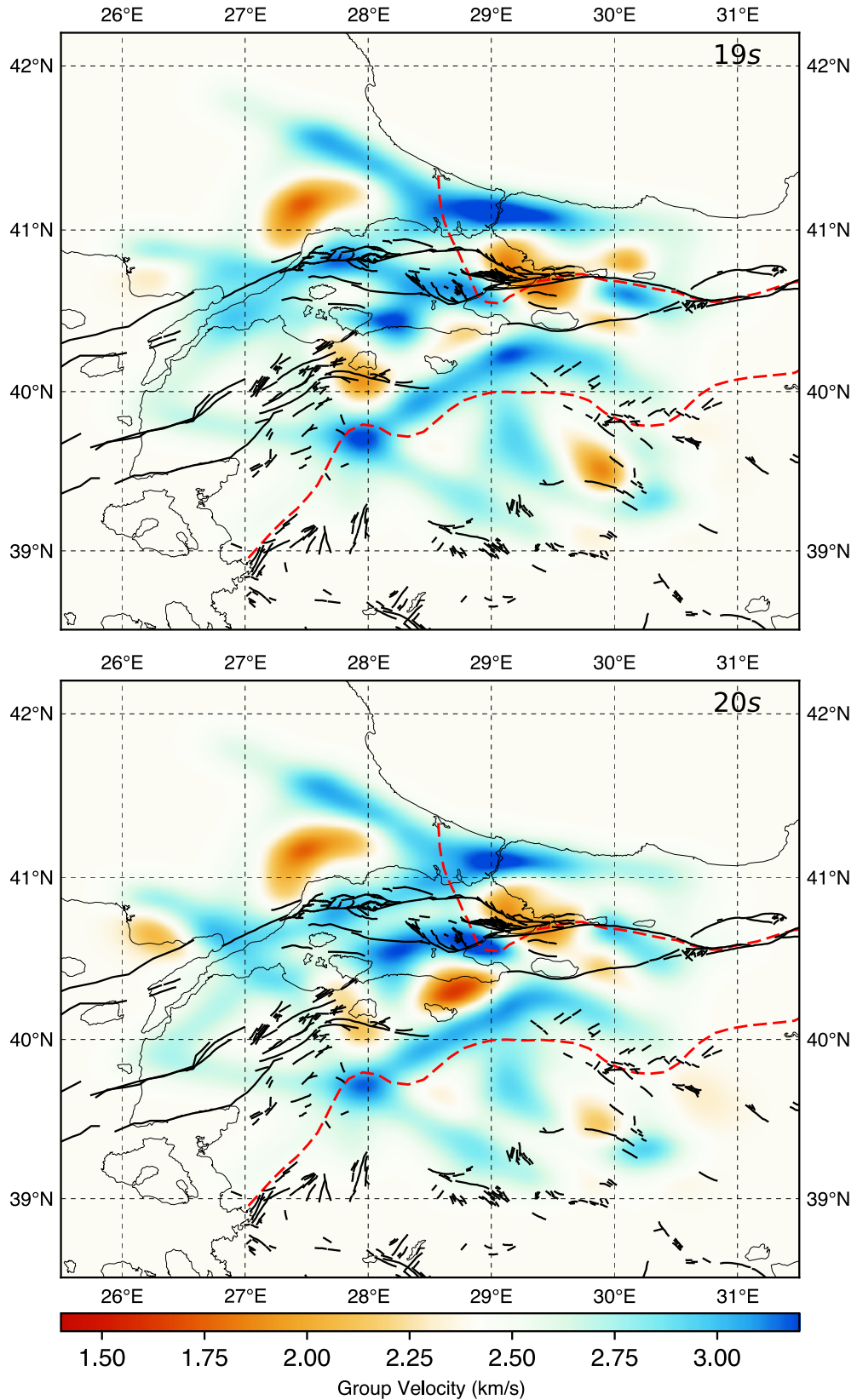


**Figure 6.1 (continued):** Group velocity images obtained from nonlinear tomography for periods between 1 sec and 20 sec. The group velocity ranges between 1.4 km/s and 3.2 km/s. Black lines represent the NAFZ, dashed red lines represent the suture zones.

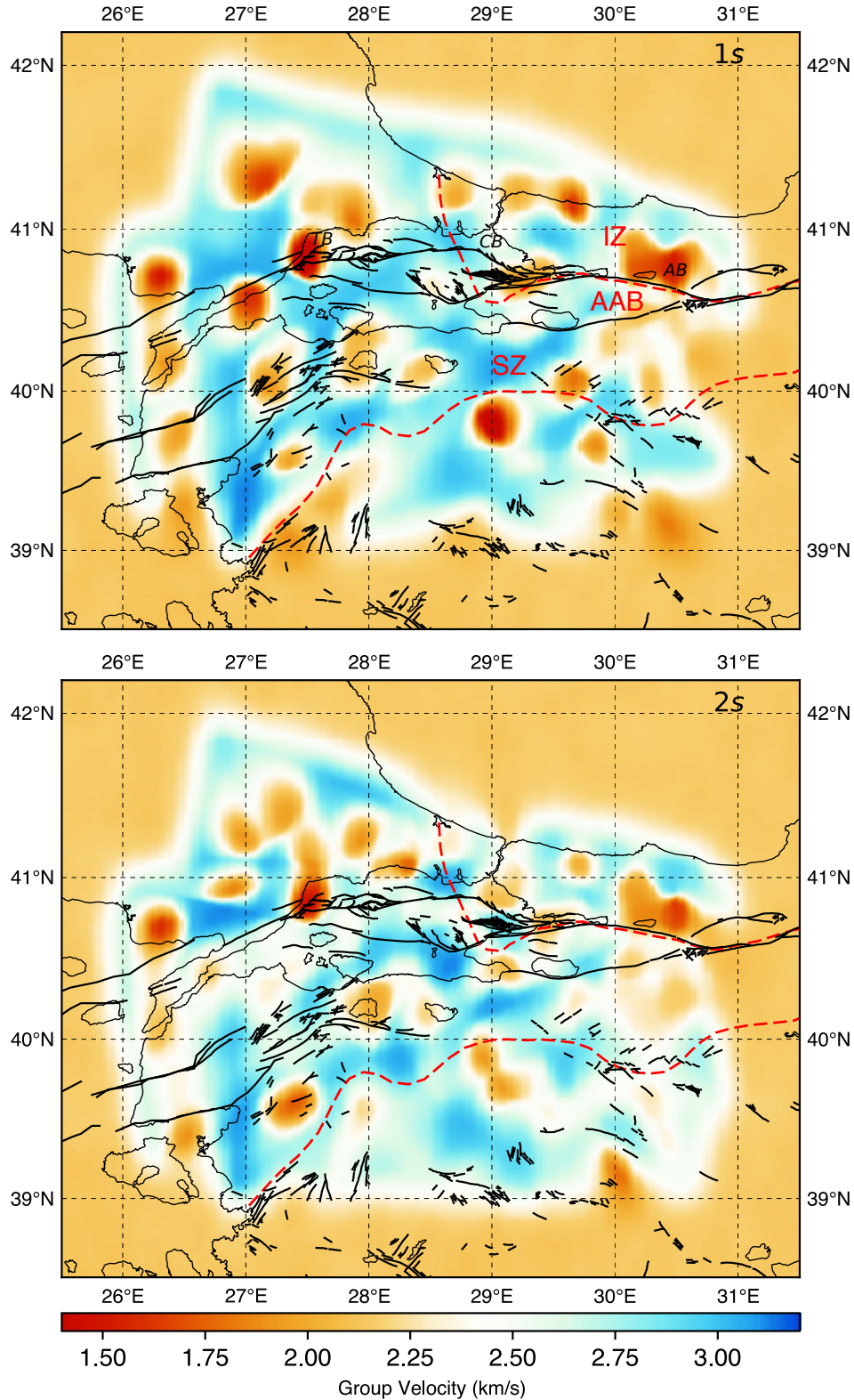


**Figure 6.2:** Group velocity images obtained from Transdimensional Bayesian tomography for periods between 1 sec and 20 sec. The group velocity ranges between 1.4 km/s and 3.2 km/s. Black lines represent the NAFZ, dashed red lines represent the suture zones. AAB: Armutlu-Almacik Block, AB: Adapazari Basin, CB: Cinarcik Basin, IZ: Istanbul Zone, SZ: Sakarya Zone, TB: Tekirdag Basin.

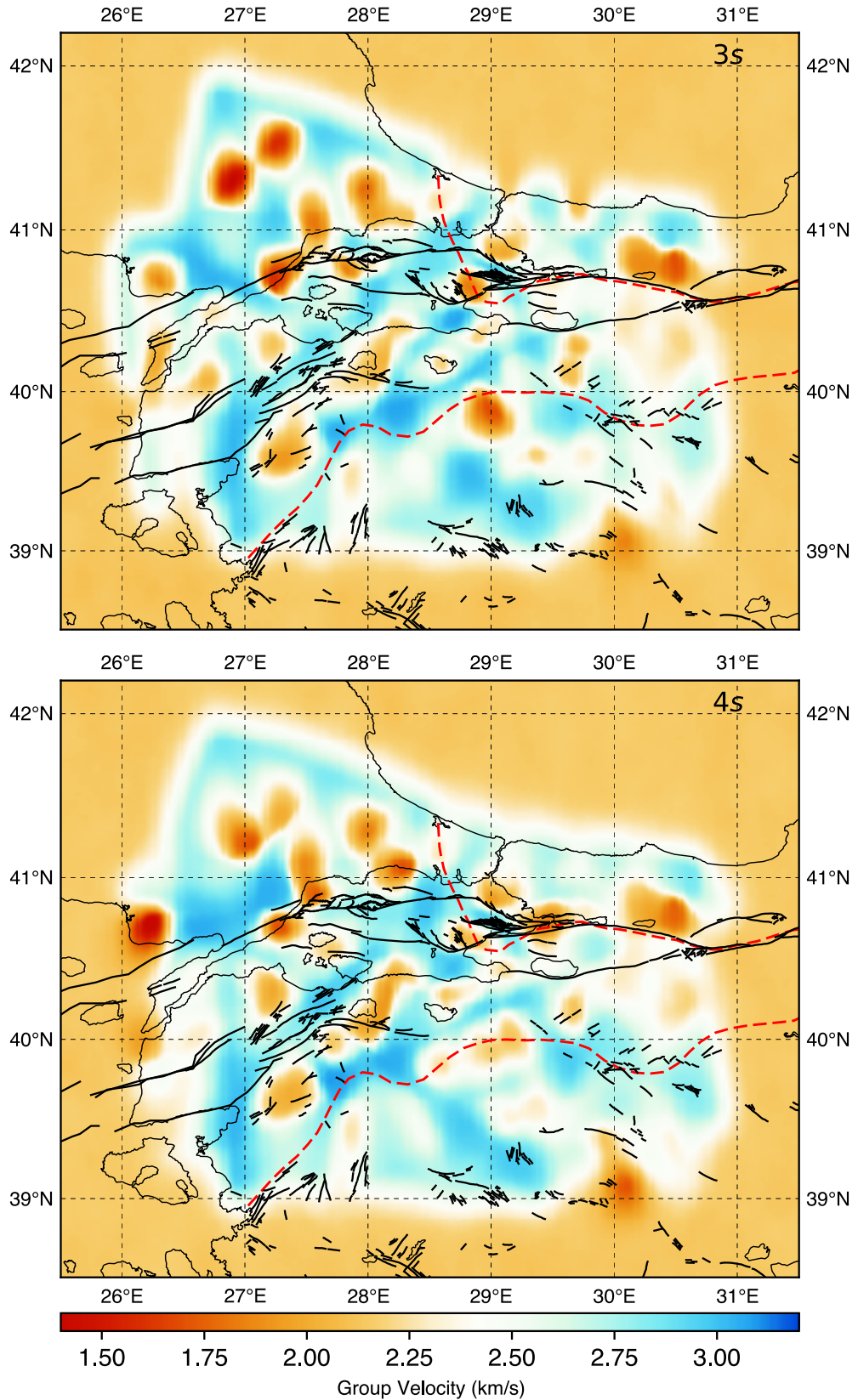


**Figure 6.2 (continued):** Group velocity images obtained from Transdimensional Bayesian tomography for periods between 1 sec and 20 sec. The group velocity ranges between 1.4 km/s and 3.2 km/s. Black lines represent the NAFZ, dashed red lines represent the suture zones.

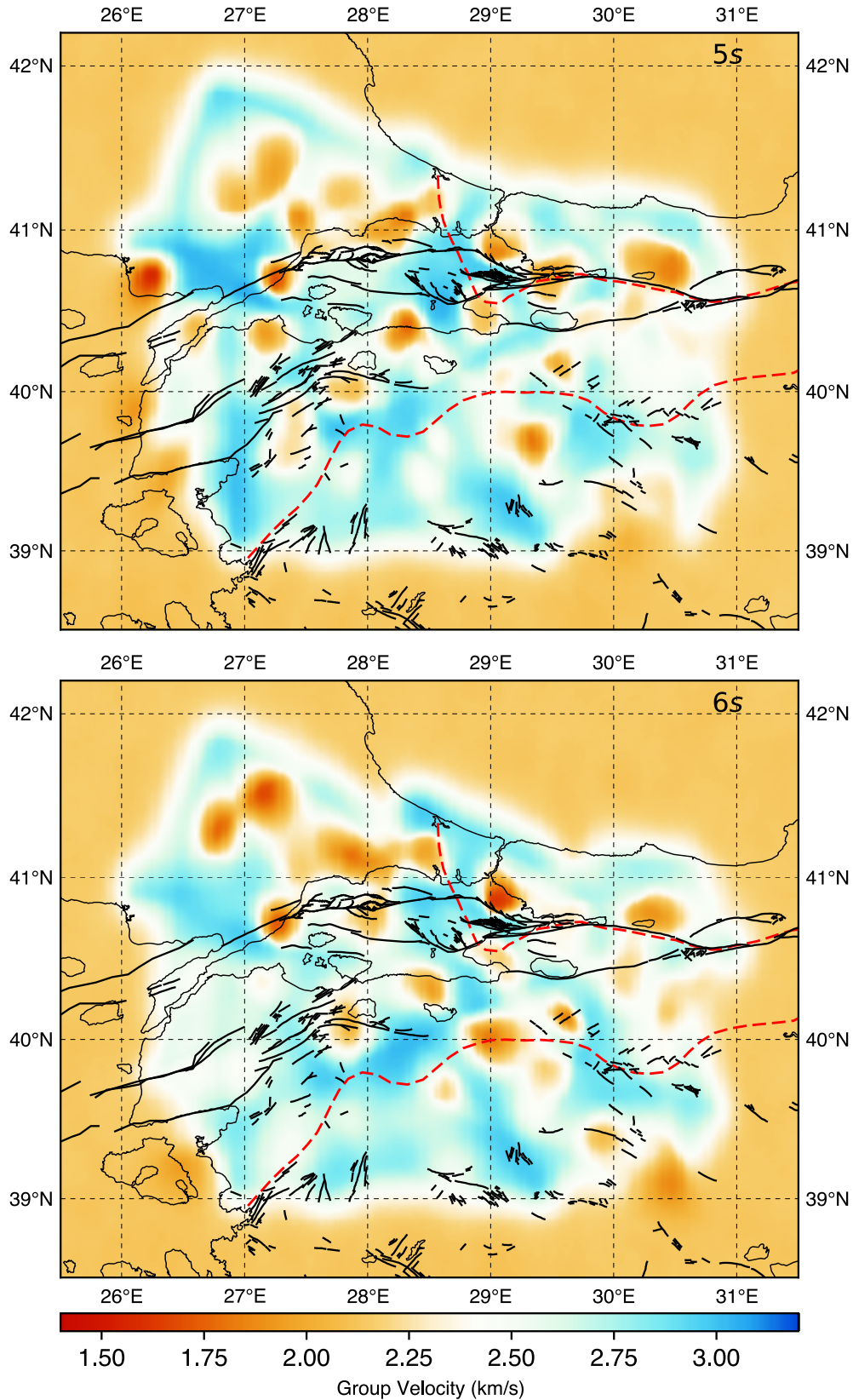


**Figure 6.2 (continued):** Group velocity images obtained from Transdimensional Bayesian tomography for periods between 1 sec and 20 sec. The group velocity ranges between 1.4 km/s and 3.2 km/s. Black lines represent the NAFZ, dashed red lines represent the suture zones.

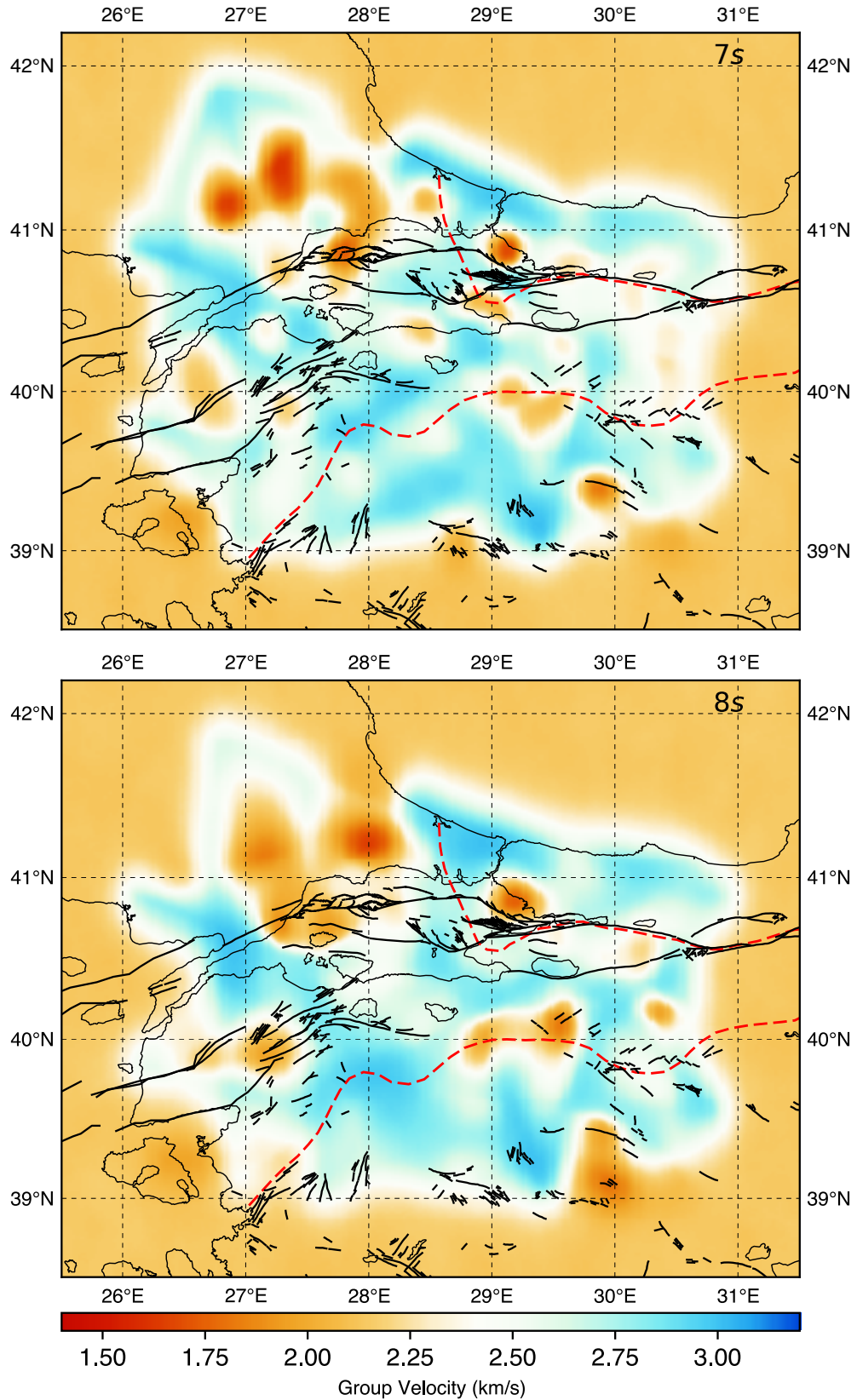


**Figure 6.2 (continued):** Group velocity images obtained from Transdimensional Bayesian tomography for periods between 1 sec and 20 sec. The group velocity ranges between 1.4 km/s and 3.2 km/s. Black lines represent the NAFZ, dashed red lines represent the suture zones.

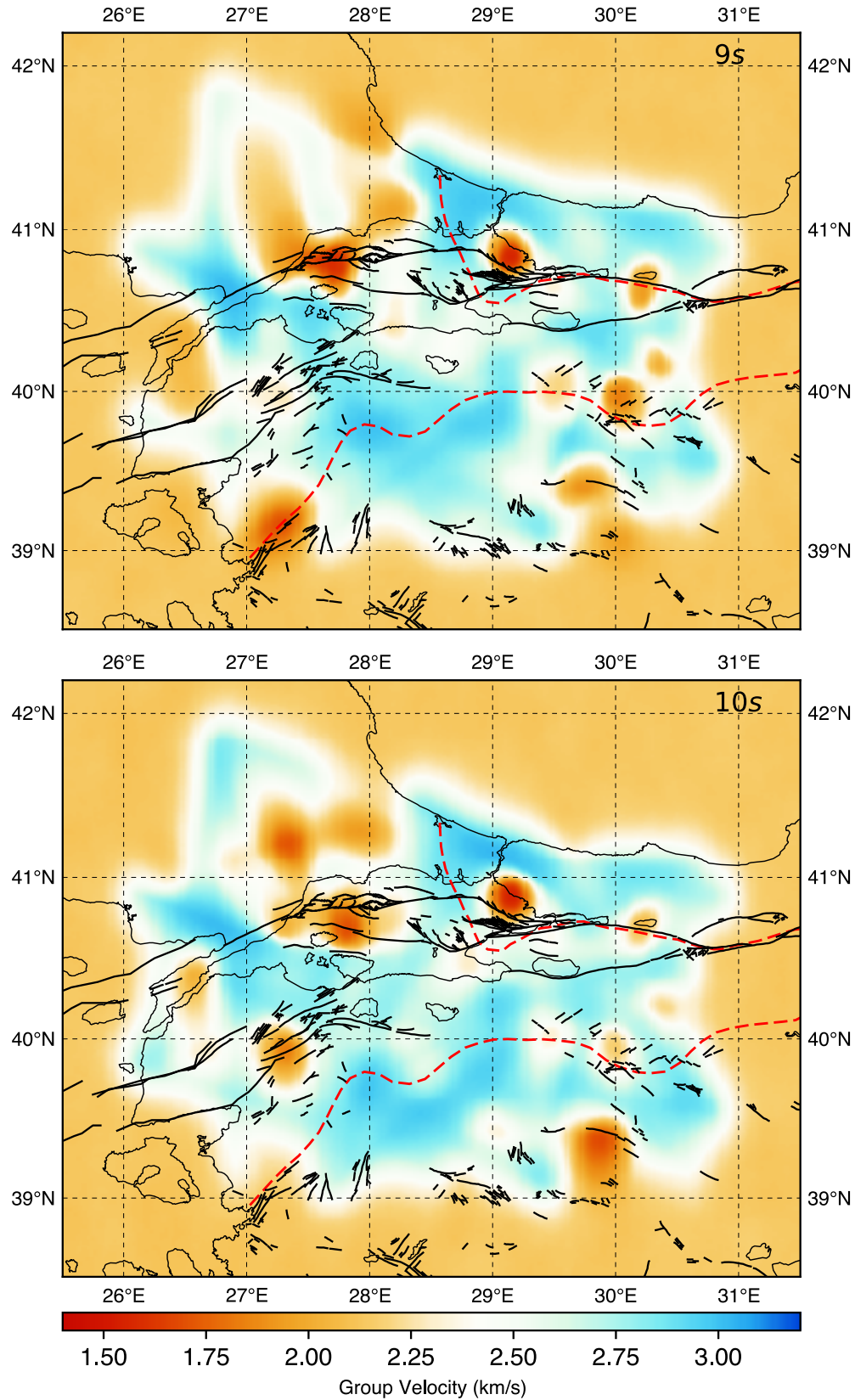


**Figure 6.2 (continued):** Group velocity images obtained from Transdimensional Bayesian tomography for periods between 1 sec and 20 sec. The group velocity ranges between 1.4 km/s and 3.2 km/s. Black lines represent the NAFZ, dashed red lines represent the suture zones.

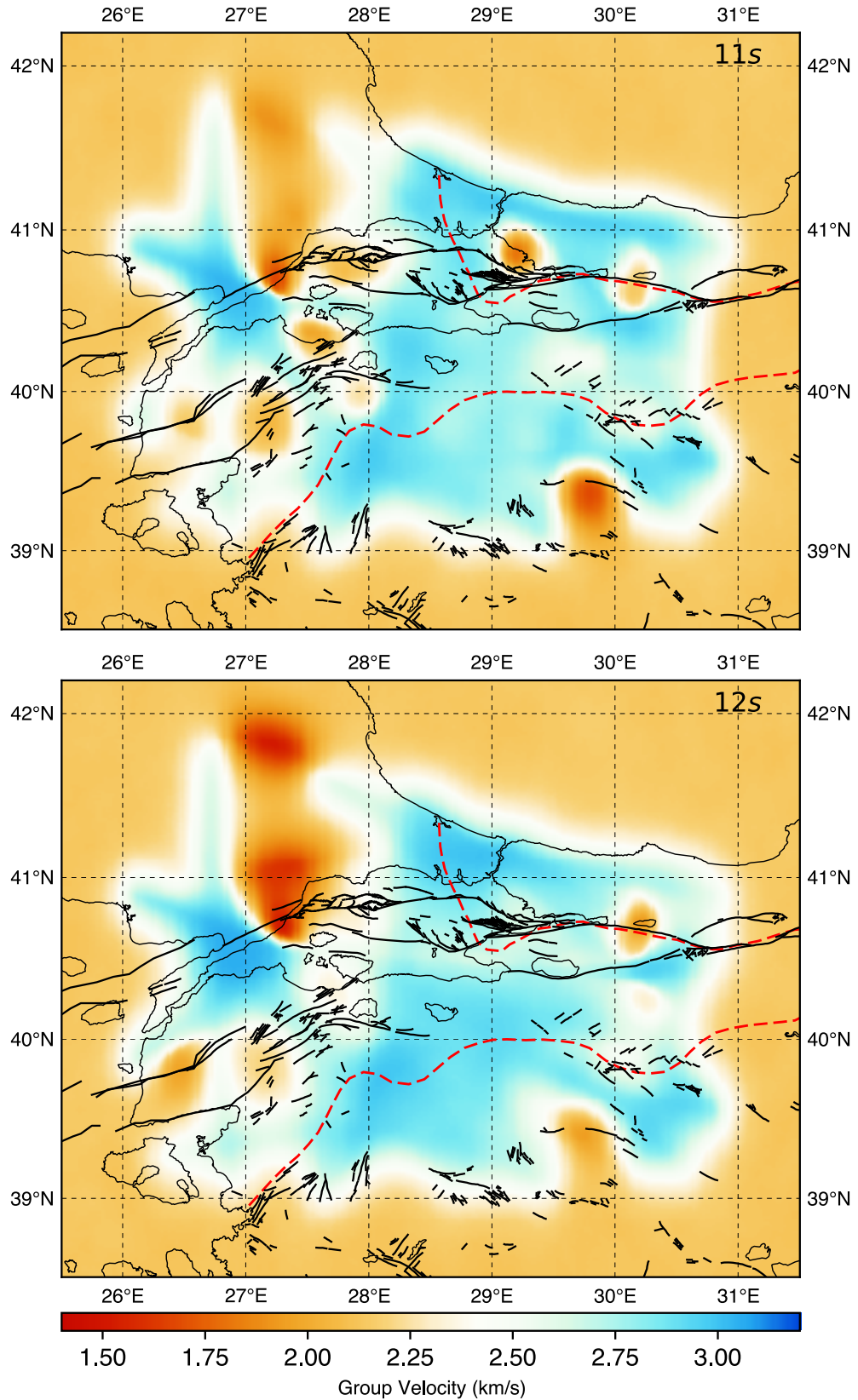


**Figure 6.2 (continued):** Group velocity images obtained from Transdimensional Bayesian tomography for periods between 1 sec and 20 sec. The group velocity ranges between 1.4 km/s and 3.2 km/s. Black lines represent the NAFZ, dashed red lines represent the suture zones.

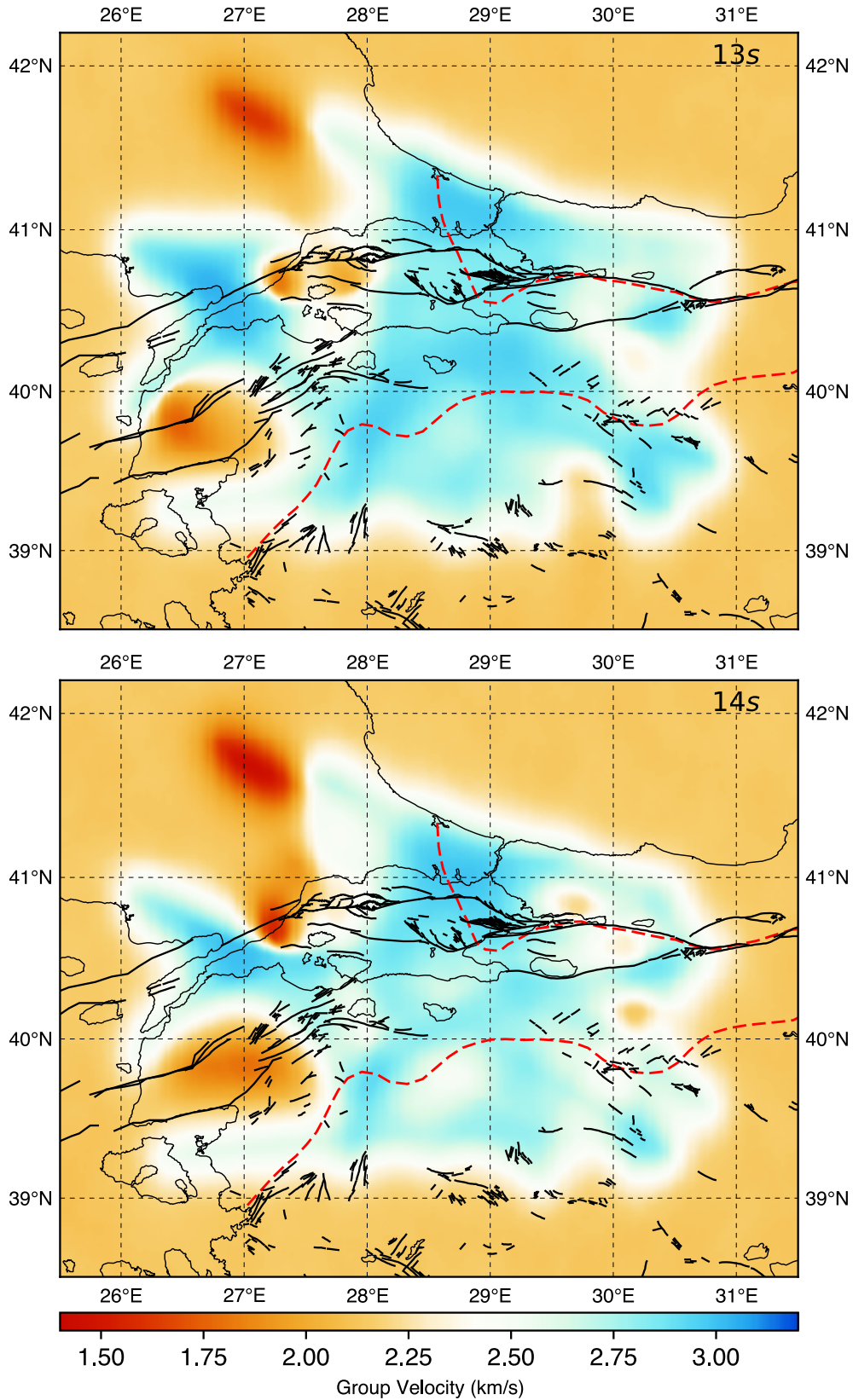


**Figure 6.2 (continued):** Group velocity images obtained from Transdimensional Bayesian tomography for periods between 1 sec and 20 sec. The group velocity ranges between 1.4 km/s and 3.2 km/s. Black lines represent the NAFZ, dashed red lines represent the suture zones.

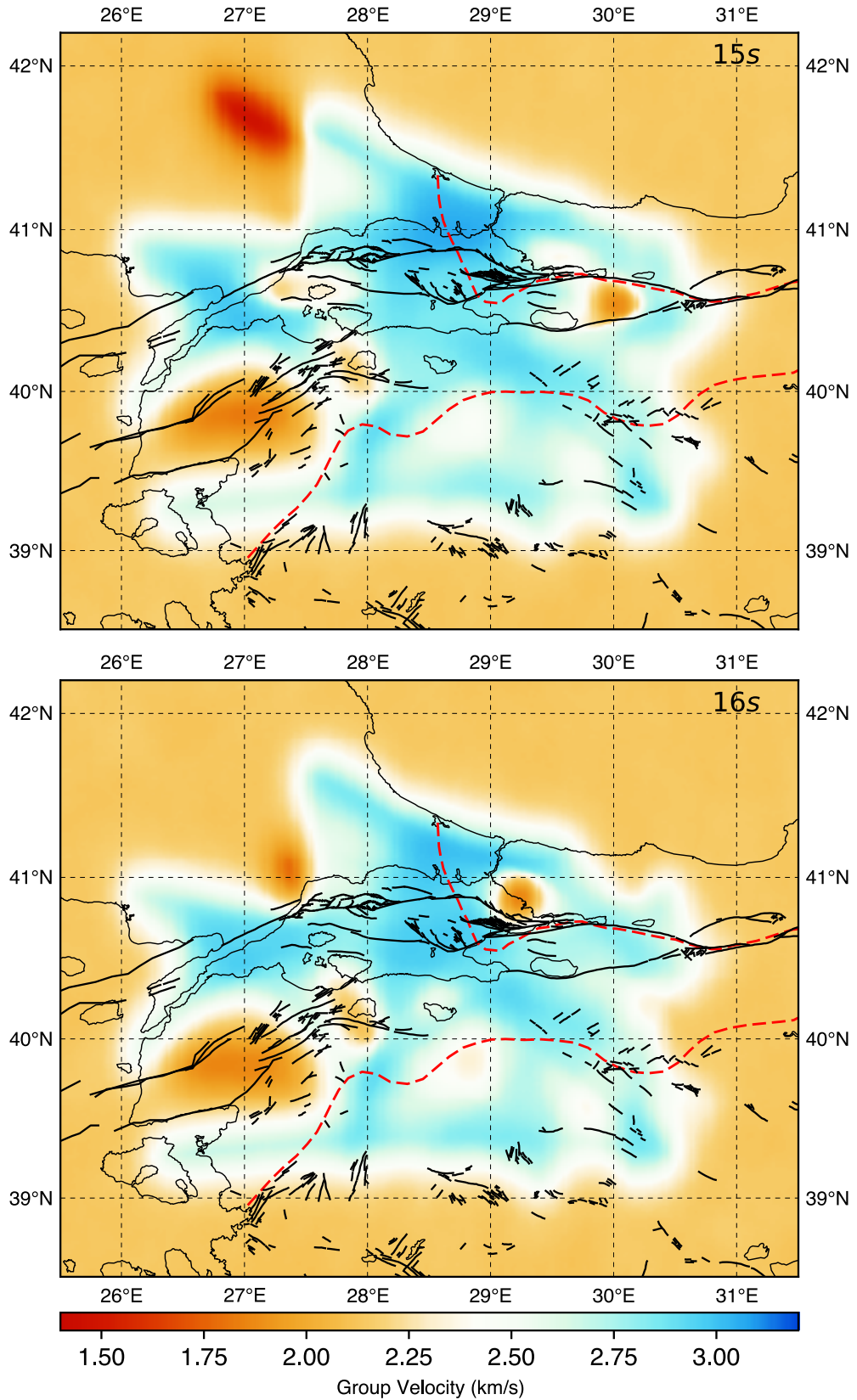


**Figure 6.2 (continued):** Group velocity images obtained from Transdimensional Bayesian tomography for periods between 1 sec and 20 sec. The group velocity ranges between 1.4 km/s and 3.2 km/s. Black lines represent the NAFZ, dashed red lines represent the suture zones.

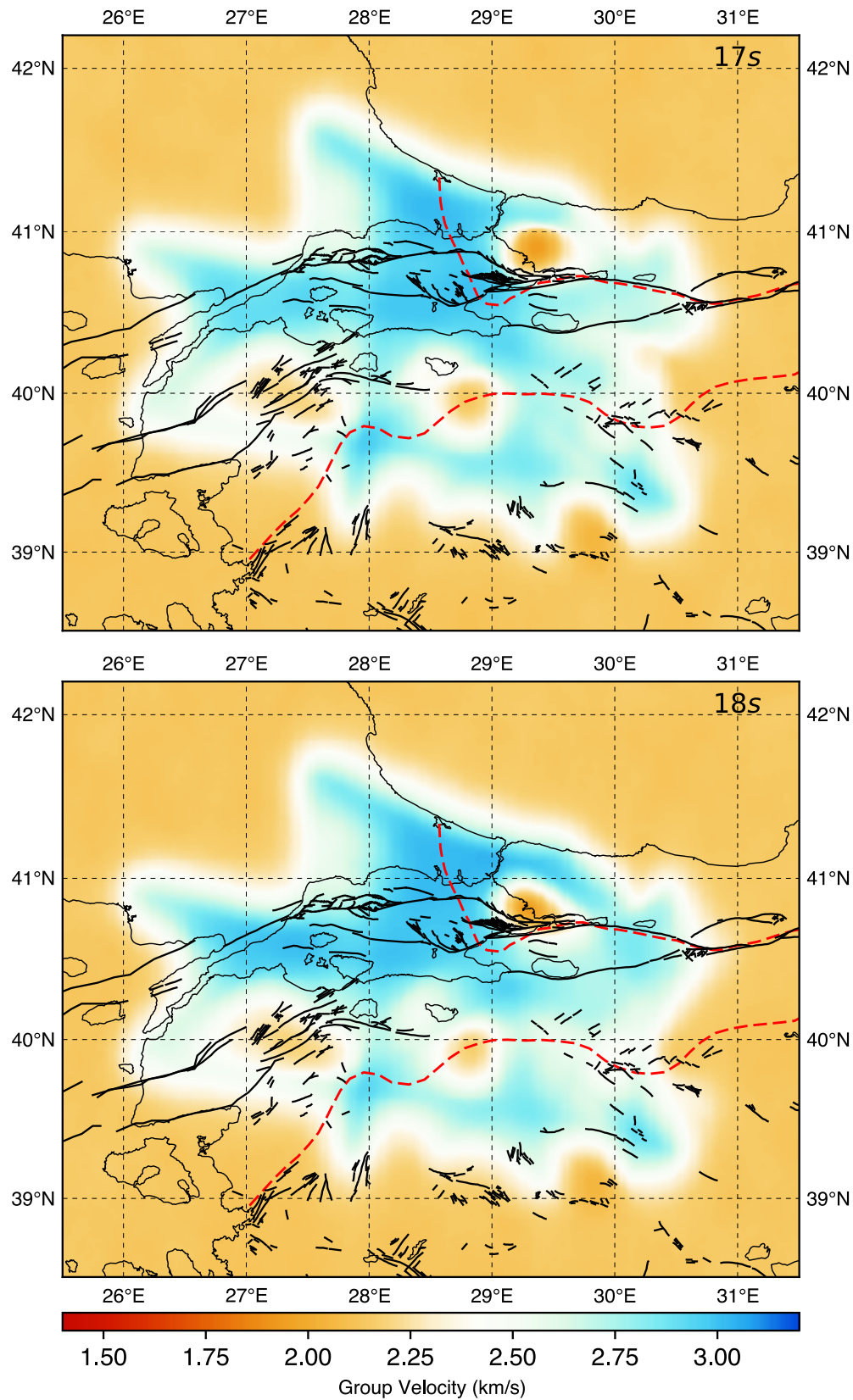


**Figure 6.2 (continued):** Group velocity images obtained from Transdimensional Bayesian tomography for periods between 1 sec and 20 sec. The group velocity ranges between 1.4 km/s and 3.2 km/s. Black lines represent the NAFZ, dashed red lines represent the suture zones.

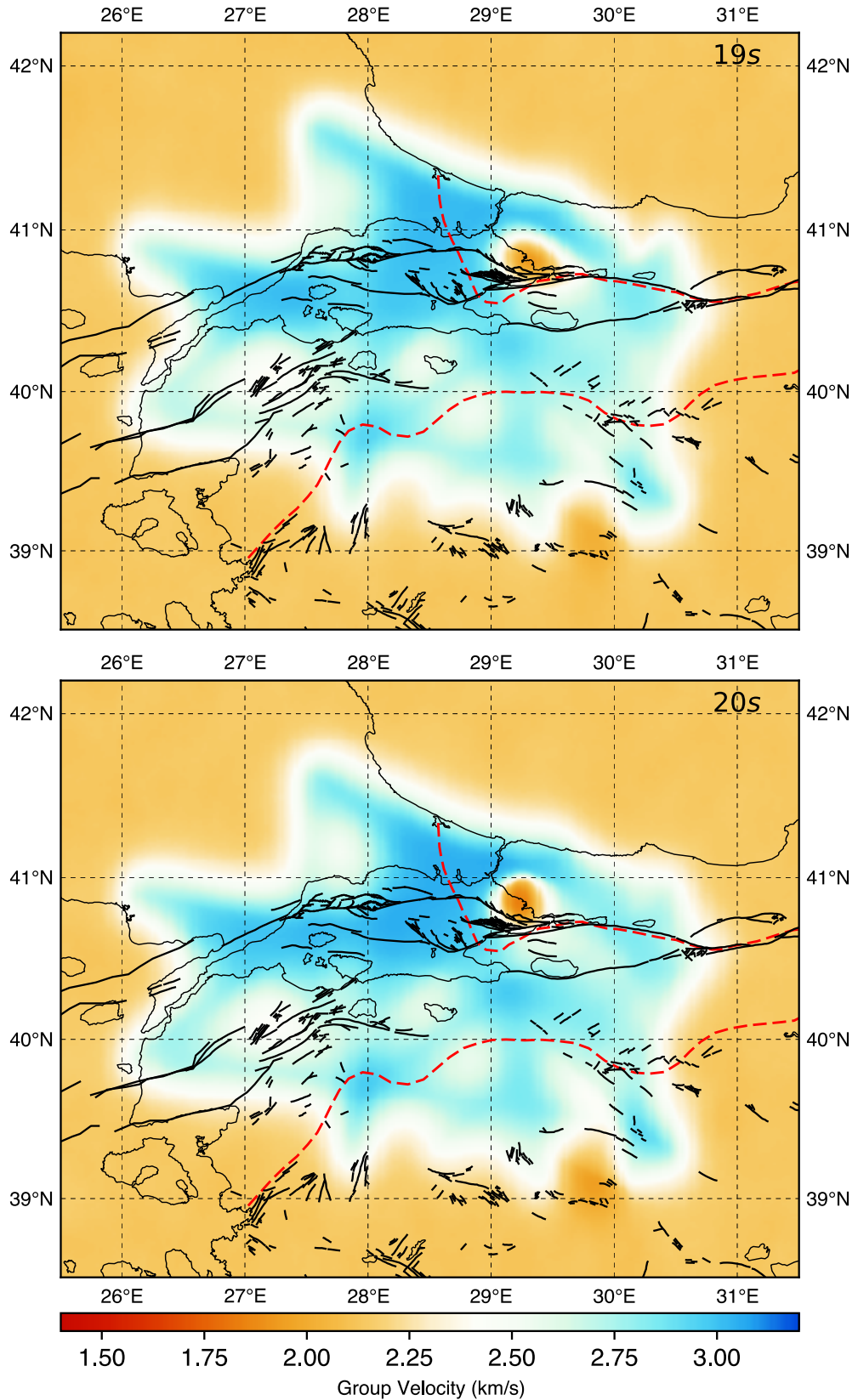


**Figure 6.2 (continued):** Group velocity images obtained from Transdimensional Bayesian tomography for periods between 1 sec and 20 sec. The group velocity ranges between 1.4 km/s and 3.2 km/s. Black lines represent the NAFZ, dashed red lines represent the suture zones.

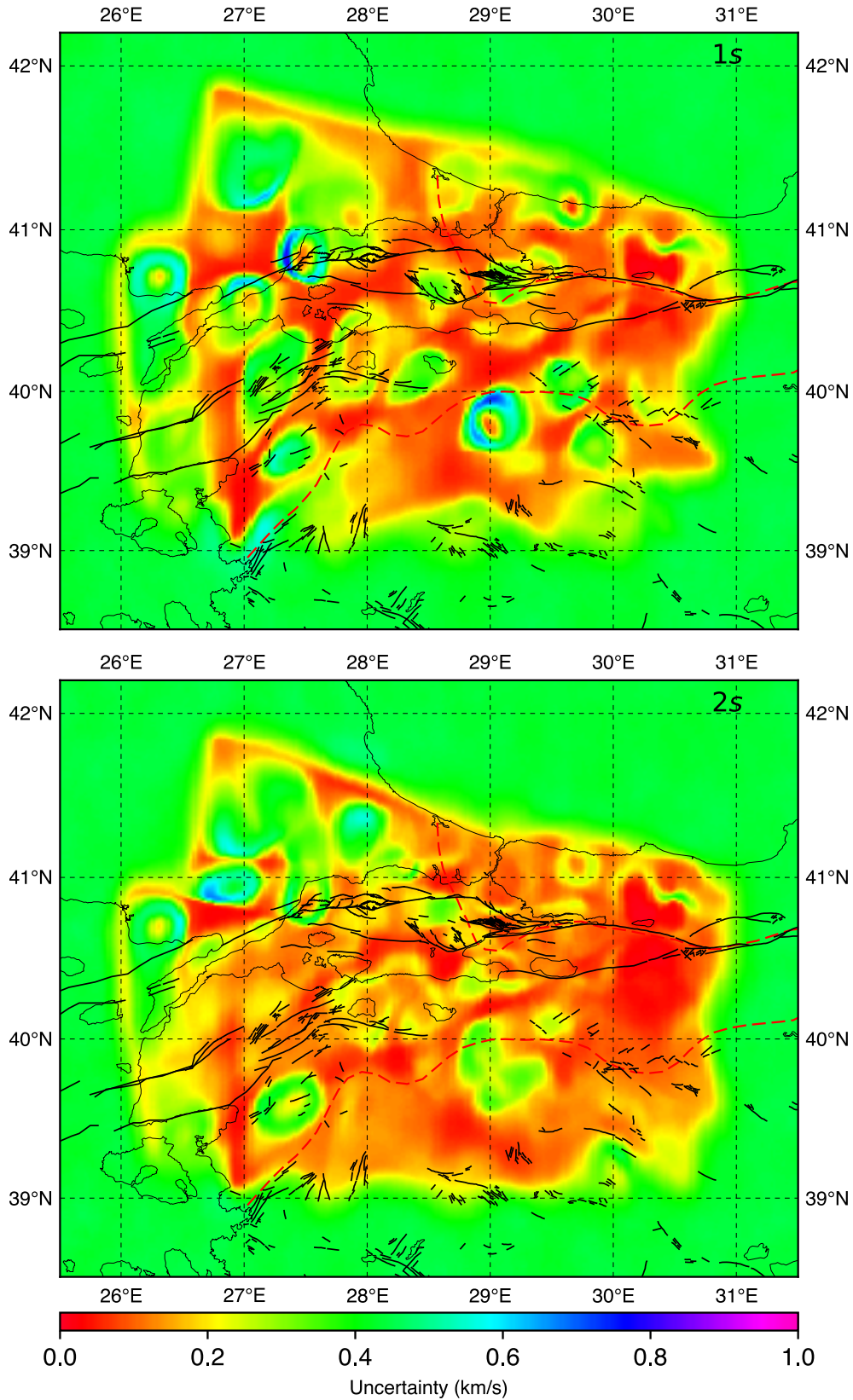


**Figure 6.3:** The uncertainty maps for periods 1-20 sec, The uncertainty tanges between 0.0-1.0 km/s. 0.0 km/s represents the lowest uncertainty and 1.0 km/s represents the highest uncertainty. Black lines represent the NAFZ, dashed red lines represent the suture zones.

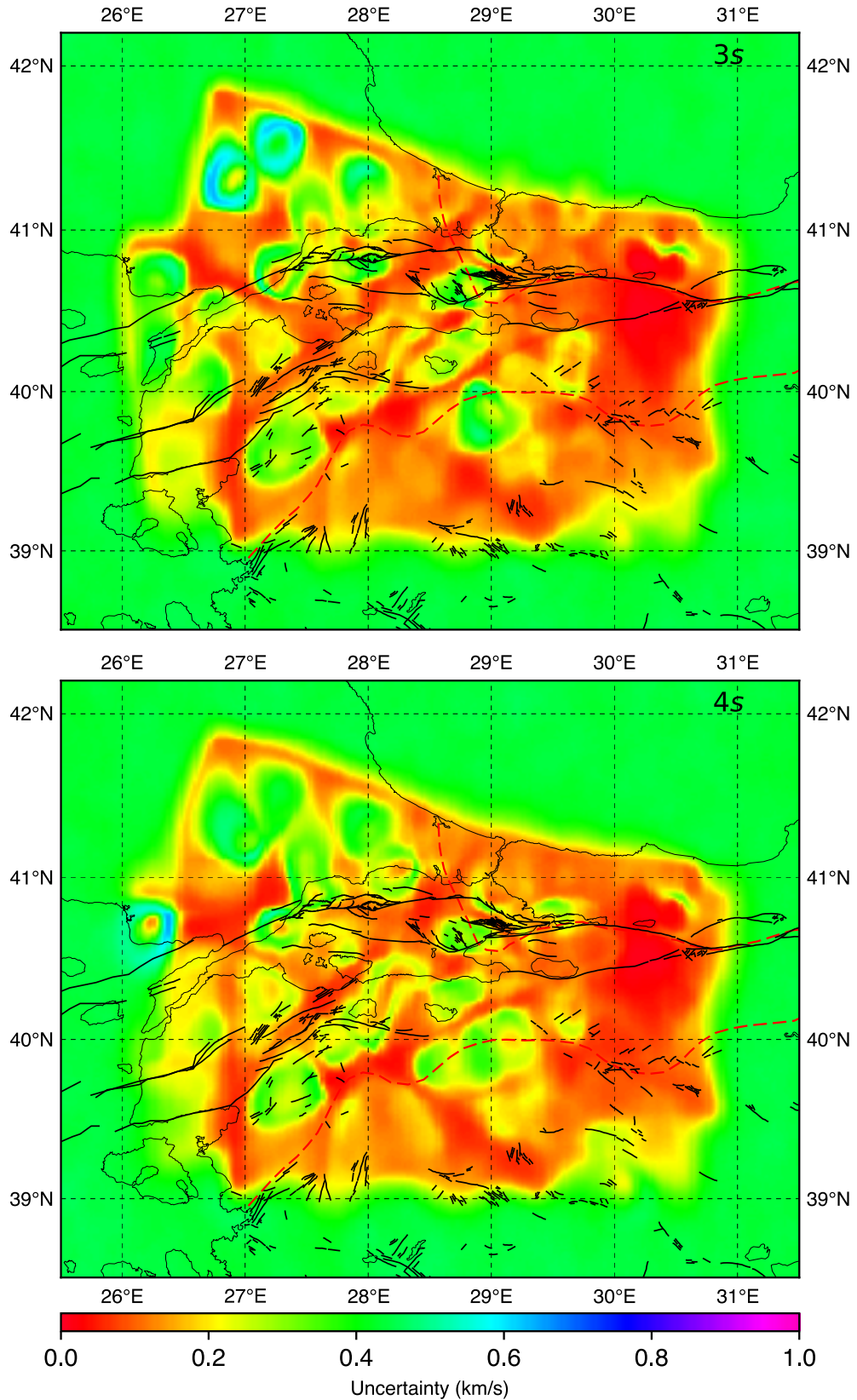


**Figure 6.3 (continued):** The uncertainty maps for periods 1-20 sec, The uncertainty tanges between 0.0-1.0 km/s. 0.0 km/s represents the lowest uncertainty and 1.0 km/s represents the highest uncertainty. Black lines represent the NAFZ, dashed red lines represent the suture zones.

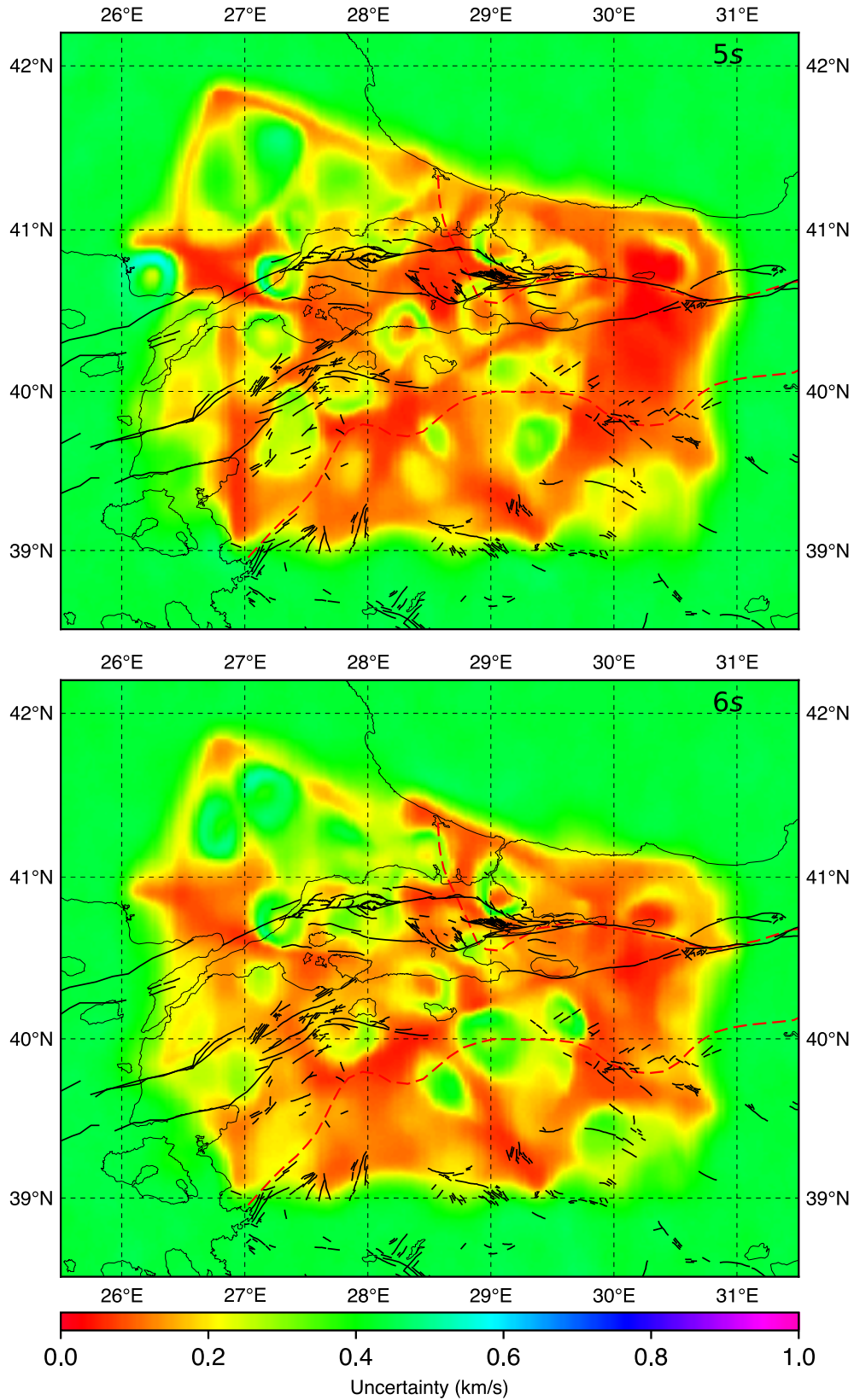


**Figure 6.3 (continued):** The uncertainty maps for periods 1-20 sec, The uncertainty tanges between 0.0-1.0 km/s. 0.0 km/s represents the lowest uncertainty and 1.0 km/s represents the highest uncertainty. Black lines represent the NAFZ, dashed red lines represent the suture zones.

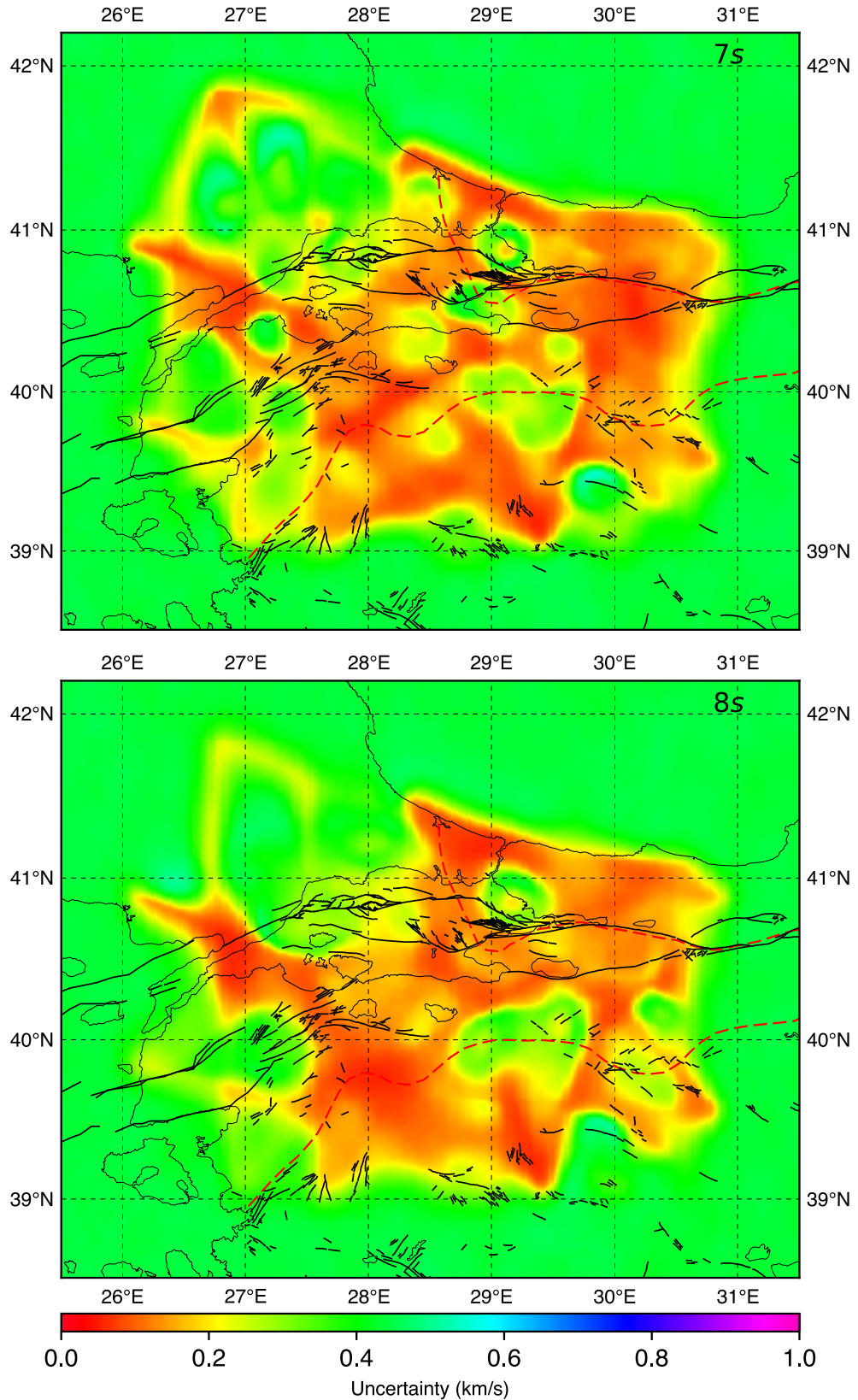


**Figure 6.3 (continued):** The uncertainty maps for periods 1-20 sec, The uncertainty tanges between 0.0-1.0 km/s. 0.0 km/s represents the lowest uncertainty and 1.0 km/s represents the highest uncertainty. Black lines represent the NAFZ, dashed red lines represent the suture zones.

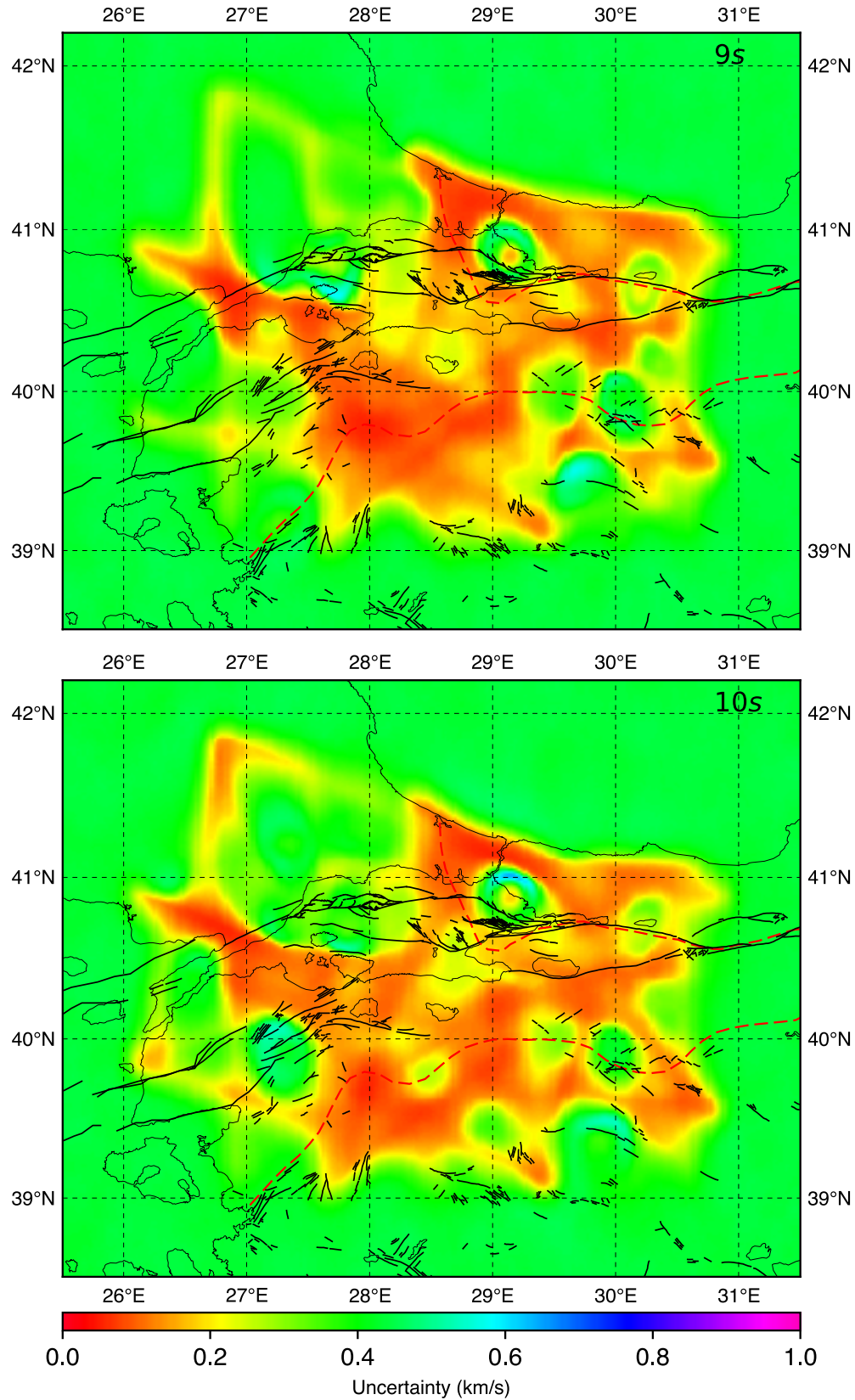


**Figure 6.3 (continued):** The uncertainty maps for periods 1-20 sec, The uncertainty tanges between 0.0-1.0 km/s. 0.0 km/s represents the lowest uncertainty and 1.0 km/s represents the highest uncertainty. Black lines represent the NAFZ, dashed red lines represent the suture zones.

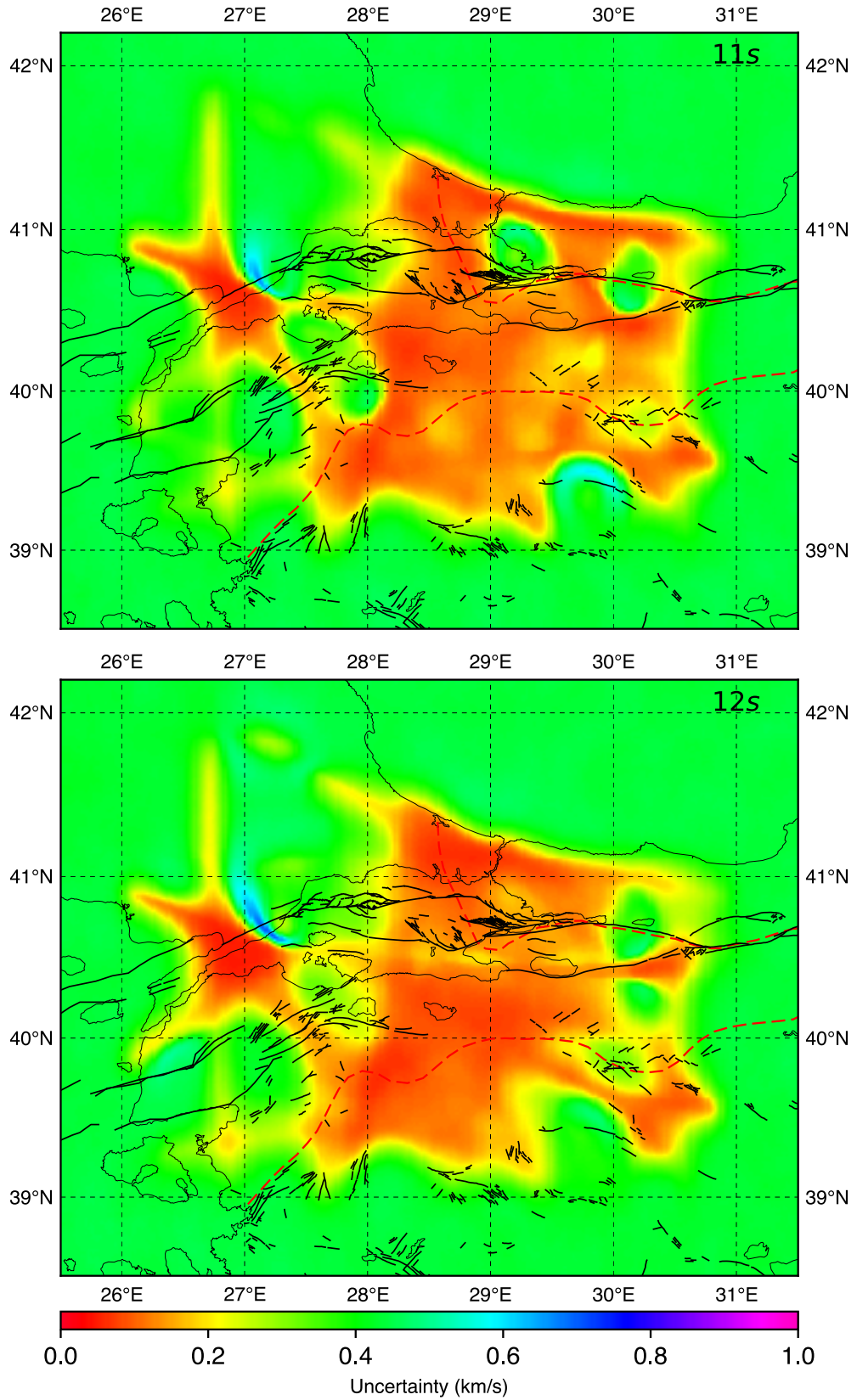


**Figure 6.3 (continued):** The uncertainty maps for periods 1-20 sec, The uncertainty tanges between 0.0-1.0 km/s. 0.0 km/s represents the lowest uncertainty and 1.0 km/s represents the highest uncertainty. Black lines represent the NAFZ, dashed red lines represent the suture zones.

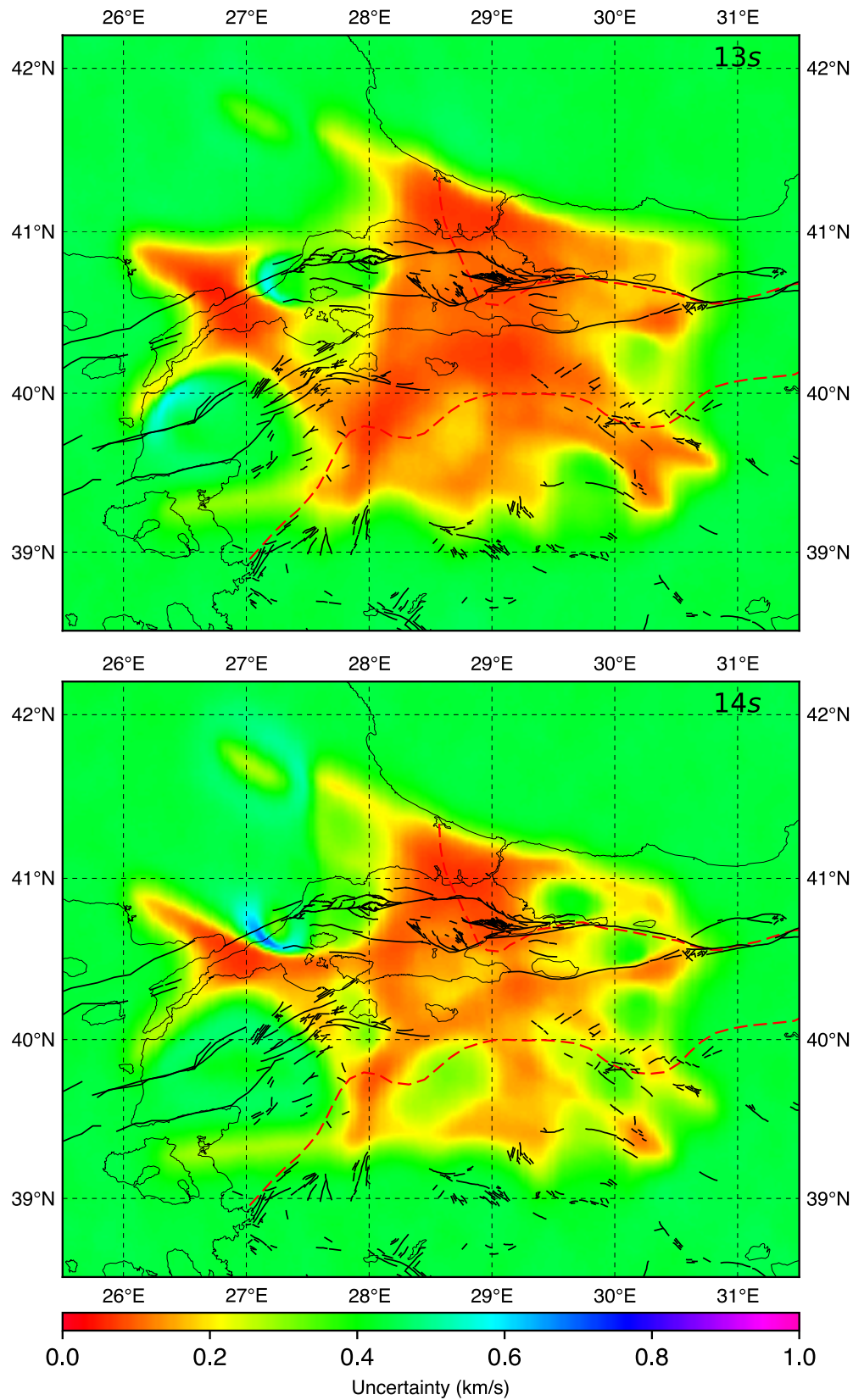


**Figure 6.3 (continued):** The uncertainty maps for periods 1-20 sec, The uncertainty tanges between 0.0-1.0 km/s. 0.0 km/s represents the lowest uncertainty and 1.0 km/s represents the highest uncertainty. Black lines represent the NAFZ, dashed red lines represent the suture zones.

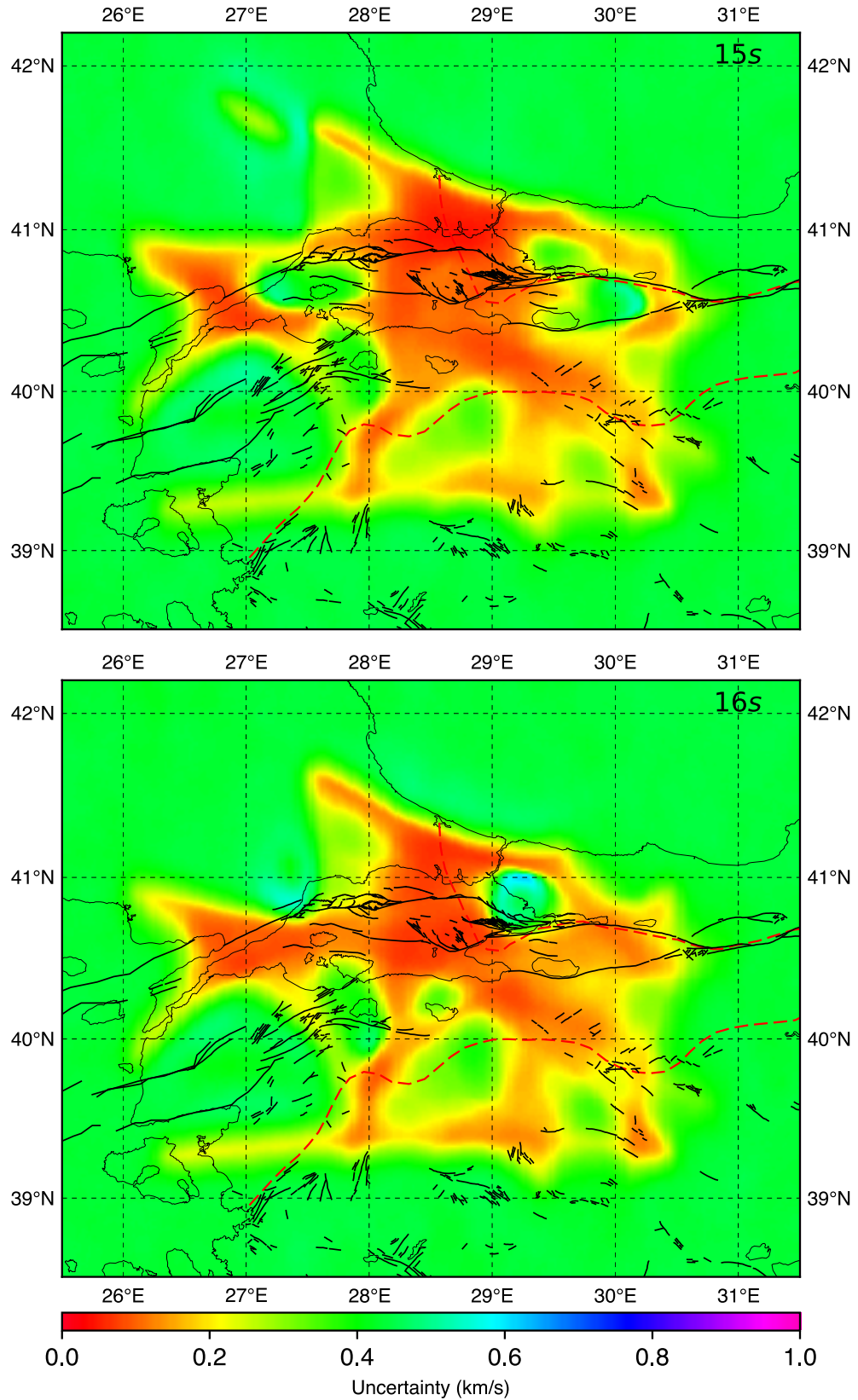


**Figure 6.3 (continued):** The uncertainty maps for periods 1-20 sec, The uncertainty tanges between 0.0-1.0 km/s. 0.0 km/s represents the lowest uncertainty and 1.0 km/s represents the highest uncertainty. Black lines represent the NAFZ, dashed red lines represent the suture zones.

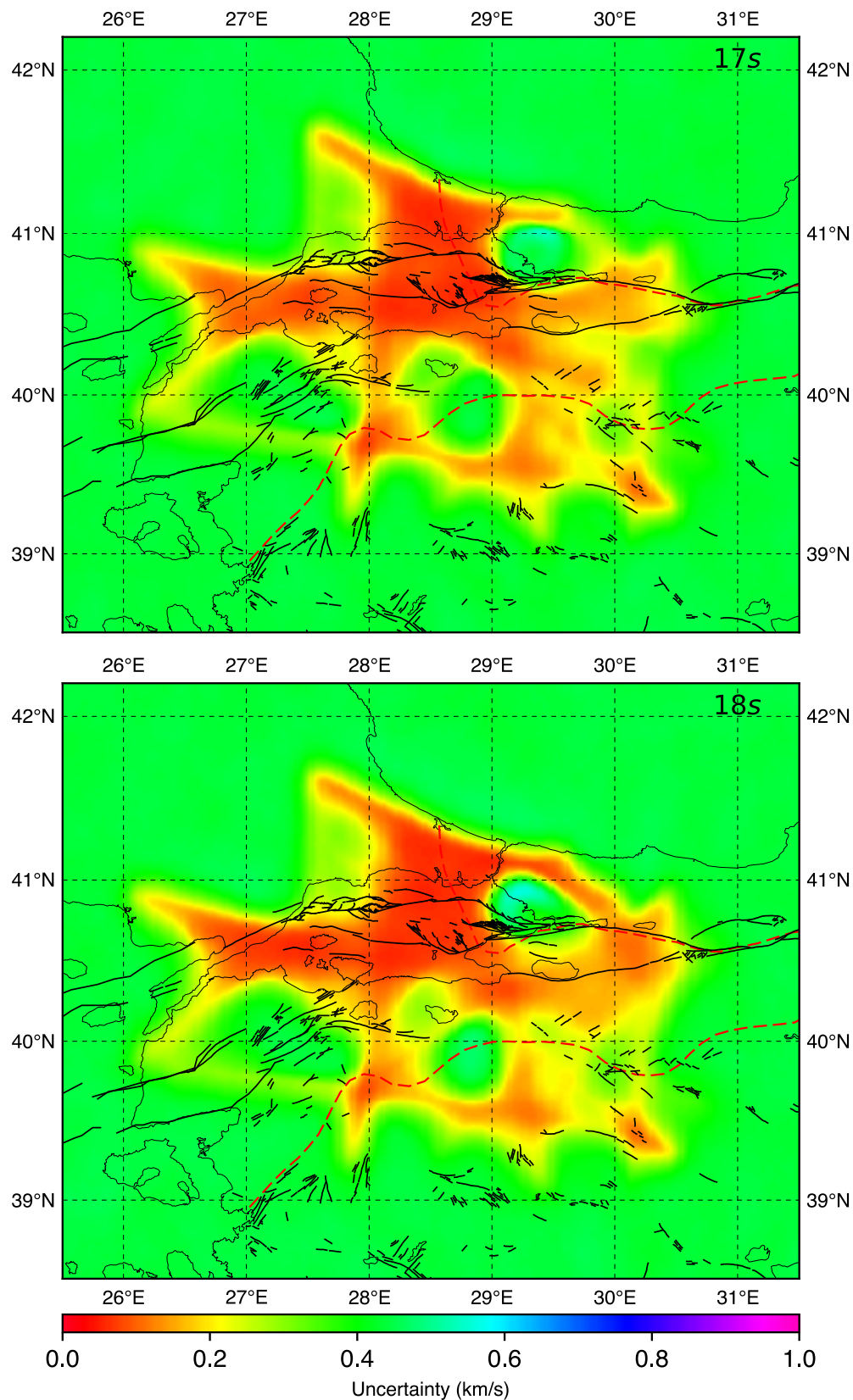


**Figure 6.3 (continued):** The uncertainty maps for periods 1-20 sec, The uncertainty tanges between 0.0-1.0 km/s. 0.0 km/s represents the lowest uncertainty and 1.0 km/s represents the highest uncertainty. Black lines represent the NAFZ, dashed red lines represent the suture zones.

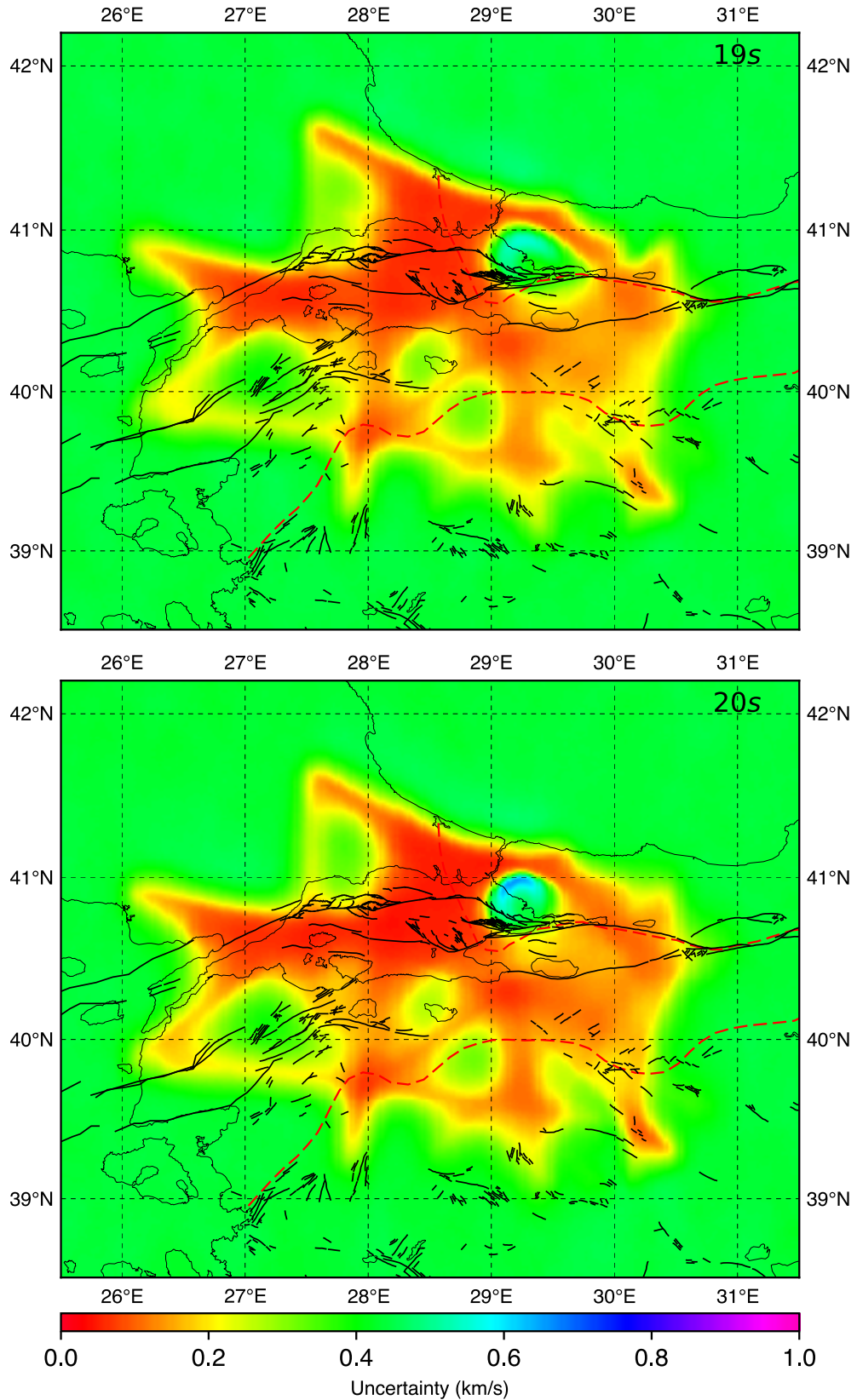


**Figure 6.3 (continued):** The uncertainty maps for periods 1-20 sec, The uncertainty tanges between 0.0-1.0 km/s. 0.0 km/s represents the lowest uncertainty and 1.0 km/s represents the highest uncertainty. Black lines represent the NAFZ, dashed red lines represent the suture zones.



## 7. CONCLUSION

We have established a Rayleigh wave Green function database via correlations of long sequences of ambient seismic noise along the northwest part of Anatolia including regions the Sea of Marmara to the west and three tectonic units separated by branches of the NAFZ to the east. Our data set does not depend on recorded seismicity at any given stations but instead, noise recorded at two stations. Thus, using ambient noise can bring advantageous in case of imaging where local seismic activity is absent or very limited due to the instrumental difficulties (insufficient number of permanent Ocean Bottom Seismometers-OBS, etc.).

Transdimensional Bayesian inversion method and nonlinear tomography inversion algorithms were applied to a merged data set, which consists of Green's functions established via cross-correlation between station-pairs belonging to available permanent and temporary seismic networks at the northwest part of Anatolia. Resultant maps of lateral variation exhibited similarly typical low velocities with low uncertainties for basin structures, i.e., Çınarcık, Tekirdağ, and Adapazarı Basins between periods 1 and 10 s. A clear signature of the NAFZ as an active continental fault zone in the area is marked by low group wave speeds. To the east, we were able to identify Istanbul-Zonguldak Zone with remarkable high group velocities.



## REFERENCES

- Aki, K., & Lee, W. H. K.** (1976). Determination of three-dimensional velocity anomalies under a seismic array using first P arrival times from local earthquakes: 1. A homogeneous initial model. *Journal of Geophysical Research*, 81(23), 4381-4399.
- Aki, K., Christoffersson, A., & Husebye, E. S.** (1977). Determination of the three-dimensional seismic structure of the lithosphere. *Journal of Geophysical Research*, 82(2), 277-296.
- Akyuz, H. S., Hartleb, R., Barka, A., Altunel, E., Sunal, G., Meyer, B., & Armijo, V. R.** (2002). Surface rupture and slip distribution of the 12 November 1999 Duzce earthquake (M 7.1), North Anatolian fault, Bolu, Turkey. *Bulletin of the Seismological Society of America*, 92(1), 61-66.
- Alaygut, D.** (1995). The petrographic investigation of the Turkish Strandja under the Thrace sedimentary basin. In *NW Turkey (abs.): International Earth Sciences Colloquium on the Aegean Region* (p. 1).
- Ambraseys, N. N.** (1970). Some characteristic features of the Anatolian fault zone. *Tectonophysics*, 9(2-3), 143-165.
- Ambraseys, N. N., & Finkel, C. F.** (1987). The Saros–Marmara earthquake of 9 August 1912. *Earthquake engineering & structural dynamics*, 15(2), 189-211.
- Ambraseys, N. N., & Jackson, J. A.** (2000). Seismicity of the Sea of Marmara (Turkey) since 1500. *Geophysical Journal International*, 141(3), F1-F6.A Modelling).
- Ambraseys, N. N., & Zatopek, A.** (1969). The Mudurnu Valley, West Anatolia, Turkey, earthquake of 22 July 1967. *Bulletin of the Seismological Society of America*, 59(2), 521-589.
- Armijo, R., Meyer, B., Navarro, S., King, G., & Barka, A.** (2002). Asymmetric slip partitioning in the Sea of Marmara pull-apart: A clue to propagation processes of the North Anatolian fault?. *Terra Nova*, 14(2), 80-86.
- Armijo, R., Pondard, N., Meyer, B., Uçarkus, G., de Lépinay, B. M., Malavieille, J., ... & Cagatay, N.** (2005). Submarine fault scarps in the Sea of Marmara pull-apart (North Anatolian Fault): Implications for seismic hazard in Istanbul. *Geochemistry, Geophysics, Geosystems*, 6(6).
- Bakırcı, T., Yoshizawa, K., & Özer, M. F.** (2012). Three-dimensional S-wave structure of the upper mantle beneath Turkey from surface wave tomography. *Geophysical Journal International*, 190(2), 1058-1076.
- Barka, A.** (1996). Slip distribution along the North Anatolian fault associated with the large earthquakes of the period 1939 to 1967. *Bulletin of the Seismological Society of America*, 86(5), 1238-1254.
- Barka, A. A.** (1992). The north Anatolian fault zone. In *Annales tectonicae* (Vol. 6, No. Suppl, pp. 164-195).
- Barka, A. A., & Kadinsky-Cade, K.** (1988). Strike-slip fault geometry in Turkey and its influence on earthquake activity. *Tectonics*, 7(3), 663-684.

- Barka, A., Akyuz, H. S., Altunel, E., Sunal, G., Cakir, Z., Dikbas, A., ... & Rockwell, T.** (2002). The surface rupture and slip distribution of the 17 August 1999 Izmit earthquake (M 7.4), North Anatolian fault. *Bulletin of the Seismological Society of America*, 92(1), 43-60.
- Bayrakci, G., Laigle, M., Bécel, A., Hirn, A., Taymaz, T., Yolsal-Çevikbilen, S., & Team, S.** (2013). 3-D sediment-basement tomography of the Northern Marmara trough by a dense OBS network at the nodes of a grid of controlled source profiles along the North Anatolian fault. *Geophysical Journal International*, 194(3), 1335-1357.
- Berk Biryol, C., Beck, S. L., Zandt, G., & Özacar, A. A.** (2011). Segmented African lithosphere beneath the Anatolian region inferred from teleseismic P-wave tomography. *Geophysical Journal International*, 184(3), 1037-1057.
- Bodin, T.** (2010). Transdimensional approaches to geophysical inverse problems.
- Bodin, T., & Sambridge, M.** (2009). Seismic tomography with the reversible jump algorithm. *Geophysical Journal International*, 178(3), 1411-1436.
- Bodin, T., Sambridge, M., Tkalčić, H., Arroucau, P., Gallagher, K., & Rawlinson, N.** (2012). Transdimensional inversion of receiver functions and surface wave dispersion. *Journal of Geophysical Research: Solid Earth*, 117(B2).
- Bois, P., La Porte, M., Lavergne, M., & Thomas, G.** (1971). Essai de détermination automatique des vitesses sismiques par mesures entre puits. *Geophysical Prospecting*, 19(1), 42-83.
- Bonnefoy-Claudet, S., Cotton, F., & Bard, P. Y.** (2006). The nature of noise wavefield and its applications for site effects studies: A literature review. *Earth-Science Reviews*, 79(3-4), 205-227.
- Box, G. E. P., & Tiao, G. C.** (1973). *Bayesian inference in statistical inference*. Addison-Wesley, Reading, Mass.
- Bürgmann, R., & Dresen, G.** (2008). Rheology of the lower crust and upper mantle: Evidence from rock mechanics, geodesy, and field observations. *Annual Review of Earth and Planetary Sciences*, 36.
- Campillo, M., & Paul, A.** (2003). Long-range correlations in the diffuse seismic coda. *Science*, 299(5606), 547-549.
- Carton, H., Singh, S. C., Hirn, A., Bazin, S., De Voogd, B., Vigner, A., ... & Sevilgen, V.** (2007). Seismic imaging of the three-dimensional architecture of the Çınarcık basin along the North Anatolian fault. *Journal of Geophysical Research: Solid Earth*, 112(B6).
- Celâl, A. M., & Yilmaz, Y.** (1981). Tethyan evolution of Turkey: a plate tectonic approach. *Tectonophysics*, 75(3-4), 181-241.
- Çubuk-Sabuncu, Y., Taymaz, T., & Fichtner, A.** (2017). 3-D crustal velocity structure of western Turkey: Constraints from full-waveform tomography. *Physics of the Earth and Planetary Interiors*, 270, 90-112.
- Delph, J. R., Biryol, C. B., Beck, S. L., Zandt, G., & Ward, K. M.** (2015). Shear wave velocity structure of the Anatolian Plate: anomalously slow crust in southwestern Turkey. *Geophysical Journal International*, 202(1), 261-276.
- Delph, J. R., Ward, K. M., Zandt, G., Ducea, M. N., & Beck, S. L.** (2017). Imaging a magma plumbing system from MASH zone to magma reservoir. *Earth and Planetary Science Letters*, 457, 313-324.

- Dewey, J. F., Helman, M. L., Knott, S. D., Turco, E., & Hutton, D. H. W.** (1989). Kinematics of the western Mediterranean. Geological Society, London, Special Publications, 45(1), 265-283.
- Duijndam, A. J. W.** (1988). BAYESIAN ESTIMATION IN SEISMIC INVERSION. PART I: PRINCIPLES 1. Geophysical Prospecting, 36(8), 878-898.
- Dziewonski, A. M., & Anderson, D. L.** (1981). Preliminary reference Earth model. Physics of the earth and planetary interiors, 25(4), 297-356.
- Dziewonski, A. M., Hager, B. H., & O'Connell, R. J.** (1977). Large-scale heterogeneities in the lower mantle. Journal of Geophysical Research, 82(2), 239-255.
- Fichtner, A., Saygin, E., Taymaz, T., Cupillard, P., Capdeville, Y., & Trampert, J.** (2013). The deep structure of the North Anatolian fault zone. Earth and Planetary Science Letters, 373, 109-117.
- Fichtner, A., Trampert, J., Cupillard, P., Saygin, E., Taymaz, T., Capdeville, Y., & Villasenor, A.** (2013). Multiscale full waveform inversion. Geophysical Journal International, 194(1), 534-556.
- Gans, C. R., Beck, S. L., Zandt, G., Biryol, C. B., & Ozacar, A. A.** (2009). Detecting the limit of slab break-off in central Turkey: new high-resolution Pn tomography results. Geophysical Journal International, 179(3), 1566-1572.
- Gao, H., & Shen, Y.** (2014). Upper mantle structure of the Cascades from full-wave ambient noise tomography: Evidence for 3D mantle upwelling in the back-arc. Earth and Planetary Science Letters, 390, 222-233.
- GEBCO 1997.** General Bathymetric Chart of the Oceans, Digital Version. CD-ROM. British Oceanographic Data Centre, Birkenhead.
- Gelman, A., Stern, H. S., Carlin, J. B., Dunson, D. B., Vehtari, A., & Rubin, D. B.** (2013). Bayesian data analysis. Chapman and Hall/CRC.
- Geyer, C. J.** (2015). R package aster2 (aster models), version 0.2-1.
- Gilks, W. R., Richardson, S., & Spiegelhalter, D. J.** (1996). Introducing markov chain monte carlo. Markov chain Monte Carlo in practice, 1, 19.
- Görür, N., & Okay, A. I.** (1996). A fore-arc origin for the Thrace Basin, NW Turkey. Geologische Rundschau, 85(4), 662-668.
- Görür, N., Cagatay, M. N., Sakinc, M., Sümengen, M., Sentürk, K., Yaltirak, C., & Tchapylyga, A.** (1997). Origin of the Sea of Marmara as deduced from Neogene to Quaternary paleogeographic evolution of its frame. International Geology Review, 39(4), 342-352.
- Green, P. J.** (1995). Reversible jump Markov chain Monte Carlo computation and Bayesian model determination. Biometrika, 82(4), 711-732.
- Gurer, O. F., Sangu, E., & Ozburan, M.** (2006). Neotectonics of the SW Marmara region, NW Anatolia, Turkey. Geological Magazine, 143(2), 229-241.
- Hastings, W. K.** (1970). Monte Carlo sampling methods using Markov chains and their applications.
- Honkura, Y., AM, I., Oshiman, N., Ito, A., Üçer, B., Baris, S., ... & Takahashi, F.** (2000). Preliminary results of multidisciplinary observations before, during and after the Kocaeli (Izmit) earthquake in the western part of the North Anatolian Fault Zone. Earth, planets and space, 52(4), 293-298.
- Izgi, G., Eken, T., Gaebler, P. J., & Taymaz T.,** (2018). Frequency-Dependent Shear Wave Attenuation along the Western Part of the North Anatolian Fault Zone, EGU2018-629, Geophysical Research Abstracts, Vol. 20 | Oral |

SM4.02. Fri, 13 Apr, 16:15–16:30, Room -2.2, EGU General Assembly  
2018, 08-13 April 2018, Vienna, Austria

- Kahraman, M., Cornwell, D. G., Thompson, D. A., Rost, S., Houseman, G. A., Türkelli, N., ... & Gülen, L.** (2015). Crustal-scale shear zones and heterogeneous structure beneath the North Anatolian Fault Zone, Turkey, revealed by a high-density seismometer array. *Earth and Planetary Science Letters*, 430, 129-139.
- Kaya, T.** (2012). Imaging of the North Anatolian Fault Zone underneath the Marmara Sea, Turkey, by ocean bottom magnetotellurics, Ph.D Thesis, Tokyo Institute of Technology.
- Kaya, T., Kasaya, T., Tank, S. B., Ogawa, Y., Tunçer, M. K., Oshiman, N., ... & Matsushima, M.** (2013). Electrical characterization of the North Anatolian Fault Zone underneath the Marmara Sea, Turkey by ocean bottom magnetotellurics. *Geophysical Journal International*, 193(2), 664-677.
- Kaya, T., Tank, S. B., Tunçer, M. K., Rokoityansky, I. I., Tolak, E., & Savchenko, T.** (2009). Asperity along the North Anatolian Fault imaged by magnetotellurics at Düzce, Turkey. *Earth, planets and space*, 61(7), 871-884.
- Kennett, B. L. N., & Engdahl, E. R.** (1991). Traveltimes for global earthquake location and phase identification. *Geophysical Journal International*, 105(2), 429-465.
- Ketin, I.** (1948). Über die tektonisch-mechanischen Folgerungen aus den grossen anatolischen Erdbeben des letzten Dezenniums. *Geologische Rundschau*, 36(1), 77-83.
- Ketin, İ.** (1969). Kuzey Anadolu fayı hakkında. *Maden Tetkik ve Arama Dergisi*, 72(72).
- Kind, R., Eken, T., Tilmann, F., Sodoudi, F., Taymaz, T., Bulut, F., ... & Schneider, F.** (2015). Thickness of the lithosphere beneath Turkey and surroundings from S-receiver functions. *Solid Earth*, 6(3), 971.
- Koulakov, I., Bindi, D., Parolai, S., Grosser, H., & Milkereit, C.** (2010). Distribution of seismic velocities and attenuation in the crust beneath the North Anatolian Fault (Turkey) from local earthquake tomography. *Bulletin of the Seismological Society of America*, 100(1), 207-224.
- Laigle, M., Becel, A., de Voogd, B., Hirn, A., Taymaz, T., & Ozalaybey, S.** (2008). A first deep seismic survey in the Sea of Marmara: Deep basins and whole crust architecture and evolution. *Earth and Planetary Science Letters*, 270(3-4), 168-179.
- Lay, T., & Wallace, T. C.** (1995). *Modern global seismology* (Vol. 58). Elsevier.
- Le Pichon, X., Şengör, A. M. C., Demirbağ, E., Rangin, C., Imren, C., Armijo, R., ... & Saatçılar, R.** (2001). The active main Marmara fault. *Earth and Planetary Science Letters*, 192(4), 595-616.
- Licciardi, A., Agostinetti, N. P., Lebedev, S., Schaeffer, A. J., Readman, P. W., & Horan, C.** (2014). Moho depth and  $V_p/V_s$  in Ireland from teleseismic receiver functions analysis. *Geophysical Journal International*, 199(1), 561-579.
- Lin, F. C., Moschetti, M. P., & Ritzwoller, M. H.** (2008). Surface wave tomography of the western United States from ambient seismic noise: Rayleigh and Love wave phase velocity maps. *Geophysical Journal International*, 173(1), 281-298.

- Lobkis, O. I., & Weaver, R. L.** (2001). On the emergence of the Green's function in the correlations of a diffuse field. *The Journal of the Acoustical Society of America*, 110(6), 3011-3017.
- Longuet-Higgins, M. S.** (1950). A theory of the origin of microseisms. *Phil. Trans. R. Soc. Lond. A*, 243(857), 1-35.
- Masce, J., & Martin, L.** (1990). Shallow structure and recent evolution of the Aegean Sea: a synthesis based on continuous reflection profiles. *Marine Geology*, 94(4), 271-299.
- McClusky, S., Balassanian, S., Barka, A., Demir, C., Ergintav, S., Georgiev, I., ... & Kastens, K.** (2000). Global Positioning System constraints on plate kinematics and dynamics in the eastern Mediterranean and Caucasus. *Journal of Geophysical Research: Solid Earth*, 105(B3), 5695-5719.
- McClusky, S., Reilinger, R., Mahmoud, S., Sari, D. B., & Tealeb, A.** (2003). GPS constraints on Africa (Nubia) and Arabia plate motions. *Geophysical Journal International*, 155(1), 126-138.
- McKenzie, D.** (1972). Active tectonics of the Mediterranean region. *Geophysical Journal of the Royal Astronomical Society*, 30(2), 109-185.
- Metropolis, N., Rosenbluth, A. W., Rosenbluth, M. N., Teller, A. H., & Teller, E.** (1953). Equation of state calculations by fast computing machines. *The journal of chemical physics*, 21(6), 1087-1092.
- Mordret, A., Shapiro, N. M., Singh, S., Roux, P., Montagner, J. P., & Barkved, O. I.** (2013). Azimuthal anisotropy at Valhall: The Helmholtz equation approach. *Geophysical Research Letters*, 40(11), 2636-2641.
- Moschetti, M. P., Ritzwoller, M. H., Lin, F. C., & Yang, Y.** (2010). Crustal shear wave velocity structure of the western United States inferred from ambient seismic noise and earthquake data. *Journal of Geophysical Research: Solid Earth*, 115(B10).
- Mosegaard, K., & Tarantola, A.** (1995). Monte Carlo sampling of solutions to inverse problems. *Journal of Geophysical Research: Solid Earth*, 100(B7), 12431-12447.
- Mutlu, A. K., & Karabulut, H.** (2011). Anisotropic Pn tomography of Turkey and adjacent regions. *Geophysical Journal International*, 187(3), 1743-1758.
- Nishida, K.** (2013). Global propagation of body waves revealed by cross-correlation analysis of seismic hum. *Geophysical Research Letters*, 40(9), 1691-1696.
- Nishida, K.** (2017). Ambient seismic wave field. *Proceedings of the Japan Academy, Series B*, 93(7), 423-448.
- Okay, A. I.** (1989). Tectonic units and sutures in the Pontides, northern Turkey. In *Tectonic evolution of the Tethyan region* (pp. 109-116). Springer, Dordrecht.
- Okay, A. I.** (2008). Geology of Turkey: a synopsis. *Anschnitt*, 21, 19-42.
- Okay, A. I., & Tüysüz, O.** (1999). Tethyan sutures of northern Turkey. *Geological Society, London, Special Publications*, 156(1), 475-515.
- Okay, A. I., Demirbağ, E., Kurt, H., Okay, N., & Kuşçu, İ.** (1999). An active, deep marine strike-slip basin along the North Anatolian fault in Turkey. *Tectonics*, 18(1), 129-147.
- Okay, A. İ., Kaşlılar-Özcan, A., Imren, C., Boztepe-Güney, A., Demirbağ, E., & Kuşçu, İ.** (2000). Active faults and evolving strike-slip basins in the

- Marmara Sea, northwest Turkey: a multichannel seismic reflection study. *Tectonophysics*, 321(2), 189-218.
- Okay, A. L., Satir, M., Tüysüz, O., Akyüz, S., & Chen, F.** (2001). The tectonics of the Strandja Massif: late-Variscan and mid-Mesozoic deformation and metamorphism in the northern Aegean. *International Journal of Earth Sciences*, 90(2), 217-233.
- Pamir, H. N., & Akyol, I. H.** (1943). Çorum ve Erbaa depremleri. *Türk Coğrafya Dergisi*, (2).
- Papaleo, E., Cornwell, D. G., & Rawlinson, N.** (2017). Seismic tomography of the North Anatolian Fault: New insights into structural heterogeneity along a continental strike-slip fault. *Geophysical Research Letters*, 44(5), 2186-2193.
- Papaleo, E., Cornwell, D., & Rawlinson, N.** (2018). Constraints on North Anatolian Fault Zone width in the crust and upper mantle from S wave teleseismic tomography. *Journal of Geophysical Research: Solid Earth*, 123(4), 2908-2922.
- Parke, J. R., Minshull, T. A., Anderson, G., White, R. S., McKenzie, D., Kucsu, I., ... & Sengor, C.** (1999). Active faults in the Sea of Marmara, western Turkey, imaged by seismic reflection profiles. *Terra Nova-Oxford*, 11(5), 223-227.
- Platt, J. P., & Behr, W. M.** (2011). Grain size evolution in ductile shear zones: Implications for strain localization and the strength of the lithosphere. *Journal of Structural Geology*, 33(4), 537-550.
- Polat, Y., Pampal, E. S., Stojanovska, E., Simsek, R., Hassanin, A., Kilic, A., ... & Yilmaz, S.** (2016). Solution blowing of thermoplastic polyurethane nanofibers: A facile method to produce flexible porous materials. *Journal of Applied Polymer Science*, 133(9).
- Rawlinson, N., & Sambridge, M.** (2004). Multiple reflection and transmission phases in complex layered media using a multistage fast marching method. *Geophysics*, 69(5), 1338-1350.
- Rawlinson, N., & Sambridge, M.** (2004). Wave front evolution in strongly heterogeneous layered media using the fast marching method. *Geophysical Journal International*, 156(3), 631-647.
- Rawlinson, W. D., Waliuzzaman, Z., Carter, I. W., Belessis, Y. C., Gilbert, K. M., & Morton, J. R.** (2003). Asthma exacerbations in children associated with rhinovirus but not human metapneumovirus infection. *The Journal of infectious diseases*, 187(8), 1314-1318.
- Reilinger, R., McClusky, S., Vernant, P., Lawrence, S., Ergintav, S., Cakmak, R., ... & Nadariya, M.** (2006). GPS constraints on continental deformation in the Africa-Arabia-Eurasia continental collision zone and implications for the dynamics of plate interactions. *Journal of Geophysical Research: Solid Earth*, 111(B5).
- Sabra, K. G., Gerstoft, P., Roux, P., Kuperman, W. A., & Fehler, M. C.** (2005). Extracting time-domain Green's function estimates from ambient seismic noise. *Geophysical Research Letters*, 32(3).
- Salah, M. K.** (2017). Lithospheric structure of Southeast Anatolia from joint inversion of local and teleseismic data. *Studia Geophysica et Geodaetica*, 61(4), 703-727.
- Salaün, G., Pedersen, H. A., Paul, A., Farra, V., Karabulut, H., Hatzfeld, D., ... & SIMBAAD Team.** (2012). High-resolution surface wave tomography

- beneath the Aegean-Anatolia region: constraints on upper-mantle structure. *Geophysical Journal International*, 190(1), 406-420.
- Sambridge, M., & Mosegaard, K.** (2002). Monte Carlo methods in geophysical inverse problems. *Reviews of Geophysics*, 40(3), 3-1.
- Sambridge, M., Bodin, T., Gallagher, K., & Tkalčić, H.** (2013). Transdimensional inference in the geosciences. *Phil. Trans. R. Soc. A*, 371(1984), 20110547.
- Saygin, E., & Kennett, B. L.** (2010). Ambient seismic noise tomography of Australian continent. *Tectonophysics*, 481(1-4), 116-125.
- Saygin, E., & Kennett, B. L. N.** (2012). Crustal structure of Australia from ambient seismic noise tomography. *Journal of Geophysical Research: Solid Earth*, 117(B1).
- Saygin, E., Cummins, P. R., Cipta, A., Hawkins, R., Pandhu, R., Murjaya, J., ... & Kennett, B. L. N.** (2015). Imaging architecture of the Jakarta Basin, Indonesia with transdimensional inversion of seismic noise. *Geophysical Journal International*, 204(2), 918-931.
- Sengor, A. M. C.** (1985). The story of Tethys: How many wives did Okeanos have?. *Episodes*, 8, 3-12.
- Şengör, A. M. C., Görür, N., & Şaroğlu, F.** (1985). Strike-slip faulting and related basin formation in zones of tectonic escape: Turkey as a case study.
- Shapiro, N. M., & Campillo, M.** (2004). Emergence of broadband Rayleigh waves from correlations of the ambient seismic noise. *Geophysical Research Letters*, 31(7).
- Shapiro, N. M., Campillo, M., Stehly, L., & Ritzwoller, M. H.** (2005). High-resolution surface-wave tomography from ambient seismic noise. *Science*, 307(5715), 1615-1618.
- Shearer, P. M.** (2009). *Introduction to seismology*. Cambridge University Press.
- Sivia, D. S.** (1996). Dealing with duff data. *Maximum Entropy and Bayesian Methods*, 131-137.
- Smith, A. D.** (1991). *National identity*. University of Nevada Press.
- Smith, W. H., & Sandwell, D. T.** (1997). Global sea floor topography from satellite altimetry and ship depth soundings. *Science*, 277(5334), 1956-1962.
- Snieder, R., & Larose, E.** (2013). Extracting Earth's elastic wave response from noise measurements. *Annual Review of Earth and Planetary Sciences*, 41.
- Snieder, R., & Wapenaar, K.** (2010). Imaging with ambient noise. *Physics Today*, 63(9), 44-49.
- Stein, R. S., Barka, A. A., & Dieterich, J. H.** (1997). Progressive failure on the North Anatolian fault since 1939 by earthquake stress triggering. *Geophysical Journal International*, 128(3), 594-604.
- Stein, S. and Wysession, M.** (2009). *An introduction to seismology, earthquakes, and earth structure*, John Wiley & Sons.
- Tanimoto, T., Um, J., Nishida, K., & Kobayashi, N.** (1998). Earth's continuous oscillations observed on seismically quiet days. *Geophysical Research Letters*, 25(10), 1553-1556.
- Tank, S. B., Honkura, Y., Ogawa, Y., Matsushima, M., Oshiman, N., Tunçer, M. K., ... & Işıkara, A. M.** (2005). Magnetotelluric imaging of the fault rupture area of the 1999 Izmit (Turkey) earthquake. *Physics of the Earth and Planetary Interiors*, 150(1-3), 213-225.
- Tarantola, A.** (2005). *Inverse problem theory and methods for model parameter estimation (Vol. 89)*. siam.

- Tarantola, A., & Valette, B.** (1982). Generalized nonlinear inverse problems solved using the least squares criterion. *Reviews of Geophysics*, 20(2), 219-232.
- Taylor, G., Rost, S., & Houseman, G.** (2016). Crustal imaging across the North Anatolian Fault Zone from the autocorrelation of ambient seismic noise. *Geophysical Research Letters*, 43(6), 2502-2509.
- Taymaz, T.** (1996). SP-wave travelttime residuals from earthquakes and lateral inhomogeneity in the upper mantle beneath the Aegean and the Hellenic Trench near Crete. *Geophysical Journal International*, 127(2), 545-558.
- Taymaz, T., & Price, S.** (1992). The 1971 May 12 Burdur earthquake sequence, SW Turkey: a synthesis of seismological and geological observations. *Geophysical Journal International*, 108(2), 589-603.
- Taymaz, T., Jackson, J., & McKenzie, D.** (1991). Active tectonics of the north and central Aegean Sea. *Geophysical Journal International*, 106(2), 433-490.
- Taymaz, T., Jackson, J., & Westaway, R.** (1990). Earthquake mechanisms in the Hellenic Trench near Crete. *Geophysical Journal International*, 102(3), 695-731.
- Taymaz, T., Westaway, R., & Reilinger, R.** (2004). Active faulting and crustal deformation in the Eastern Mediterranean region. *Tectonophysics*, 391(1), 1-10.
- Taymaz, T., Yilmaz, Y., & Dilek, Y.** (2007). The geodynamics of the Aegean and Anatolia: introduction. Geological Society, London, Special Publications, 291(1), 1-16.
- Toksöz, M. N., Shakal, A. F., & Michael, A. J.** (1979). Space-time migration of earthquakes along the North Anatolian fault zone and seismic gaps. *Pure and Applied Geophysics*, 117(6), 1258-1270.
- Turgut, S.** (1991). Evolution of the Thrace sedimentary basin and its hydrocarbon prospectivity. Generation, accumulation, and production of Europe's hydrocarbons, 415-437.
- Warren, L. M., Beck, S. L., Biryol, C. B., Zandt, G., Özacar, A. A., & Yang, Y.** (2013). Crustal velocity structure of Central and Eastern Turkey from ambient noise tomography. *Geophysical Journal International*, 194(3), 1941-1954.
- Weaver, R. L.** (2005). Information from seismic noise. *Science*, 307(5715), 1568-1569.
- Wong, H. K., Lüdmann, T., Ulug, A., & Görür, N.** (1995). The Sea of Marmara: a plate boundary sea in an escape tectonic regime. *Tectonophysics*, 244(4), 231-250.
- Yaltırak, C.** (2002). Tectonic evolution of the Marmara Sea and its surroundings. *Marine Geology*, 190(1-2), 493-529.
- Yang, Y., Ritzwoller, M. H., Levshin, A. L., & Shapiro, N. M.** (2007). Ambient noise Rayleigh wave tomography across Europe. *Geophysical Journal International*, 168(1), 259-274.
- Yao, H., van Der Hilst, R. D., & De Hoop, M. V.** (2006). Surface-wave array tomography in SE Tibet from ambient seismic noise and two-station analysis—I. Phase velocity maps. *Geophysical Journal International*, 166(2), 732-744.

- Yilmaz, Y., Tüysüz, O., Yigitbas, E., Can Genç, S., & Sengör, A. M. C.** (1998). Geology and tectonic evolution of the Pontides. *Memoirs-American Association of Petroleum Geologists*, 183-226.
- Yolsal-Çevikbilen, S.** (2014). Seismic anisotropy along the Cyprean arc and northeast Mediterranean Sea inferred from shear wave splitting analysis. *Physics of the Earth and Planetary Interiors*, 233, 112-134.
- Yolsal-Çevikbilen, S., & Taymaz, T.** (2012). Earthquake source parameters along the Hellenic subduction zone and numerical simulations of historical tsunamis in the Eastern Mediterranean. *Tectonophysics*, 536, 61-100.
- Yolsal-Cevikbilen, S., Biryol, C. B., Beck, S., Zandt, G., Taymaz, T., Adiyaman, H. E., & Özacar, A. A.** (2012). 3-D crustal structure along the North Anatolian Fault Zone in north-central Anatolia revealed by local earthquake tomography. *Geophysical Journal International*, 188(3), 819-849.
- Yolsal-Çevikbilen, S., Taymaz, T., & Helvacı, C.** (2014). Earthquake mechanisms in the Gulfs of Gökova, Sığacık, Kuşadası, and the Simav Region (western Turkey): Neotectonics, seismotectonics and geodynamic implications. *Tectonophysics*, 635, 100-124.
- Yolsal, S.** (2008). Source mechanism parameters and slip distributions of Crete-Cyprus Arcs, dead sea transform fault earthquakes and historical tsunami simulations. PhD thesis.
- Zulfakriza, Z., Saygin, E., Cummins, P. R., Widiyantoro, S., Nugraha, A. D., Lüher, B. G., & Bodin, T.** (2014). Upper crustal structure of central Java, Indonesia, from transdimensional seismic ambient noise tomography. *Geophysical Journal International*, 197(1), 630-635.



## CURRICULUM VITAE



**Name Surname** : Buse Turunçtur

**Place and Date of Birth** : Istanbul-Turkey / 01.09.1992

**E-Mail** : turunçtur@itu.edu.tr

### EDUCATION :

- **B.Sc.** : 2017, Istanbul Technical University, Faculty of Mines, Department of Geophysical Engineering
- **M.Sc.** : 2018, Istanbul Technical University, Faculty of Mines, Department of Geophysical Engineering

### PROFESSIONAL EXPERIENCE AND REWARDS:

- 2018 | **Commonwealth Scientific and Industrial Research Organization (CSIRO) - Perth/Australia**  
15 Feb – 05 Apr 2018 | Deep Earth Imaging, Future Science Platform  
28 Jun – 14 Sep 2018 | Deep Earth Imaging, Future Science Platform
- 2015 | **Turkish Scientific and Technological Research Council (TÜBİTAK) - Istanbul/Turkey**  
20 days | Marmara Research Center, Earth and Marine Science Institute
- 2015 | **Turkish Petroleum Corporation - Ankara/Turkey**  
30 days | Data processing and field work
- 2014 | **Bogazici University Kandilli Observatory and Earthquake Research Institute (KOERI) - Istanbul/Turkey**  
31 days | with in the framework of *Continental Dynamics: Within the context of Central Anatolian Tectonics Project (CD-CAT)*

## **OTHER PUBLICATIONS, PRESENTATIONS AND PATENTS:**

- Eken, T., Confal J.M., Tilmann, F., **Turunctur, B.**, Taymaz, T., 2018. New Splitting Measurements based on Teleseismic Direct S-wave Analysis for Turkey, *Geophysical Research Abstracts*, Vol. 20, EGU2018-13888, *European Geophysical Union General Assembly 2018* 8–13 April 2018, Vienna, Austria **(poster)**.
- **Turunctur, B.**, Eken, T., Confal J.M., Taymaz, T., 2017. Apparent S-wave Splitting Parameters under Various Two-Layer Models, *Earth Sciences & Engineering Education Symposium and Student Graduation Projects Exhibition (YER 2017)-Istanbul Technical University* 12 June 2017, Istanbul, Turkey **(oral & poster)**.
- **Turunctur, B.**, Eken, T., Confal J.M., Taymaz, T., 2017. Apparent S-wave Splitting Parameters under Various Two-Layer Models. *90th Anniversary of Geophysics-Istanbul University* 10-12 May 2017, Istanbul, Turkey **(oral)**.
- **Turunctur, B.**, Eken, T., Confal J.M., Taymaz, T., 2017. Apparent S-wave Splitting Parameters under Various Two-Layer Models, *Geophysical Research Abstracts*, Vol. 19, EGU2017-7812, *European Geophysical Union General Assembly 2017* 23–28 April 2017, Vienna, Austria **(poster)** .